UCLA
UCLA Electronic Theses and Dissertations

Title
Engineering Nanomaterials towards Energy Harvesting and Virological Applications

Permalink
https://escholarship.org/uc/item/51d9v5sh

Author
Weng, Ding

Publication Date
2012

Peer reviewed|Thesis/dissertation

eScholarship.org Powered by the California Digital Library
University of California

UNIVERSITY OF CALIFORNIA

Los Angeles

Engineering Nanomaterials towards Energy Harvesting and Virological Applications

A dissertation submitted in partial satisfaction of the

requirements for the degree Doctor of Philosophy

in Chemical Engineering

by

Ding Weng

2012

© Copyright by

Ding Weng

2012

ABSTRACT OF THE DISSERTATION

Engineering Nanomaterials towards

Energy Harvesting and Virological Applications

by

Ding Weng

Doctor of Philosophy in Chemical Engineering

University of California, Los Angeles, 2012

Professor Yunfeng Lu, Chair

Nanomaterials, defined as the materials with critical dimensions less than 100 nm, often exhibit unique properties in comparison with their bulk counterparts. The capability to synthesize huge families of nanomaterials provides human being with unprecedented opportunities towards more glory human civilization. Focusing

on nanomaterial synthesis and application, this dissertation mainly contains three topics related to energy harvesting and health care, including: 1) the synthesis of thermoelectric nanocomposites from dissimilar nanocrystals as building blocks for energy harvesting, 2) the synthesis of self-disinfection coatings from photoactive nanocrystals as building blocks for preventing rapid and large-scale spread of viruses, and 3) construction of virus-polymer nanoparticles with significantly enhanced stability for biomedical applications such as gene delivery. By engineering the nanocrystal-nanocrystal interface, the virus-nanocrystal interface, and the virus-polymer interface, different nanocomposites were successfully developed, which were briefly summarized below.

1) The synthesis of thermoelectric nanocomposites from dissimilar nanocrystals. Thermoelectricity has been considered as a promising alternative energy harvesting measure to solar cell, wind power, waterpower, and nuclear power. The efficiency of a thermoelectric material is judged by its dimensionless figure of merit, *ZT*. Mathematically, *ZT* is proportional to the square of the material's Seebeck Coefficient, electrical conductivity, and average working temperature; and inversely proportional to its thermal conductivity. The phonon-glass electron-crystal structure has been proposed to increase the overall thermoelectric performance by enhancing their phonon scattering while maintaining electrical conductivity. This hypothesis was previously realized in

superlattice materials; however, the use of such superlattice was limited by its high cost and difficulties in scale-up fabrication.

Herein, a novel class of nanocomposites was proposed to achieve such phonon-glass electron-crystal structure from nanocrystals of lead telluride and TiO_2 as building blocks. Lead telluride nanocrystals were synthesized with oleic acid as ligands and served as the electron-crystal portion; while titanium oxide nanocrystals were synthesized with oleic acid as ligands and served as the phonon-glass portion. The interfaces between the nanocrystals further scattered transportation of phonons. Existence of oleic acid provided the nanocrystals enough suspension ability in hexane to achieve homogeneous mixing, leading to the formation of homogenous nanocrystals composites. Then oleic acid was completely removed to achieve a highly densified bulk device after spark plasma sintering. As a result, the $PbTe/TiO_2$ nanocomposites provided low thermal conductivity similar to that of a superlattice structure, which has almost approached the lowest theoretical calculated results.

2) The synthesis of self-disinfection coatings from photoactive nanocrystals. Influenza A virus historically has played a significant role in pandemics and killed millions of people. In average, it caused three deadly pandemics per century since the seventeenth century. Antiviral drugs and vaccines have been developed to fight against influenza A virus as efficient *in vivo* measures, but their stockpiling and

development are not economical due to unpredictable outbreak time and type of influenza pandemics. Thus *in vitro* solution is non-negligible to prevent rapid spread of influenza A virus. The influenza viruses can survive a remarkably long time on contaminated surfaces, for example over 24 hr on hands, stainless steel and plastics, and also spread through aerosol. A few disinfectant chemicals and methods have been introduced for disinfecting surfaces, like hypochlorous acid, ozone, UV shining, etc. Harmful chemicals may get involved and not be suitable for continuous use in areas with large flowing population. Therefore self-disinfecting coatings are better solution for continuous operation.

Herein, a visible light powered self-disinfecting antiviral coating was proposed to cut off the spread of influenza A viruses. Visible light powered copper indium zinc sulfide nanocrystals were synthesized and uniformly coated on glass cover slips with oleic acid as ligands. Such coatings exhibited highly effective disinfecting ability for influenza A virus; 74% of viruses were disinfected in first 15 min and up to 94% of viruses were disinfected in 2 hr. Mechanism studies showed that this disinfection process involved the deactivation of viral surface proteins by the photo-generated oxidative free radicals. This mechanism suggested a universal disinfecting ability. The disinfection of hepatitis C virus and bacteria were also successfully observed under visible lights. To explore the disinfection without light illumination, self-disinfecting coatings were also made from non-

stoichiometric perovskite-structured lanthanum manganese oxide. The disinfection process was related to the oxidative ability of Mn^{4+} by series of investigations. 76% of influenza A virus was disinfected on 15 min contact with as-prepared coatings.

3) The synthesis of virus-polymer nanoparticles for gene delivery. Besides understanding how to disinfect viruses, the other direction is to stabilize viruses towards more effective vectors for gene delivery. To date, extensive efforts have been devoted to engineering virus vectors for gene therapy, which has mainly focused on large-scale vector production with reduced immunogenicity. However, poor stability of such virus vectors still limits their application, particularly, during their storage and transportation process.

Herein, a novel class of virus nanogel was proposed by wrapping each virion with a thin acid-degradable polymer shell. Adenovirus was selected as a model system. Positively charged monomers and acid-degradable crosslinkers were *in situ* co-polymerized onto the viral surface. Upon the degradation of the polymer shells, encapsulated virus was released. It was found that the stability of the encapsulated adenovirus has been dramatically improved over 11 folds after 12 day storage at 4 °C, in comparison with the native virus counterpart. Based on this study, we demonstrated that virus stability could be significantly enhanced for gene delivery application.

The dissertation of Ding Weng is approved.

Harold Monbouquette

Yi Tang

Qibing Pei

Yunfeng Lu, Committee Chair

University of California, Los Angeles

2012

DEDICATION

To my loving mother and father,

Min Wang and *Duan Weng*

My respectful advisor

Yunfeng Lu

And all my dear friends

Without your faith, support and constant encouragement

This dissertation could never have been finished.

TABLE OF CONTENTS

LIST OF FIGURES xvii

LIST OF TABLES xxii

ACKNOWLEDGEMENTS xxiii

VITA xxiv

Chapter 1 Introduction 1

1.1 Nanomaterials 1

1.2 Thermoelectricity 3

1.2.1 Global Energy Concerns 3

1.2.2 What is Thermoelectricity 4

1.2.3 Theoretical Model of Thermoelectricity 9

1.2.4 Thermoelectricity: Current State of the Art 14

1.2.5 Thesis Objective 16

1.3 Antiviral Self-disinfecting Coatings 17

1.3.1 Virus, Tiny Infectious Agent 17

1.3.2 Influenza A Virus, Pandemics and Human Being 25

1.3.3 Antiviral Coatings: Current State of the Art 30

1.3.4 Thesis Objective 32

1.4 Virus as Gene Delivery Vector 33

1.4.1 Genetic Disorders and Gene Therapy 33

1.4.2 Adenovirus, the Ultimate Infectious Agent 34

1.4.3 Polymer Nanogel: Current State of the Art 35

1.4.4 Thesis Objective 36

Chapter 2 Synthesis of Thermoelectric Nanomaterials 37

2.1 Background Introduction 37

2.1.1 Motivation: Significance of Nano-size 37

2.1.2 Research Objective..... 39

2.2 Experimental Procedure 41

2.2.1 Solvothermal Synthesis of PbTe Nanocrystals 41

2.2.2 High Throughput Facile Synthesis of PbTe Nanocrystals in Aqueous Solution 41

2.2.3 Reverse Micelles Assisted Synthesis of SiO_2/PbTe Core-shell Nanoparticles 42

2.2.4 Electrospray Assisted Synthesis of PbTe/SiO_2 Nanocomposites 42

2.2.5 Two Phase Approach Synthesis of TiO_2 Nanocrystals 43

2.2.6 Chemical Removal of the Organic Ligands in Thermoelectric Nanocomposites 43

2.3 Materials Characterization and Discussion 45

2.3.1 Solvothermal Synthesis of PbTe Nanocrystals 45

2.3.2 High Throughput Facile Synthesis of PbTe Nanocrystals in Aqueous Solution 46

2.3.3 Reverse Micelles Assisted Synthesis of SiO_2/PbTe Core-shell Nanoparticles 47

2.3.4 Electrospray Assisted Synthesis of PbTe/SiO_2 Nanocomposites 51

2.3.5 Two Phase Approach Synthesis of TiO_2 Nanocrystals 53

2.4 Assemble Thermoelectric Devices for Application 56

2.4.1 Mixing and Hot Plate Drying of PbTe/TiO_2 Nanocomposites 56

2.4.2 Removing the Organic Residue 58

2.4.3 Reducing Oxidation Layer 60

2.4.4 Spark Plasma Sintering 61

2.5 Thermoelectric Property 67

2.6 Conclusion and Future Direction 69

Chapter 3 Visible Light Driving Self-Disinfecting Coating 71

3.1 Background Introduction 71

3.1.1 Motivation: *In Vitro* Antiviral Disinfecting Coatings 71

3.1.2 Research Objective 73

3.2 Experimental Procedure 74

3.2.1 Synthesis of $CuInZn_4S_6$ nanocrystal 74

3.2.2 Design Self-Disinfecting Coating 74

3.2.3 Disinfection of H1N1 Influenza A Virus 75

3.2.4 Disinfection of HCV 75

3.2.5 Disinfection of *E. coli.* 76

3.2.6 Deactivation of Hemagglutinin (HA) 76

3.2.7 Deactivation of Neuraminidase (NA) 77

3.2.8 Deactivation of Trypsin 77

3.3 Results and Discussion 78

3.3.1 Characterization of As-prepared $CuInZn_4S_6$ Nanocrystals Coating 78

3.3.2 Effect of Surface Ligands Exchange 79

3.3.3 Disinfection of Influenza A Virus 81

3.3.4 Disinfection of HCV and *E. coli.* 83

3.3.5 Disinfection Mechanism 85

3.4 Conclusion and Future Direction 88

Chapter 4 Spontaneous and Continuous Disinfection of Influenza A Virus by Non-stoichiometric Perovskite-structured La_xMnO_3 89

4.1 Background Introduction 89

4.1.1 Motivation: External Condition Independent Self-disinfecting Coating 89

4.1.2 Research Objective 91

4.2 Experimental Procedure 93

4.2.1 Preparation of Non-stoichiometric Perovskite-structured La_xMnO_3 (x=1, 0.95, 0.9) 93

4.2.2 X-ray Diffraction (XRD) Patterns 93

4.2.3 Electron Paramagnetic Resonance (EPR) Spectra 93

4.2.4 Temperature Programmed Reduction (TPR) 94

4.2.5 Disinfecting Ability of La_xMnO_3 (x=1, 0.95, 0.9) 94

4.2.6 Deactivation of Hemagglutinin 95

4.2.7 Deactivation of Neuraminidase 95

4.3 Results and Discussion 97

4.3.1 Characterization of Perovskite-structured $LaMnO_3$ 97

4.3.2 Disinfection of Influenza A Virus 99

4.3.3 Disinfection Mechanism 101

4.4 Conclusion and Future Direction 102

Chapter 5 Novel Adenovirus Nanogel as Gene Delivery Vector with Enhanced Stability 103

5.1 Background Introduction 103

5.1.1 Motivation: Adenovirus as DNA Delivery Vector 103

5.1.2 Research Objective 104

5.2 Experimental Procedure 106

5.2.1 Covalently Conjugation of Polymerizable Acryl Groups onto Adenovirus Capsid 106

5.2.2 Synthesis of Positively Charged Monomer 106

5.2.3 Synthesis of the Novel Adenovirus Nanogel 107

5.2.4 4 °C Stability of the Novel Adenovirus Nanogel 107

5.2.5 Luciferase Assay 108

5.3 Results and Discussion 109

5.3.1 Modification of Amine Group Resulted Significant Loss in Infectivity 109

5.3.2 NMR Characterization of Synthesized NTris Monomer 110

5.3.3 DLS Characterization of NTris Adenovirus Nanogel 110

5.3.4 Enhanced 4 °C Stability of NTris Adenovirus Nanogel 111

5.4 Conclusion and Future Direction 114

Chapter 6 Thesis Conclusion 115

References 117

LIST OF FIGURES

Figures	Description	Page
Figure 1.1	Sketch for work mode of thermoelectric device. (**a**) Use temperature gradient to generate electric power and (**b**) use electric power to transport heat.	4
Figure 1.2	Dimensionless figure of merit vs. Temperature for current state of the art.	15
Figure 1.3	Development of the thermoelectric figure of merit.	15
Figure 1.4	Tobacco Mosaic Virus negative stained with heavy metal.	19
Figure 1.5	TEM image of adenoviruses with negative stain.	20
Figure 1.6	Enveloped viruses. (**a**) TEM image of influenza A viruses, (**b**) 3D illustration of the influenza A virus and (**c**) diagram of the HIV virus.	20
Figure 1.7	Diagram of enterobacteria phage T4 with artificial colors, which shows complex structure containing an icosahedral head, a helical tail and protein fibers.	21
Figure 2.1	Plot of $Z_{2D}T$ vs layer thickness a for (**1**) $a_0 - b_0$ plane layers and (**2**) $a_0 - c_0$ plane layers. The dashed line indicates the best ZT for 3D bulk Bi_2Te_3.	38
Figure 2.2	Plot of $Z_{1D}T$ vs wire width a for 1D wires fabricated along the x, y, and z directions.	38
Figure 2.3	Proposed dissimilar nanocomposites as phonon-glass electron-crystal thermoelectric materials.	42
Figure 2.4	TEM image of solvothermal synthesized PbTe nanocrystals.	45
Figure 2.5	XRD pattern of solvothermal synthesized PbTe nanocrystals.	46
Figure 2.6	TEM image of aqueous solution synthesized PbTe nanocrystals.	47
Figure 2.7	XRD pattern of aqueous solution synthesized PbTe nanocrystals.	47
Figure 2.8	Sketch of micro emulsion assisted synthesis of SiO_2/PbTe core-shell nanoparticles	48

Figures	Description	Page
Figure 2.9	SEM image of micro emulsion assisted synthesized SiO_2/PbTe core-shell nanoparticles.	50
Figure 2.10	EDS spectra of as-prepared SiO_2/PbTe core-shell nanoparticles. Red one is the element ratio of the small point; blue one is the element ratio of the whole window.	50
Figure 2.11	XRD pattern of as-prepared SiO_2/PbTe core-shell nanoparticles.	51
Figure 2.12	Sketch of electrospray assisted synthesis of PbTe/SiO_2 nanocomposites.	52
Figure 2.13	SEM image of electrospray assisted synthesis of PbTe/SiO_2 nanocomposites.	53
Figure 2.14	TEM of two phase approach synthesized TiO_2 nanocrystals.	54
Figure 2.15	XRD of two phase approach synthesized TiO_2 nanocrystals.	54
Figure 2.16	TEM image of the PbTe/TiO_2 homogeneous mixture.	56
Figure 2.17	SEM and EDX mapping of PbTe/TiO_2 nanocomposites in solid state. (**a**) is the SEM picture of a cluster after solvent got totally evaporated; (**b**) is the mapping of all kinds of elements; (**c**) is the EDX mapping of Pb; (**d**) is the EDX mapping of Te; (**e**) is the EDX mapping of Ti.	57
Figure 2.18	TGA plots of (**B**) temperature, (**D**) As-prepared PbTe/TiO_2 mixture, (**E**) PbTe/TiO_2 mixture after treatment with $LiBHEt_3$ (Method 2), (**C**) PbTe/TiO_2 mixture after treatment with $LiBHEt_3$/Me_3SiCl (Method 3), (**F**) PbTe/TiO_2 mixture after treatment with NaOH/$NaBH_4$ (Method 4).	59
Figure 2.19	FTIR spectra of (**a)** As-prepared PbTe/TiO_2 nanocomposites, (**b**) after treatment with $LiBHEt_3$ (Method 2), (**c**) after treatment with $LiBHEt_3$/Me_3SiCl (Method 3), (**d**) after treatment with NaOH/$NaBH_4$ (Method 4).	60
Figure 2.20	Typical Sintering Chart. Extension vs. Time.	61
Figure 2.21	SEM image of pure PbTe nanocrystals after sintering.	62
Figure 2.22	SEM image of PbTe/TiO_2 nanocomposites after sintering.	63

Figures	Description	Page
Figure 2.23	XRD results and TiO_2 crystal lattices.	65
Figure 2.24	Seebeck Coefficient of PbTe/TiO_2 after SPS. (**a black**) is Seebeck coefficient and (**a red**) is figure of merit *ZT*. (**b black**) is electrical conductivity and (**b red**) is thermal conductivity.	67
Figure 3.1	Illustration of disinfecting virus on a self-disinfecting surface powered by visible light.	73
Figure 3.2	(**a**) XRD pattern of as-prepared $CuInZn_4S_6$ nanocrystals, which suggested ~20 nm crystal size calculated from Debye-Scherrer Equation. (**b**) Absorption spectrum of as-prepared $CuInZn_4S_6$ nanocrystals. (**c**) TEM image shows a particle size around 20 nm by direct observation. (**d**) AFM image of the coating surface suggest the formation of uniformed self-disinfecting coatings.	78
Figure 3.3	(**a**) Illustration of surface ligands exchange process that $CuInZn_4S_6$ nanocrystals get more hydrophilic as time goes on then eventually get lost during washing. (**b**) Different time of surface ligands exchange will affect the overall disinfecting performance of the coating.	80
Figure 3.4	Disinfection of influenza A virus. (**a**) Disinfection efficiency of CIZS-coated surfaces over time. (**b**) Disinfection efficiency of CIZS- and P25-coated surfaces with and without illumination for 1 hr. (**c**) Disinfection efficiency of the CIZS-coated surfaces prepared with and without the sintering process.	81
Figure 3.5	Disinfection efficiency of P25-coated surfaces with and without illumination for 1 hr. UV lights were not blocked, thus TiO_2 just contribute 29% of total disinfection on PR8.	82
Figure 3.6	Disinfection of hepatitis C virus and bacteria. (**a**) Disinfection of HCV and (**b**) *E. coli.* by CIZS-coated surface after 1-hr illumination and fluorescence images of the HCV-infected cells on the CIZS-coated surface: (**c**) control, (**d**) with and (**e**) without the illumination.	84

Figures	Description	Page
Figure 3.7	Inactivation of proteins: hemagglutinin (**a**) and neuraminidase (**b**) on CIZS-coated surface and bare glass surface with and without illumination for 2 hr. and trypsin (**c**) by CIZS nanocrystals with and without illumination.	85
Figure 4.1	Oxidization thus disinfection of influenza A virus by nonstoickiometric perovskite-structured La_xMnO_3 (x=1, 0.95, 0.9).	91
Figure 4.2	The XRD patterns of the La_xMnO_3 (x=1, 0.95, 0.9) samples.	97
Figure 4.3	The EPR spectrum of the La_xMnO_3 (x=1, 0.95, 0.9) samples.	98
Figure 4.4	The H_2-TPR profiles of the La_xMnO_3 (x=1, 0.95, 0.9) samples.	98
Figure 4.5	Disinfection of influenza A virus. (**a**) Disinfecting ability of La_xMnO_3 (x=1, 0.95, 0.9) samples got better with the increase of the surface concentration, $La_{0.9}MnO_3$ showed the best disinfecting ability of 76% on PR8 in 15 min with surface concentration of 20 $\mu g/mm^2$ and the infectivity of PR8 kept decreasing with time (**b**). Mechanism study showed that hemagglutinin (**c**) and neuraminidase (**d**) have been deactivated after treated by $La_{0.9}MnO_3$.	100
Figure 5.1	Design of novel adenovirus nanogels utilizes non-covalent electric interaction to anchor polymer shell onto surface of adenovirus.	104
Figure 5.2	Synthesis route of positively charged monomer.	106
Figure 5.3	Loss of infectivity by covalently conjugating acryl groups onto adenovirus surface proteins.	109
Figure 5.4	NMR spectrum of as-prepared NTris monomer.	110
Figure 5.5	DLS characterization of as-prepared NTris adenovirus nanogel. Bottom-left axes with black and red lines are size distribution of native adenovirus (NativeAdv) and NTris adenovirus nanogel (NTrisAdv). Top-right axes with shadowed columns are zeta potential of NTris adenovirus nanogel.	111

Figures	Description	Page
Figure 5.6	Enhanced 4 °C stability of NTris adenovirus nanogel. (**a**) presents relative infectivity, which use native virus infectivity as reference respectively to the date. (**b**) presents specific infectivity of the same data in **a**, which reflects the infectivity drop of native adenovirus and enhanced stability of as-prepared nanogel more apparently. Notation "Acid" means the samples were acid-degraded for 30 min before infect the cells. However, not much enhancement in adverse pH has been found.	112

LIST OF TABLES

Table	Description	Page
Table 2.1	Density measurement of $PbTe/TiO_2$ samples after sintering.	64
Table 4.1	The integrated peak area of the La_xMnO_3 (x=1, 0.95, 0.9) samples.	99

ACKNOWLEDGEMENTS

Five years and three months PhD life in UCLA is full of fun though stressful. Meeting new people, communicating with collaborators, making discussion, attending seminars and even failure in experiments all are unforgettable. I want to appreciate my parents. They gave me life and kept leading me and supporting me.

I would like to appreciate my professor, Dr. Yunfeng Lu, for recruiting me in his research group six years ago; even my background was not chemical engineering, materials science or chemistry but physics and mathematics. I have passion in materials research and he gave me enough trust, time and support to start slowly. And when I felt interested in virus, he was really open mind and helped me finding new collaborations. Also I would like to thank other faculties in my departments and my collaborating principal investigators in Department of Molecular and Medical Pharmacology, Dr. Ren Sun and Dr. Ting-Ting Wu gave my plenty of help in influenza virus projects and Dr Lily Wu supported research on adenovirus.

I want to appreciate Post-doc fellows and other students in our lab too. Dr. Junwei Wang, Dr. Zhenglong Yang, Dr. Daocheng Pan and Dr. Qiangfeng Xiao helped me a lot in early study of inorganic material synthesis. Dr. Ming Yan, Juanjuan Du, Jing Jin and Yang Liu helped me a lot in polymer nanogel synthesis. Also my collaborator in pharmacology, Hangfei Qi, Jun Feng and Ziyue (Karen) Jiang, taught me cell culturing techniques and biology knowledge. We have had a wonderful collaborating time together.

Finally I would thank the funding for supporting my experiments and living in UCLA.

VITA

2002 Fall - 2006 Summer	B. S., Fundamental Sciences, Phys & Math Tsinghua University Beijing, P. R. China
2006 Fall - 2007 Winter	Ph.D. Candidate, Chemical Engineering Teaching Assistant Tulane University, New Orleans, Louisiana, the United States Transferred to UCLA

Chapter 1 Introduction

1.1 Nanomaterials

Nano, the prefix terminology becomes famous since late 20 century all over the world. A nanomaterial is defined by European Commission as:

"A natural, incidental or manufactured material containing particles, in an unbound state or as an aggregate or as an agglomerate and where, for 50 % or more of the particles in the number size distribution, one or more external dimensions is in the size range 1 nm - 100 nm.

In specific cases and where warranted by concerns for the environment, health, safety or competitiveness the number size distribution threshold of 50 % may be replaced by a threshold between 1 and 50 %.

By derogation from the above, fullerenes, graphene flakes and single wall carbon nanotubes with one or more external dimensions below 1 nm should be considered as nanomaterials."

Shrinking in the size from bulk to nano unveils much more unprecedented properties of materials because size of the particle approaches the critical scale of physical phenomena and enough atoms have been exposed on the surface. The energy level, band structure and interaction between particles or particle and environment are very different from inside of the particle. Also dislocation of crystals could affect the performance of the nanoparticles much more apparently, like nanojunctions and core-shell structures, which band gap has been distorted on the interface. Quantum confinement could be considerably enhanced and has been widely applied in clinical diagnostics. Surface plasmon resonance is another important physical phenomenon. Its absorption frequency and intensity are related to type of metallic material and very sensitive to

particle shapes, sizes and size distribution. Engineering nanomaterials with enhanced or tunable localized surface plasmon resonance have unveiled its applications as biosensors. However nano-size effect sometimes finds troubles for semiconductor industry. For example, ferromagnetic materials smaller than 10 nm will switch their magnetization using room temperature thermal energy, which makes them fail in memory storage. Therefore engineering nanomaterials for desired property is of great significance for today's material science and technology.

1.2 Thermoelectricity

1.2.1 Global Energy Concerns

Nowadays, a huge dependence has been put onto the fossil fuels supplied energy. As an unrecoverable resource, the price of fossil fuel continues increasing, which make an urgent demand for the alternative energy technologies to reduce the addiction on it. Thus after hydro power, wind power, geothermal power, solar energy, biomass energy and nuclear power, thermoelectric technology has come to the front. Different from the single application of other technologies, thermoelectric technology can be applied in two ways. One is generating electric current from heat gradient, such as temperature detection (thermal couples, used in everywhere), power generation (as radioisotope thermoelectric generators, extremely long working life) and waste heat recycling (in energy industry or vehicle's exhaust) as shown in **Figure 1.1a**. The other one is transferring heat as a solid state heat pump (semiconductor cooling or heating, such like portable refrigerator), working like **Figure 1.1b**. According to the expectation from ENECO, a development stage company, annual thermoelectric market should be 250 million, and multi billions of potential markets including waste heat recycle and cooling can be expected in the future.

Taking the application on vehicle as an instance.[1] For a 200 Hp engine, it can generate around 150 kW of power and in the most, one third could be turned in driving and the other 100 kW will be wasted. Even only 4.5% of energy could be recycled from thermoelectric device placed on the exhaust pipe, it is already a substantial amount.[2] Moreover, by increasing the thermoelectric materials' efficiency and optimize the design of heat exchanger, we can further increase the percentage of recycle.

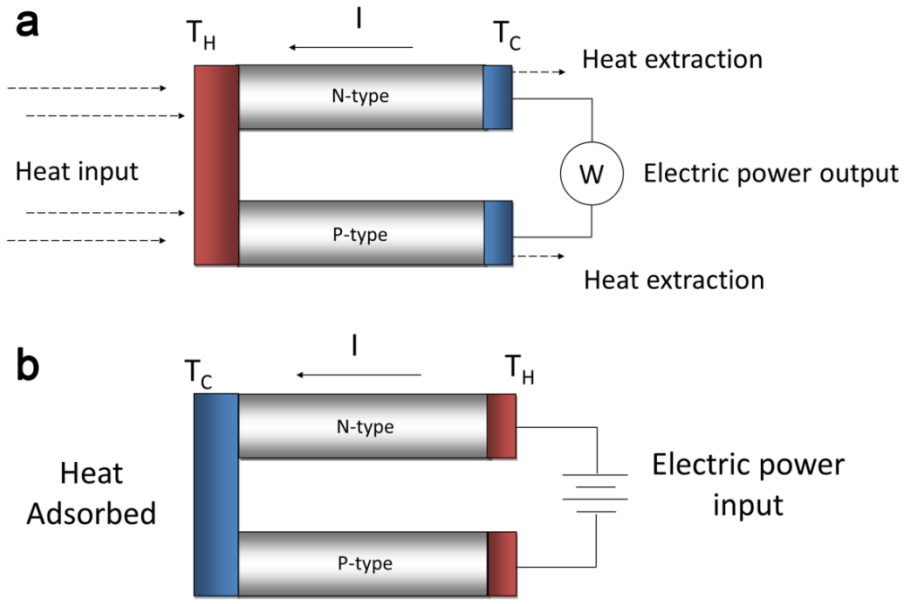

Figure 1.1 Sketch for work mode of thermoelectric device. (**a**) Use temperature gradient to generate electric power and (**b**) use electric power to transport heat.

1.2.2 What is Thermoelectricity

Thermoelectricity stands for a set of phenomena in which an electric potential can cause a temperature difference or a temperature difference can generate an electric potential. In modern technical usage, the word thermoelectricity almost always refers collectively to the Seebeck Effect, the Peltier Effect, and the Thomson Effect. And in many textbooks, thermoelectric effect is considered combinatorial as the Peltier-Seebeck Effect, which derives from the independent discoveries of Estonian-German Physicist Thomas Johann Seebeck and French physicist Jean Charles Athanase Peltier.

The Seebeck Effect

In 1821, T. J. Seebeck discovered (published in 1822) that a compass needle could be deflected if placed near a closed loop composed of two joined dissimilar metals with a

temperature difference.[3] And if the temperature difference was reversed, the deflection of the compass needle would also be reversed. Initially, Seebeck believed that the joined dissimilar metals became magnetically polarized when exposed to the temperature gradient, which caused the deflection of the compass needle and he called the phenomenon thermomagnetic effect. However, it was quickly realized that there was an electric current induced in the junction that deflected the compass needle by Ampere's Law. Then this kind of thermoelectric phenomenon was called the Seebeck Effect.

As the main topic of my dissertation is on materials research, I would only give a brief introduction of mathematical model in this section which could directly define the Seebeck Coefficient (also named as thermoelectric power or thermopower). Here is the equation describing V as the thermal electromotive force generated by the temperature difference.

$$V = \int_{T_1}^{T_2} \left(S_B(T) - S_A(T)\right) dT \qquad \text{Eq.1-1}$$

T_1 and T_2 are the absolute temperature of the two junctions. S_A and S_B are the Seebeck Coefficients of materials A and B, which are non-linear as a function of temperature and depend on the conductors' absolute temperature, material, and molecular structure. If changes of the Seebeck coefficients are effectively small in the measured temperature range, they can be considered as constants and the above formula can be approximated as:

$$V = (S_B - S_A) \cdot (T_2 - T_1) \qquad \text{Eq.1-2}$$

By Eq.1-3, we can easily find out the thermal electromotive force V is proportional to the temperature difference and if we set $(T_2 - T_1)$ unchanged, we need find a larger $(S_B - S_A)$ couples to get better V performance. In industry, as same as the way of making thermoelectric heat pump, a lot of small couple units are linked up to generate a large enough electric potential for application, like thermal couples, thermal diodes and thermoelectric generators, such as

radioisotope thermoelectric generators which are used for creating power from heat difference in spacecrafts.

The Peltier Effect

In 1834, J. C. A. Peltier found that the temperature could rise or fall at the junction of two dissimilar metals carrying small current, depending on the direction of the current.[4] Experimentally, the rate of intake or output heat was proportional to the magnitude of the current through the junction, which proved a kind of electromotive force residing at the junction. Finally, this kind of electromotive force was called Peltier EMF and the phenomenon is called Peltier Effect.

To quantitatively describe the Peltier Effect, the following equation is given out and Peltier Coefficient Π is defined as how much heat the current can carry per unit charge through the given material.

$$\dot{Q} = \Pi_{AB}\, I = (\Pi_B - \Pi_A)\, I \qquad \text{Eq.1-3}$$

$\dot{Q}$ is the Peltier heat adsorbed by the lower temperature side per unit time and I is the current made to flow through the circle. Π_{AB} is the Peltier Coefficient of entire couple while Π_A and Π_B refer to each individual materials. Basically since the current must be continuous across a junction, the heat flow will develop a discontinuity if Peltier Coefficient Π is different between the two sides of the junction. Thus a non-zero divergence at the junction will be induced and the heat must be accumulated or depleted, depend on the sign of the current I. Moreover, according to Eq.1-3 we can find the direction of heat transfer, mathematically the sign of $\dot{Q}$ on the left hand side of Eq.1-3, is controlled by the polarity of the current, the sign of I on the right hand side however the absolute value doesn't, which means we can control the application of the device,

cooling or heating, under the same efficiency. As Peltier Effect only depend on the current and the materials, $\dot{Q}$ can be added up by plenty of devices connected together and every single unit can be smaller in size which point out a way from the lab to the industry, could be called solid state heat pump or thermoelectric cooler (TEC). Nowadays, lots of companies put Peltier Effect into their products and make them more and more popular, such like portable refrigerators, beverage coolers, electronic component coolers, etc.

The Thomson Effect

Although it seems that the Peltier Effect and the Seebeck Effect have already covered all the information of thermoelectric phenomena, the Thomson Effect is really unique and important among the three. Thomson Effect was firstly talked in 1851, predicted in 1854 and experimentally observed in 1856 by William Thomson,[5-6] the great 1st Baron Kelvin, which described the heating or cooling by a current-carrying conductor which a temperature gradient. With a temperature between two ends, a current-carrying conductor, except for a superconductor, will either absorb or emit heat depending on the materials. Here is the point that Thomson Effect distinguish from the other two, which the Peltier Effect and the Seebeck Effect both require two dissimilar metals joined together but Thomson Effect can be observed on every individual metal.

To calculate quantitatively, assume a current density J occures through a homogeneous conductor, the heat production per unit volume, which represented by Q, is described by Eq.1-4.

$$Q = \rho J^2 - \mu J \frac{dT}{dx} \qquad \text{Eq.1-4}$$

ρ is the electrical resistivity of the material, $\frac{\mathrm{dT}}{\mathrm{dx}}$ is the temperature gradient along the wire and the constant μ is defined as the Thomson Coefficient. Looking at the Eq.1-4, we can clearly find that the first term on the right, ρJ^2, is nothing but irreversible Joule heat generated by the current and

the second term is what we are looking for, the Thomson Heat. The sign of the Thomson heat is determined by both temperature gradient and the direction of the current, which means the direction of heat transfer can be changed by changing the direction of current or make a reversed temperature gradient. What should be emphasized here is that, heat production in both the Peltier Effect and the Thomson Effect can be changed by the direction of current carrying on the conductors but the Joule heat is not. Thus the Joule heat effect in Eq.1-4 cannot be treated as a kind of thermoelectric phenomenon but the energy loss due to non-ideality in thermoelectric devices.

We have mentioned that the Thomson Effect is unique among the three thermoelectric phenomena as the Thomson Effect can be observed on every individual materials but not a joined couple, which means the Thomson Coefficient here is the only one that directly measurable from all three coefficient. However, we luckily have two equations relating these three coefficients, the Thomson Relationship, also known as the Kelvin relations. Therefore, we should treat only one, the Thomson Coefficient, as independent variable and calculate the others. Here are the Thomson relations.

$$\Pi = S \cdot T \qquad \text{Eq.1-5}$$

$$\mu = T\frac{dS}{dT} \qquad \text{Eq.1-6}$$

Here T is the absolute temperature. From Eq.1-5, we can find that the Peltier Coefficient is actually the product of the Seebeck coefficient and the Thomson Coefficient. And the by Eq.1-6, we can govern it to a much clear form Eq.1-7.

$$dS = \frac{\mu}{T}dT \qquad \text{Eq.1-7}$$

Now we get the idea that by integrating the Thomson Coefficient over the absolute temperature, the Seebeck Coefficient as the function of T is derivable. Thus the method to determine all three

coefficients, μ, S and Π, can be carried out like following step. Firstly, measure the Thomson Coefficient μ of the material over a wide temperature range, including the temperature close to zero, and get relationship $\mu_{(T)}$. Then by the Thomson relations Eq.1-7, do the integration and find out $S_{(T)}$. After that, use Eq.1-5, $\Pi_{(T)}$ is straight forwards. Till now, we get all the three coefficients as dependents of T for this kind of material and they all are absolute (i.e. single material) value. In principle, these work just need to be done on one kind of material as the Peltier Effect and the Seebeck Effect both taking place at the junctions and the relative values of the Peltier Coefficient and the Seebeck Coefficient can be directly observed. Therefore, by combining the known material (as reference value) with the unmeasured material, the absolute value of unmeasured materials can be calculated very easily.

Commonly, lead (Pb) is asserted that its Thomson Effect is zero. Though it is true that its three thermoelectric coefficients are small, they are in general non-zero. Thus wide temperature range measurement is carried on lead and the absolute value of its coefficients are calculated out as the functions of T which could be considered as the reference values for future experiments.[7]

1.2.3 Theoretical Model of Thermoelectricity

Since the Seebeck effect was discovered in 1821, the thermoelectric models have been studied more than 190 years. However, the improvement does not get faster until 1950. The most important parameter to characterize the performance of real thermoelectric devices is the thermoelectric figure of merit, $Z = S^2\sigma/\kappa$ with the units of $Kelvin^{-1}$, which was defined in 1957 by Ioffe.[8] In this definition, S is the Seebeck coefficient and the reason of appearance is self-explanatory. Because of the Joule heating, the electrical conductivity σ also gets involved. Passing through a thermoelectric element, Joule heat is generated by the current and can be

transported to the cold junction. The reason of thermal conductivity κ in here is that, the thermoelcetric devices also perform as the thermal insulator between the hot and the cold sides when applying as thermoelectric coolers or power generators. A high thermal conductivity will cause too much heat leakage between the hot and the cold sides thus make it hard to maintain the temperature gradient.

In many situations, dimensionless thermoelectric figure of merit, as $ZT = S^2\sigma\, T/\kappa$ which T is the average device temperature in SI unit. ZT is commonly cited instead of Z. Nowadays, widely used expression of thermoelectric properties are derived from the Boltzmann transport equation under the relaxation time approximation.[9]

$$\sigma = L^{(0)}, k_e = \frac{L^{(2)}}{e^2\, T} - \frac{L^{(1)}\, L^{(1)}}{e^2\, T\, L^{(0)}}, S = -\frac{L^{(1)}}{e\, T\, L^{(0)}} \qquad \text{Eq.1-8}$$

where

$$L^{(\alpha)} = e^2 \int \frac{d^3\vec{k}}{4\pi^3}\left(-\frac{\partial f_{F\,D}}{\partial E}\right)\tau\left[E_{(\vec{k})}\right]\left[\vec{v}_{(\vec{k})}\right]^2\left[E_{(\vec{k})} - u\right]^{\alpha} \qquad \text{Eq.1-9}$$

In these expressions, k_e is the electronic contribution to the thermal conductivity, e is the unit charge, $\vec{k}$ is the electron wave vector, $f_{F\,D}$ represents the Fermi-Dirac distribution, τ is the carrier (the electron or the hole) relaxation time, $\vec{v}_{(\vec{k})}$ is the electron group velocity and the u is the chemical potential. Thus when energy band is assumed as three dimensional parabolic and the relaxation time is assumed to be a constant, the expression of ZT comes out to be,

$$Z_{3D}T = \frac{\left[\left(5F_{3/2}/3F_{1/2}\right) - \xi^*\right]^2\left(3F_{1/2}/2\right)}{1/B_{3D} + 7F_{5/2}/2 - \left(25F_{3/2}^2/6F_{1/2}\right)} \qquad \text{Eq.1-10}$$

where

$$F_i(\xi^*) = \int_0^{\infty} \frac{x^i\, dx}{exp(x - \xi^*) + 1} \qquad \text{Eq.1-11}$$

$$B_{3D} = \frac{(m^*)^{3/2}}{3\pi^2}\left(\frac{2k_BT}{\hbar^2}\right)^{3/2}\ \frac{k_B^2\,T\,\mu_c}{e\,k_p} \qquad \text{Eq.1-12}$$

In Eq.1-10, ξ^* is normalized chemical potential by k_BT and k_B is the Boltzmann constant, F_i is the Fermi-Dirac integral defined as Eq.1-11, k_p is the phonon contribution to the thermal conductivity, μ_c is the carrier mobility and m^* is the effective density of states mass of carriers.

After thoroughly considered the Eq.1-10, we can find that there are actually only two free variables that can be engineered in searching high ZT thermoelectric materials and designing efficient thermoelectric devices, the ξ^* and the B factor. As described before, ξ^* stands for the reduced chemical potential which could be controlled by doping because doping could change the states density. Thus doping materials usually be carefully chose to optimize the thermoelectric performance of 3D bulk materials. The other free term in Eq.1-10 is the B factor, which could be affected by electron effective mass, the carrier mobility and the thermal conductivity contributed by phonon. By relationship of B factor and total ZT value, we can say the larger B factor gives the greater ZT value. Eventually, besides the doping, the research of thermoelectric materials and devices is often directed by finding a large B factor, which usually has the characteristics like a large effective mass and a high mobility for carriers and a low lattice thermal conductivity. Slack gave a name to this kind of materials in the book "CRC handbook of thermoelectrics",[10] which is phonon-glass electron-crystal materials (PGECs). Actually these two requirements are not necessarily exclusive to each other, that a high mobility needs a low mobility effective mass but a high density of states demands a large density of states effective mass. One example is the anisotropic media, no matter in bulk form or in superlattices, which have a small effective mass i.e. a high mobility in the current flow direction with a large effective mass i.e. a high density of states under the perpendicular directions to the current flow.

Here we must notice that the subscript 3D in Eq.1-10 and Eq.1-12 means there are several restriction on this model, such like isotropic relaxation time for both electrons and phonons, bulk density of states for electrons and holes and local equilibrium. Though this model, Eq.1-10, is one of the milestones during the development of the thermoelectric models, it has some defects especially when applying in nanomaterials. For the constant relaxation time assumption, a more realistic form of the relaxation time is given as $\tau \propto E^{\gamma}$, which depends on the scattering mechanism.[11] As an instance, optical phonons have $\gamma = 1/2$, while acoustic phonons have $\gamma = -1$. So that the *ZT* is also a function of γ which indicates that by controlling the phonon scattering mechanism could also improve the *ZT* value. And the bulk density of states for carriers means bands are parabolic to 3D bulk structure, however when the model enters field of nanomaterials where quantum structures and quantum effects dominate, the band structure has a considerably different density of states which requires changed expressions of ZT in Eq.1-10 and B factor in Eq.1-12.[12] The third one, local equilibrium approximation, also is a too much simplified assumption in nanomaterials though it is a pretty good one in bulk materials. As the meaning of local equilibrium, it assumed the electron deviate very slightly from their equilibrium distributions which only valid in the condition that the characteristic length on transport direction is much longer than the electron mean free path. However, in nanomaterials, particles always give out quantity of interfaces or the transport in superlattices usually along the perpendicular direction to the thin films. Moreover, the hot electron effect, which means an electron is not in thermal equilibrium with the lattice, is well known in semiconductor elements featuring high electric fields. All of these situations could make the local equilibrium assumption invalid and the Eq.1-10 could lose its foundation.

In order to recover these defects and make a model running under the affection of quantum structures, scientists have made great efforts in modifying the bulk thermoelectric models to the low dimensional thermoelectric models.

In 2003, Sofo et al. presented a calculation method for the electronic structure from the first principle calculations, which could incorporate the full band structure information in the calculation of thermoelectric coefficients and the relaxation time approximation was also included to calculate the transport coefficient.[13] A kernel of all transport coefficients, Ξ, was also defined as the transport distribution in their work, which includes all the necessary electronic information to directly obtain the thermoelectric coefficients for any given materials as shown in Eq.1-13.

$$S = \frac{e\,k_B}{\sigma} \int d\varepsilon \left(-\frac{\partial f_0}{\partial \varepsilon}\right) \Xi(\varepsilon) \frac{\varepsilon - u}{k_B T} \qquad \text{Eq.1-13}$$

where

$$\Xi = \sum_{\vec{k}} \vec{v}_{\vec{k}} \vec{v}_{\vec{k}} \vec{\tau}_{\vec{k}} \qquad \text{Eq.1-14}$$

$$\vec{v}_{\vec{k}} = \frac{1}{\hbar} \frac{\partial \varepsilon_{\vec{k}}}{\partial \vec{k}} \qquad \text{Eq.1-15}$$

Here $\vec{v}_{\vec{k}}$ is the group velocity associated with the state, u is the chemical potential, k_B is the Boltzmann constant and $\vec{k}$ is the solution of Boltzmann's equation Eq.1-16.

$$\frac{\partial f_{\vec{k}}}{\partial t} = -\vec{v}_{\vec{k}} \cdot \frac{\partial f_{\vec{k}}}{\partial \vec{r}} - \frac{e}{\hbar}\left(\vec{E} + \frac{1}{c}\vec{v}_{\vec{k}} \times \vec{H}\right) \cdot \frac{\partial f_{\vec{k}}}{\partial \vec{k}} + \left.\frac{df_{\vec{k}}}{dt}\right|_{scatt.} \qquad \text{Eq.1-16}$$

Another calculation work about the thermoelectric coefficients is using a tight-binding model with $sp^3d^5s^*$ orbits by Lee and Allmen in 2006.[14] They got the similar match result as Sofo did on Bi_2Te_3 experimental data.

With more and more valuable calculation work and models coming out, we are hopeful to handle the thermoelectric materials both theoretically and experimentally. After the prior

researches on this field, we fully believe that the success in engineering the property of thermoelectric nanomaterials and fabricating high *ZT* thermoelectric devices could definitely change the human-beings.

1.2.4 Thermoelectricity: Current State of the Art

Persistent efforts have been put into the thermoelectric field since 1950s, but till now, the highest ZT of dominant commercial materials based on Bi_2Te_3 and its alloys like p-type alloy $Bi_xSb_{2-x}Te_3$ is still remaining around 1. In past decade, enhancement of ZT has been reported by several groups in the following directions. (I) superlattices such as $Bi_2Te_3/SbTe_3$ and $PbSe_{0.98}Te_{0.02}/PbTe$.[15-16] (II) new bulk materials like lead antimony silver telluride and its alloy including skutterudites.[17-18] The current ZT value till 2003 was trimmed by Kanatzidis,[19] as shown in **Figure 1.2** and the development of ZT history was summarized by Bass,[20] in **Figure 1.3**.

The superlattice nanostructure surely could deliver a higher ZT value, nevertheless, it has been noticed that there is a great difficulty in usage of large scale energy conversion application. Comparing to the superlattice in the heat transfer and cost, bulk materials are more ideal for high temperature operations. While near the room temperature 0-250 °C, Bi_2Te_3 based materials still dominate, PbTe based materials show a proved thermoelectric ability in the temperature range 300-700 °C.

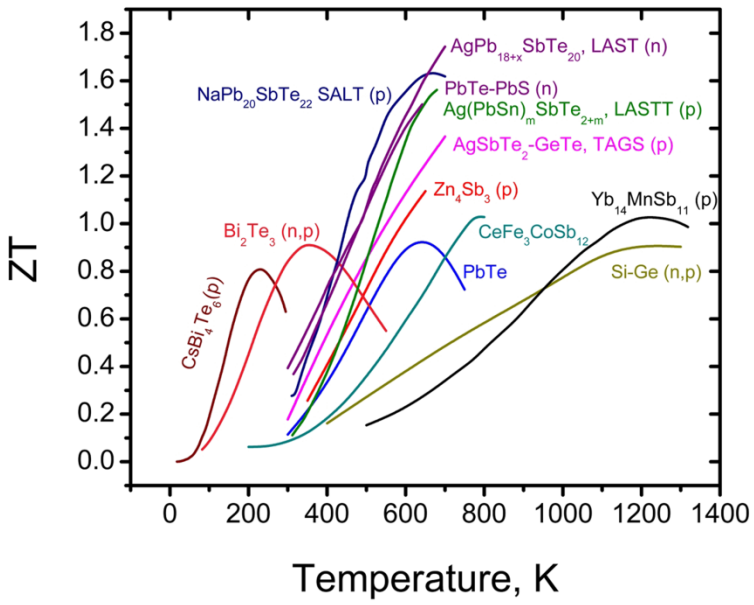

Figure 1.2 Dimensionless figure of merit vs. Temperature for current state of the art.

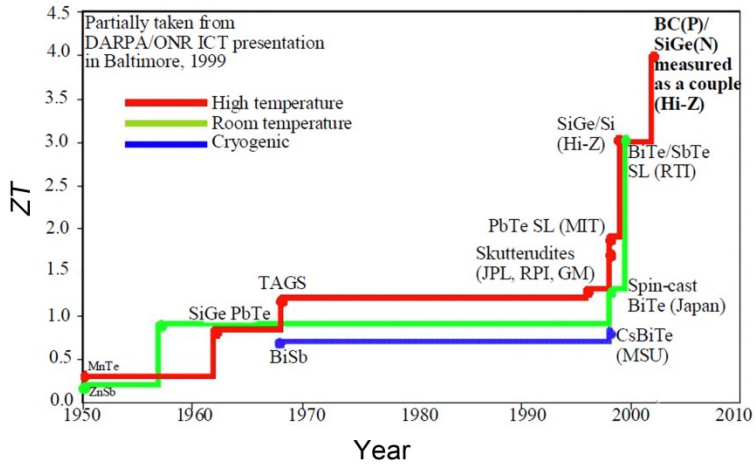

Figure 1.3 Development of the thermoelectric figure of merit.

PbTe has a FCC structure and fm3m space group with a cell parameter 6.459Å. Its energy gap is $0.25\ \text{eV}|_{T=0K}$ and $0.32\ \text{eV}|_{T=300K}$. With an intrinsic relatively low thermal conductivity, PbTe is considered as an ideal thermoelectric material in high temperature application. Lots of PbTe based thermoelectric materials have been discovered and the latest report about ZT of PbTe

based alloy materials is from Heremans and Snyder, which synthesized $Tl_{0.02}Pb_{0.98}Te$ alloy and got a ZT=1.5 at 773 K.[21] Thus PbTe based thermoelectric materials was selected as research object in our project.

1.2.5 Thesis Objective

The energy consumption has been concerned about globally and the environmental friendly property of thermoelectric technology as the method to convert waste heat back to electrical power has been well recognized. Many important materials have been found however the final device still need lots of problem to solve in order to fully exposure the promising thermoelectric effect. Thus this project will include the following targets: (1) designing phonon-glass electron-crystal nanocomposites based on nanocrystals as building blocks; (2) developing high efficient, low-cost and environmentally friendly synthesis approach for PbTe nanocrystals; (3) engineering interface properties to achieve phonon-glass electron-crystal nanocomposites; (4) finding proper sintering process for assembling bulk devices.

1.3 Antiviral Self-disinfecting Coatings

1.3.1 Virus, Tiny Infectious Agent

Virus, referring to poison and other noxious substances, comes from Latin and first used in English in 1392.[22] It is pretty interesting that this word first get meaning of "agent that causes infectious disease" in 1728 which 110 year earlier than the Russian biologist Dmitry Ivanovsky first discovered viruses in 1892.[22] At that time, it was believed that Chamberland-Pasteur filter, which pores smaller than bacteria, could collect all infectious agents. However, Ivanovsky found filtered leaf extracts from infected tobacco plants still remain infectious.[23] Unfortunately he suggested a toxin product from bacteria but missed the tobacco mosaic virus in one step, which was then discovered by the Dutch microbiologist Martinus Beijerinck in 1898.[24] Beijerinck repeated Ivanovsky's experiment and convinced the filtered solution containing a new type of infectious agent, but he called it *contagium vivum fluidum* which means soluble living germ and re-introduced the word *virus*. Later Wendell Stanley proved that viruses were actually particles.[23] On the other hand, the first animal virus, aphthovirus, which causes foot-and-mouth disease, was separated by Friedrich Loeffler in 1897.[25] The origin of viruses in evolutionary history of life is still unclear. However, viruses are important natural means to transferring genes between different species which increases genetic diversity and drives evolution.[26] The ability of switch on and off of genes and mechanism for introducing foreign genes into host cells are continuously attracting intense research interest over the world.

Up to date, over 5000 viruses have been described in detail and there are millions of different types.[27] Virus particles, also known as virions, consist of two or three parts: genetic material made from either DNA or RNA, a protein coat that protects these genes and play key role during infection, and sometimes an envelope of lipids that surrounds the protein coat when

they are outside of a cell. The average size of virions is 1/100 of the average bacterium thus most of them can't be directly observed with at light microscope. Most viruses have been studied have a diameter between 20 nm to 300 nm, for example, some filoviruses have a total length of 1400 nm but their diameters are only 80 nm.[28] Thus scanning electron microscope (SEM) and transmission electron microscopes (TEM) are employed in visualize virions, in which electron-dense stains are usually included especially in TEM.[29] By using solutions of salts of heavy metals such like tungsten, the scattering of region covered by the stain will be increased thus get higher contrast in TEM. There are two types of staining. Positive staining, which virions are directly coated with stain but obscure the virion details, the other is negative staining, which overcomes this problem by staining the background only. Moreover, atomic force microscopy (AFM) could be applied in mechanically probing the capsid morphology of virions.

The structure of virion can be divided into four types: helical, icosahedral, prolate and enveloped.

Helical: capsomers stack around a central axis to form a helical structure, which may create central cavity or hollow tube. This assembly results in rod-shaped or filamentous virions, could be either short and rigid or long and flexible. The genetic material is bound into the protein helix by electric interactions, negative charge from nucleic acid and positive charge on the protein. Therefore, the length of a helical capsid is related to the length of the nucleic acid wrapped in it and the diameter is dependent on the size and arrangement of capsomers, the perfect example for this type is well-studied tobacco mosaic virus, as shown in **Figure 1.4**.[30]

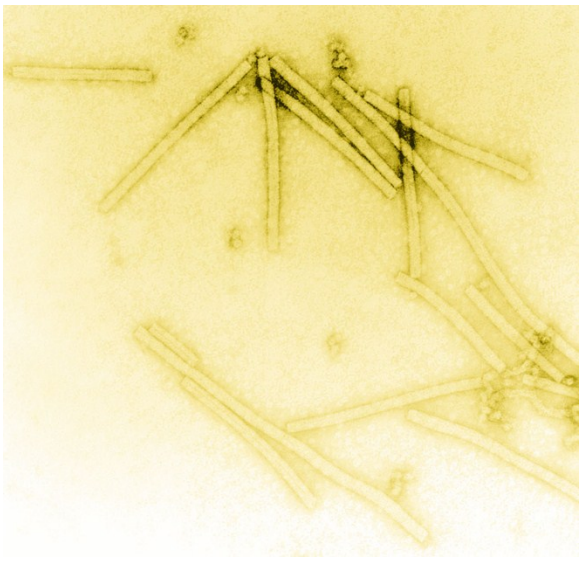

Figure 1.4 Tobacco Mosaic Virus negative stained with heavy metal.

Icosahedral: icosahedral or near-spherical shapes are observed in most animal viruses. A regular icosahedron is the optimum way of forming a closed shell from identical sub-units. Twelve is the minimum required number of identical capsomers and each of them consists of five identical sub-units. More than twelve capsomers will show a more spherical shape while maintain the same symmetry. Capsomers at the apex are surrounded by five other capsomers and called pentons. Capsomers on the triangular faces are surrounded by six other capsomers and called hexons. Usually hexons are flat and pentons are curved to form 12 vertices. Hexon and penton may be occupied by same type of subunits or different ones. A good example of icosahedral virion is the adenovirus, as shown in **Figure 1.5**.[31]

Prolate: prolate shape is kind of elongated icosahedron along the fivefold axis. It is a common arrangement of the heads of bacteriophages. It could be also imaged like a cylinder with caps at the both ends.

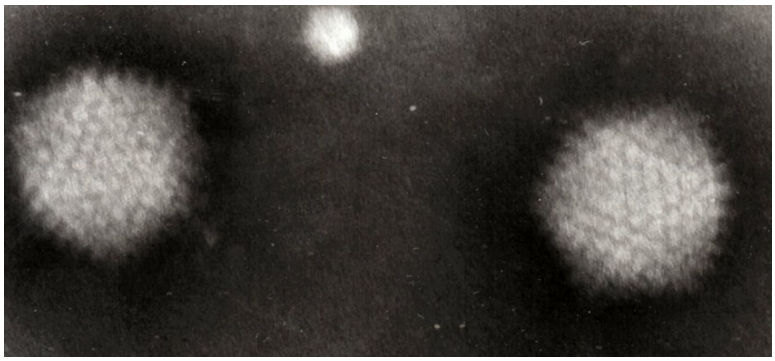

Figure 1.5 TEM image of adenoviruses with negative stain.

Enveloped: Some species of virus envelop themselves with an outer lipid double layer. The lipid membrane could come from one of the host cell membranes, such as nuclear membrane or endoplasmic reticulum. The lipid membrane is decorated with envelope proteins coded by the viral genome and host genome, which significantly related to infectivity of most enveloped viruses such like HIV and influenza virus, as shown in **Figure 1.6**.[32-34]

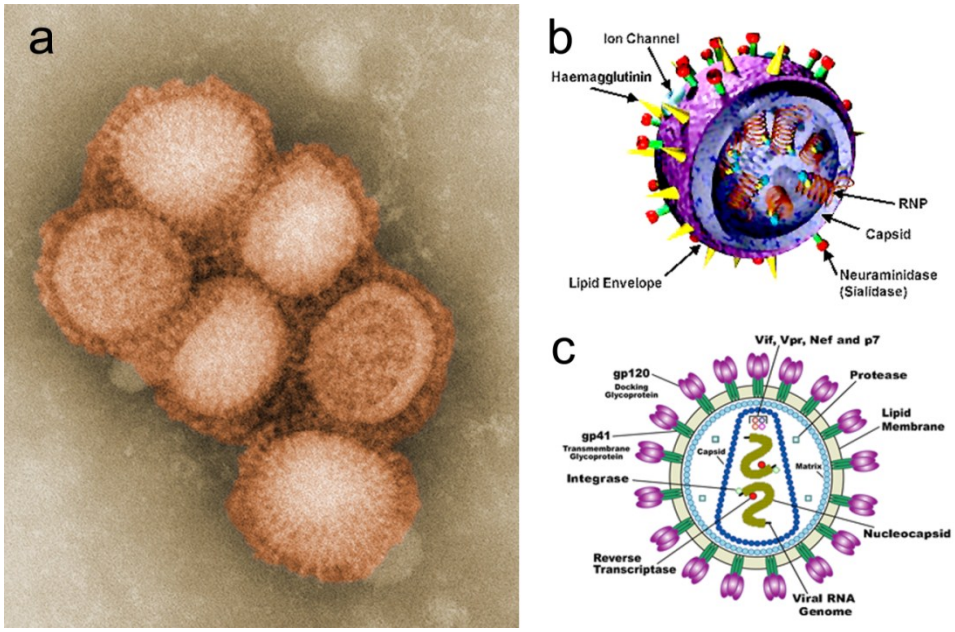

Figure 1.6 Enveloped viruses. (**a**) TEM image of influenza A viruses, (**b**) 3D illustration of the influenza A virus and (**c**) diagram of the HIV virus.

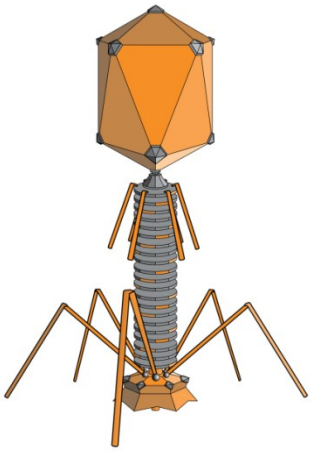

Figure 1.7 Diagram of enterobacteria phage T4 with artificial colors, which shows complex structure containing an icosahedral head, a helical tail and protein fibers.

Besides the four typical morphologies, some viruses present like complex of them. Their capsid possess neither purely helical nor purely icosahedral and may possess extra structure like protein tails or complex outer wall. For instance, enterobacteria phage T4 has an icosahedral head connected to a helical tail, which may have a hexagonal base plate with protruding protein tail fibers, as shown in **Figure 1.7**.[35] After a T4 attaches to host bacterium, it injects the viral genome through the tail, using it as a molecular syringe.

After summarized the structure types, let's talk about genome of virus. A virus has either DNA or RNA genes and is called a DNA virus or a RNA virus, respectively. Biologist David Baltimore, the Nobel Prize-winner, developed Baltimore classification system, which is based on mechanism of mRNA production.[36] Viruses must use host cell resource to generate mRNAs from their viral genomes to produce proteins and finish self-replication. However, different mechanisms are employed during this process. Viral genomes may be single-stranded (SS), double-stranded (ds), RNA or DNA, and may use reverse transcriptase (RT) or not. In addition, ssRNA viruses may also be sense (+) or antisense (-). A single strand of DNA is sense or

negative (-) if an RNA version of the same sequence is translated or translatable into proteins. The complementary strand of a sense is called antisense or positive (+). A single-stranded genome that contains both sense fragment and antisense fragment is said to be ambisense. In virology, positive-sense viral RNA signifies that the particular sequence may be directly translated into desired viral proteins, thus this strand RNA could also be treated like an mRNA. On the other hand, negative-sense RNA is the complementary mRNA and must be transcribed into a positive-sense RNA by an RNA polymerase then perform as an mRNA. Some viruses suck as influenza virus, have negative-sense genomes thus must carry an RNA polymerase inside the virion. Based on this information, the classification places viruses into seven different groups.

I. dsDNA viruses, e.g. adenoviruses, herpesviruses, poxviruses

II. ssDNA viruses: (+)sense DNA, e.g. parvoviruses, geminiviruses

III. dsRNA viruses, e.g. reoviruses, cystoviruses

IV. (+)ssRNA viruses: (+)sense RNA, e.g. picornaviruses, togaviruses, hepatitis C virus

V. (-)ssRNA viruses: (-)sense RNA, e.g. orthomyxoviruses, rhabdoviruses

VI. ssRNA-RT viruses: (+)sense RNA with DNA intermediate in life-cycle, e.g. HIV

VII. dsDNA-RT viruses, e.g. hepatitis B virus

Viruses have played a very important role in human diseases, examples including common cold, flu, chickenpox etc. and serious diseases like Ebola, AIDS, SARS and avian influenza. There is also possible connection between virus infection and neurological diseases.[37] Mechanisms at cellular level primarily include cell lysis. In multicellular organisms, the whole organism will suffer the effects if enough cells die. Besides disrupting of host's healthy homeostasis, viruses may also exist relatively harmlessly within an organism. The viruses caused

cold sores, herpes simplex virus, could serve as an example. They can remain a dormant state within human body which called latency. However, latent viruses sometime benefit the host for increasing immunity against bacterial pathogens, such as *Yersinia pestis*.[38]

Viral diseases could transmit vertically from mother to child or horizontally from person to person. Examples for vertical transmission include hepatitis B virus and HIV which new born babies already get infected from their mothers.[39] In addition but much rarer example is the varicella zoster virus can be fatal to the fetus and new-born baby even the infection is mild in adults.[40] Horizontal transmission is the most common mechanism of spread of viruses in population and causing epidemics. Examples can be listed as HIV by exchanging body fluids during sexual activity, hepatitis C virus by exchanging blood with contaminated transfusion or sharing needle, Epstein-Barr virus by exchanging of saliva by mouth, norovirus by ingesting contaminated food or water, influenza virus when virus contained aerosols are inhaled and dengue when insect vectors such as mosquitoes penetrate the skin of a host. The rate of spread depends on factors including population density, susceptible individuals, quality of healthcare and the weather. Control measures against epidemics are developed base on understanding the transmission of the virus. The first step is finding the sources and identifying the virus. Then viral transmission chain could be quickly broken by vaccines. But not always the vaccine exists, for example hepatitis B virus has vaccines but hepatitis C virus doesn't. On the later situation, usually infected people are isolated from the rest community and placed in quarantine. Most viral infection has latency called incubation periods, which range from few days to several weeks but are known to most infections. Failed in controlling the epidemics will result world-wide infection, the pandemics. The most cited example of pandemics is 1918 flu pandemic also referred as Spanish flu which caused by an unusual severe and deadly influenza A virus. The Spanish flu

lasted from Jan 1918 to Dec 1920, recent research suggested that as many as 100 million people were killed, equaled to 5% of world's population at that time. Also It is said that this flu killed more people in 24 weeks than AIDS has killed in 24 years, more in a year than the Black Death killed in a century.[41]

Because a virus uses host cell's metabolic pathway for replication, it is difficult to eliminate without using drugs that generally cause toxic effect to the host cell. The effective medical solutions to viral infections are vaccinations to provide immunity to infection and antiviral drugs that selectively interferes viral replication.

Vaccines are effective way of preventing infection by known specific viruses which could result in a dramatic reduction in morbidity and mortality. Vaccines can be divided into live-attenuated, killed viruses or viral proteins (antigens).[42] Live-vaccine is attenuated virus, the weakened form of original virus that cannot cause disease but enough to stimulate human's immune system. However, even attenuated vaccine could be dangerous when given to immunocompromised people that original diseases may occur. Biotechnology and genetic engineering techniques helps developing subunit vaccines, which use only capsid proteins as antigens to stimulate immune system, for example, hepatitis B vaccine.[43] There subunit vaccines are safe to immunocompromised community because no viral genomes contained. Vaccines are very effective in helping immune system quickly respond and block known stable viruses, however, they become pathetic when facing rapidly mutating viruses like influenza viruses and HIV. Antiviral drugs are particularly useful in these cases.

Antiviral drugs are often fake DNA building blocks, called nucleoside analogues, for viruses to mistakenly incorporate into their own genomes during replication thus interfere normal replication, translation and proteins coded base on viral genome.[44] The life-cycle of the virus is

then halted because of newly synthesized DNA or proteins are not functional. Also inhibitors could be antiviral drugs too, such like inhibitors targeting receptors on virion surface and binding to them eventually ending virus entrance of host cell, un-coating inhibitor to combat influenza viruses, retroviral integrase inhibitor to stop integrate synthesized DNA into the host cell genome like in HIV infection, inhibitor that block attachment of transcription factor to viral DNA, antisense molecule to critical section of viral genomes and the inhibitor preventing release of replicated viral particles such like neuraminidase inhibitor for treating influenza virus. Unfortunately, drug resistance is conspicuous as pathogens keep mutating over time. Thus more *in vitro* control methods for cutting the spread of virus thus preventing outbreak of epidemics and pandemics are of great importance.

1.3.2 Influenza A Virus, Pandemics and Human Being

The most common disease caused by virus should be the flu, which comes from a large virus family, the influenza A viruses. Influenza A viruses belong to the Orthomyxoviridae, they are negative sense single-stranded RNA viruses. Other genera of orthomyxoviridae are influenza B virus, influenza C virus, isavirus, thogotovirus and the sixth has recently been described,[45] in which first two and influenza A virus can cause influenza in vertebrates including humans, birds, seals and pigs, isaviruses infect salmon and thogotoviruses infect vertebrates and invertebrates like mosquitoes and sea lice.[46-48] Till now, all flu pandemics are caused by influenza A virus, which subtypes are categorized based on the type of two envelope proteins on their viral envelope, H or HA, short for hemagglutinin, totally 16 different types and N or NA, short for neuraminidase, totally 9 different types. The ratio of hemagglutinin to neuraminidase is usually 4-5 to 1 on a single virion. Even only a portion of subtypes are infectious to human, there have

already been three influenza pandemics in each century for the past 300 years by statistics.[49] Here are some famous influenza pandemics.

The earliest record of influenza pandemic is 1889-1890 Russian Flu, which was caused influenza A virus subtype H2N2. It began in Russia and rapidly involved entire Europe. Then it reached North America in December 1889 and recruited Latin America and Asia in February 1890. About 1 million people died in this Russian Flu.[50]

To talk about influenza pandemics, no one can avoid the severest pandemic in human history, Spanish Flu. Spanish flu last from 1918 to 1920 as mentioned before. It is the first H1N1 pandemic in the record and unusually severe and deadly. The pandemics started January 1918 ended in December 1920, even spread to Arctic and remote Pacific islands.[51] The first case of influenza were recorded in continental US, Haskell County, Kansas, later to the rest of Europe and to Spain.[52] The nickname Spanish Flu came from the earliest perceptions of the disease's severity. Unfortunately, World War I broke out and though it didn't cause the flu, but close troop quarters and massive troop movements helped spread of pandemic and possibly increased transmission and mutation rate. Recent research suggested that 50 - 100 million people were killed, equaled to 3-5% of world's population at that time.[53-54] Contrast to our common sense, the most victims were healthy young adults but not juvenile, elderly or weakened patients. Partial reason should be addressed as during World War I, troops got infected easily because of large population got too close. Other explanation came from research on tissue sample from frozen victims, which concluded that victims could be killed through a cytokine storm, thus strong immune system of healthy young adults ravaged their own bodies more likely.[55] Moreover, because of the war, severely patients were sent to crowded field hospitals, spreading deadly virus and virus mutated to much deadlier form thus the second wave began in France, Sierra Leone

and the United States in autumn of 1918.[56] In addition, virus-induced pulmonary consolidation and secondary bacterial pneumonias added the number of mortality.[57] Finally the pandemic disappeared in December 1920, one hypothesis was that virus mutated to a milder form and tapered off which usually happened in other pandemics. [55]

36 years later, another H2N2 pandemic came to human world. It was called Asian Flu, which first identified in Guizhou, China in early 1956, then spread to Singapore in February 1957, Hong Kong by April and the United States by June.[58] Some researchers believed that it mutated in wild ducks by combining with a pre-existed human strain.[59] Estimation from worldwide deaths varied widely from 1 to 4 million and with World Health Organization settling on about two million.

Later the Asian flu strain mutated to H3N2 and caused a milder pandemic from 1968 to 1969.[60] The first outbreak was recorded in Hong Kong in July 1968 and reached Vietnam, Singapore, India, Philippines, northern Australia and Europe by September 1968. In the same month, the virus entered California from returning Vietnam War Troops and later arrived in Japan, Africa and South America by 1969.[60] Approximately 33,800 people died in the United States.[61]

Recently, H1N1 influenza virus caused another pandemic in human being after 90 years of Spanish Flu, the 2009 Swine Flu. The first observation was in Mexico in April 2009, in the rest of spring, the disease spread worldwide rapidly. World Health Organization stated that "more than 214 countries and overseas territories/communities have officially reported confirmed cases of the influenza pandemic H1N1 infection, including over 18398 deaths." [62]

Looking through these data, the huge threaten keeps applying to human health care. Thus large quantity of research has been address on subtypes of influenza virus, infectious mechanism

and fighting against them. As mentioned before, vaccines have the best efficiency in antiviral measures. However, influenza A virus has too many serotypes, which make it hard to predict the coming outbreaks and quantity provide efficient amount of vaccine shortly after the pandemic starts. Moreover, the virus keeps mutating during both pandemics and the gaps, for example, it was proved that virus of 2009 Swine flu was different from one of 1918 Spanish flu, it contained sources from one human strain, one avian strain and two swine strains.[63] Thus besides developing vaccines against influenza virus, research efforts are donating into antiviral drugs at the same time.

It is known that there are two important envelope proteins decorated on influenza A virus' lipid envelope, the hemagglutinin (H1 to H16) and neuraminidase (N1 to N9) and their inhibitors could serve as antiviral drugs.

Hemagglutinin is an antigenic glycoprotein, which name comes from its ability to cause red blood cells to agglutinate *in vitro*. Hemagglutinin has two functions. Firstly it recognize target vertebrate cells and binding to the monosaccharide sialic acid on the target cell's surface. The cell membrane then engulfs the virus and encloses it in an endosome and later the host cell begins to acidify interior of endosome and transform endosome to lysosome in order to digest the inside contents. However, as soon as pH of the endosome drops to about 6.0, the second function of hemagglutinin wakes up. The original folded structure of hemagglutinin molecule becomes partially unfolded and releasing a previous hidden, very hydrophobic portion of its peptide chain which called fusion peptide. The fusion peptide acts like a grappling anchor by insert itself into endosomal membrane then the rest part of hemagglutinin refolds into an even more stable structure at lower pH. During the refolding, hemagglutinin retracts the anchor, fusion peptide, thus pulls the virus right up next to the endosomal membrane and cause fuse together of the

endosomal membrane and virus' own lipid membrane. Once this happened, the contents of virus are free to release into the cell's cytoplasm.

As hemagglutinin plays one of the key steps in the viral infection, neutralizing antibodies has been found as antiviral drugs. Inhibition could be realized by mirroring the two function of hemagglutinin, inhibition of attachment and inhibition of membrane fusion. The first type of antibodies could bind to hemagglutinin and physically block the interaction with sialic acid receptors on the target cells.[64-65] The second type of antibodies could bind to cross-linking parts of hemagglutinin's peptide together, thus block the key structural changes that drive the membrane fusion process.[66] Nevertheless, hemagglutinin inhibitors as antiviral drugs still have a long way to go.

Neuraminidase is a glycoside hydrolase that cleaves the glycosidic linkages from glycoproteins. At the end step of influenza virus' replication, new replicated virions are still linked to sialic acid receptors on the host cell membrane and neuraminidase can enzymatically cleave the sialic acid groups from host glycoproteins thus release the progeny viruses and spread them to uninfected surrounding cells. Neuraminidase could also prevent aggregation of viruses by cleaving the sialic acid residues from viral proteins.

Comparing to hemagglutinin, neuraminidase inhibitors as antiviral drugs are more successful in combating influenza infection. Currently there are already two drugs debuted to the US market and two under research. Zanamivir (Relenza),[67] administered by inhalation, works by binding to the active site of the neuraminidase. Oseltamivir (Tamiflu),[68] a prodrug administered orally, after converted by natural chemical processes in the liver it can serves as a competitive inhibitor of the activity of the viral neuraminidase upon sialic acid. Laninamivir (Inavir), [69] is another prodrug approved in Japan in 2010 and currently in Phase III clinical trials

in the US. The other experimental one in Phase III clinical trials is peramivir[70], administered through intravenous or intramuscular injection, acts as a transition-state analogue inhibitor of influenza neuraminidase. Various drawbacks have been reported like zanamivir is limited by inhaled route, thus treating asthmatics could induce bronchiospasm and oseltamivir could associates with adverse drug reactions include but not limit to nausea, vomiting, diarrhea, abdominal pain, headache, hepatitis, elevated liver enzymes, anaphylaxis and Stevens–Johnson syndrome.[71]

Therefore, besides focusing on the *in vivo* antiviral measures, vaccines and antiviral drugs, we should also seek *in vitro* disinfecting solution that prevent the spread of influenza A viruses and even other hazard microbes in the environment. Numerous sterilizing chemicals and methods have been developed, such like apply chemical disinfectants (chlorine, ozone, *etc.*), direct UV irradiation, ultrasonic and heat, but these methods are either harmful to human's health themselves or expensive and energy consumptive. Thus a good solution that can disinfect pathogens while not dangerous to human being, effective but less expensive and continuous working but controllable is highly demanded and attracts interests from both academia and industry.

1.3.3 Antiviral Coatings: Current State of the Art

TiO_2 semiconductors have been considered as the most popular photocatalyst family due to their chemical stability, non-toxicity, cheap availability and high photocatalytic reactivity, since the discovery of photosensitized decomposition of water on the TiO_2 electrode by Honda and Fujishima in 1972.[72] However, the inherent large band gap of 3.2 eV prevented native TiO_2 from utilizing visible-light but only UV light shorter than 387 nm, which is only 3-4% of energy

from solar light that reaches our earth. Moreover, on the purpose of continuously disinfecting hazardous virus and bacteria in in-door spaces, UV light should be void because of skin cancer risk and damage to eyes. Thus abundant research interests has been focused on designing, synthesizing and tailoring TiO_2 semiconductors in order to make ideal photocatalysts operating efficiently under visible-light and interior lighting. Up to now, quantities of remarkable research results have been reported and the main pathways includes but not limit to coupling TiO2 with a narrow band gap semiconductors, anion/cation doping or co-doping with two or more foreign ions, surface sensitization by organic dyes or metal complexes, surface modification like fluorination, and noble metal decoration.

Besides doped TiO_2, ternary oxides also attract broad research interests due to their promising ability as photocatalysts, *e.g.* Cu_2O,[73] Bi_2O_3,[74] $PbBi_2Nb_2O_9$,[75] and $BiVO_4$.[76] Within them, Bi_2WO_6 shows significantly higher absorption in the wavelength range over 440 nm than either Bi_2O_3 or WO_3 does, thus suggests enhanced photocatalytic activity under visible light illumination.[77] In 2010, Zhang et al. reported completely disinfection of *E. coli.* K-12 (5×10^7 cfu/mL) by AgBr-Ag-Bi_2WO_6 nanojuction as photocatalyst within 15 min.[78] The mechanism was investigated, that generation of $OH^{\bullet}$ and $O_2^{\bullet-}$ as reactive radicals were confirmed by DMPO spin-trapping ESR, damage of outer cell membrane was examined by testing K^+ leakage and destruction of the *E. coli.* K-12 was observed by TEM. Eventually, TEM images suggested that the bacteria could be complete destructed if the time frame was long enough.

1.3.4 Thesis Objective

Influenza A viruses, pathogens caused three deadly pandemics per century, keeps risking human's health even under today's medical technology. Untilizing functional semiconductor

materials, we were looking for developing self-disinfecting coatings, which could kill hazard virus, bacteria or even fungi thus control the outbreak of potential pademics, spoutaneously and continueously. Quantity of materials and chemicals have been reported, however, more convenient synthesis, economical materials, lower toxicity to human being and high disinfecting efficiency were always what scientiests pursuing. Thus we designed our self-disinfecting coatings should be: (1) spontaneously and continueously disinfecting hazard microbes, (2) physically and chemically stable for long-term working, (3) lower toxicity to human being while maintain enough efficiency, (4) synthesis and coating method should be facial, (5) technical possible and economics reasonable for large scale amplification.

1.4 Virus as Gene Delivery Vector

1.4.1 Genetic Disorders and Gene Therapy

As name indicated, a genetic disorder is an illness caused by abnormalities in genes or chromosomes. A genetic disorder may be a heritable or not, though some genetic disorders will affect the children but almost always the same disease actually are caused by new mutations of the DNA. Genetic disorders could be single gene disorder, to which about 4000 human disease relates, and multifactorial/polygenic disorders, which associate with the combined effects of multiple gene mutation, personal lifestyle and environmental factors. Typical examples of genetic disorders are Sickle-cell anemia, Familial hypercholesterolemia, red-green color blindness, hypertrichosis pinnae, Leber's hereditary optic neuropathy, asthma, diabetes, heart disease, cleft palate, mental retardation and some cancers.

Whether or not genetic disorder has been passed onto the embryo from parents could be found out by pre-implantation genetic diagnosis. Currently, existing genetic disorders rarely have effective treatments. Gene therapy has been tested as a possible treatment for some genetic diseases.

The common idea of gene therapy is using a functional gene to replace a mutated gene. It includes correcting a mutation directly and delivering a DNA to encode a therapeutic protein drug. The therapeutic DNA is capsulated in a "vector", which could do intracellular delivery and released the DNA for expressing by the cell machinery. Currently delivery methods can be divided into two major types, one is non-viral methods and the other is viral vector.

Non-viral methods are use naked DNA or DNA-polymer complex to transfect target cells, which can achieve large production and low host immunogenicity however usually can't compete the efficiency of viral vectors. As introduced before, all virus bind to their host and deliver their

genome to the host cell through efficient targeting process. It has been recognized as a plausible solution for gene therapy. As during the virus infection or delivery process, there is usually nothing related to viral genome, thus scientist could recombine viral vector with therapeutic DNA to achieve gene therapy, but the major drawback is the host immunogenicity. A number of viruses have been recruited into human gene therapy, like retrovirus, adenovirus, adeno-associated virus, etc. In which, great research interest has been exerted on adenovirus as a potent delivery platform.

1.4.2 Adenovirus, the Ultimate Infectious Agent

Adenovirus belongs to Group I in Baltimore classification, which means it has double-stranded DNA as genome. Adenoviruses are non-enveloped and icosahedral structured, usually around 90-100 nm, which represent the largest non-enveloped viruses. Unique spike-like fiber proteins are decorated on each penton base of the capsid. During the entry process, adenoviruses first attach knob domain of the fiber proteins to the host cell receptors, which are recognized as coxsackievirus adenovirus receptor (CAR) or CD46 (especially for group B human adenovirus). Then a specialized motif in penton base proteins interact with a co-receptor molecule called αv integrin, which finally results in endocytosis of the virion.

Once the virus gets into the host cell with in an endosome and the cell acidifies the endosome, capsid component of virus is altered to disassociate. These changes with the toxic nature of pentons result in release of the virion from endosome to cytoplasm. Aided by microtubules, the virus is transported next to nuclear pore complex where the virion gets disassembly and viral DNA is released and entered nucleus via nuclear pore. Finally, viral DNA associates with histones and starts replication.

By engineered to reduce adenovirus' immunogenicity, adenovirus vectors are nearly the most efficient class of vector in gene delivery towards the cell nucleus and can efficiently transduce in most tissues by direct injection.[79]

1.4.3 Polymer Nanogel: Current State of the Art

Polymer nanogel has been applied in drug delivery purpose for a while, specialized in gene delivery, Lemieux has reviewed some DNA delivery reports in 2000,[80] and lots of them were PEG, PEI, PSP, etc. and their copolymer based nanogel. More works including siRNA delivery have been published.[81-83]. One interesting work should be mentioned here that Lee et. al. synthesized a virus mimetic nanogel vector for delivery doxorubicin.[84] They built a hydrophobic copolymer core which containing doxorubicin, and two hydrophilic layers, polyethylene glycol as inner shell and bovine serum albumin (BSA) as outer shell also to mimic viral surface proteins. Moreover, folic acids were decorated onto BSA for targeting purpose. At pH 7.4, this kind of vector shrank its size to 55 nm and at lower pH like 6.4, the size of the vector changed to 355 nm and DOX were released. Also direct conjugating DNA with polymer molecules has been found as another solution for intracellular delivery.[85-88] Some reports about combining polymer technology and viral vector have been published.[89-91] One of them should be mentioned here is Fisher et. al. covalently coated adenovirus vector with poly-[N-(2-hydroxypropyl) methacrylamide] (pHPMA) to eliminate binding ability to the coxsackievirus and adenovirus receptor.[89] By incorporating basic fibroblast growth factor and vascular endothelial growth factor on the polymer-coated viral vector, retargeting of adenovirus vector has been achieved. Overall, current researches on viral vectors are mainly focusing on targeting regulation and lower the toxicity but stability is little considered for viral vectors.

1.4.4 Thesis Objective

Adenovirus with its ultimate infectious efficiency has been thoroughly studied and as gene delivery vector has been proved. However, long-term stability of these vectors is the limit on its application and makes it costly in storage and transportation. Thus solution to improve the stability and further control its targeting selection is of great value.

With polymer technique, polymer nanogel has been developed as intracellular protein delivery platform in our group by Yan and Du, et al. in our group.[92] The nanogel is a nanocapsule consisting of a thin permeable polymeric shell and a protein core, as a result, the stability against temperature, digestion, adverse pH condition and delivery efficiency has been significantly advanced. Lately, multi enzymes co-delivery system or quantum dot and enzyme co-delivery nanogel has been developed by Liu, et. al. in the same group. By migrating those strategies, a novel adenovirus nanogel is designed with following properties: (1) maintaining the infectivity of adenovirus, (2) controllability in size and zeta potential, (3) increasing stability, (4) possibility in targeting selectivity, (5) further modification on polymer shells.

Chapter 2 Synthesis of Thermoelectric Nanomaterials

2.1 Background Introduction

2.1.1 Motivation: Significance of Nano-size

Nanomaterials are also called as low-dimensional materials, such like superlattices, quantum wells, quantum wires, quantum dots and nanotubes, which offer new ways to control the electron and phonon properties of a certain materials. In the size that quantum effects come to the front, the energy distribution of electrons and phonons can be manipulated through changing the size of the structure, thus increasing the ZT value. Different length scales could create their own properties which belong to the given extent and could reflect on its ZT performance, although they have the same atoms and structures as their "bulk" counterparts.

As an instance, L. D. Hicks and M. S. Dresselhaus from MIT calculated the effect of quantum-well superlattice structures on Bi_2Te_3 and made a comparison with 3D bulk Bi_2Te_3 in the term of thermoelectric figure of merit in 1993.[93] They found that the best 3D figure of merit for Bi_2Te_3 was 0.52 but in quantum-well structure, it could easily exceed 1.5 as long as the layers were thin enough. Moreover, the thinner the layer was the larger factor over the bulk value achieved. Their calculation result is shown in **Figure 2.1**. In addition, they rapidly updated their calculation results for 1D nanowire structure of Bi_2Te_3 just one month later. The new calculation showed an amazing enhancement on the thermoelectric figure of merit due to the 1D wire structure, as shown in **Figure 2.2**. As mentioned that best $Z_{3D}T$ is 0.52, for a 2D quantum-well with width 10 Å the best $Z_{2D}T$ is 2.5 and for a 5 Å quantum well the best $Z_{2D}T$ reaches 5.[93] Respectively, a 10 Å width wire structure give out a $Z_{1D}T = 6$ while $Z_{1D}T = 14$ for a 5 Å wire.[94]

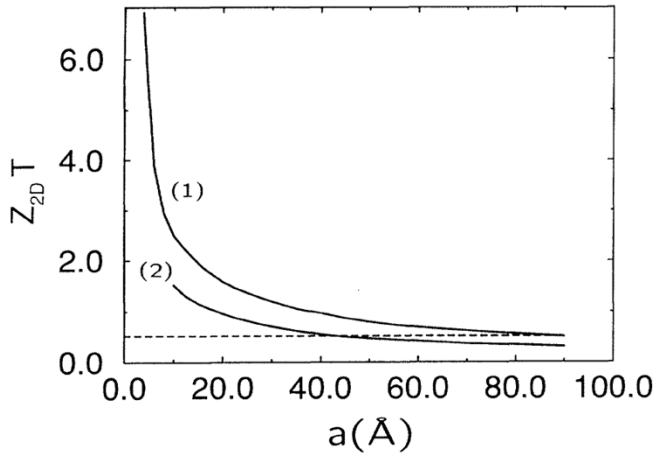

Figure 2.1 Plot of $Z_{2D}T$ vs layer thickness a for (**1**) $a_0 - b_0$ plane layers and (**2**) $a_0 - c_0$ plane layers. The dashed line indicates the best ZT for 3D bulk Bi_2Te_3.

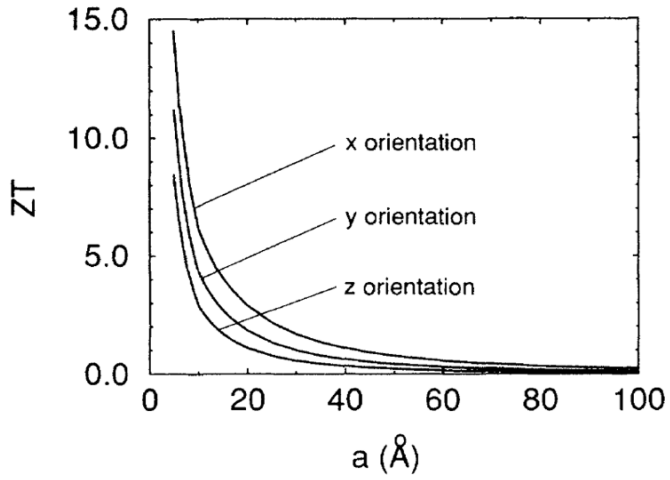

Figure 2.2 Plot of $Z_{1D}T$ vs wire width a for 1D wires fabricated along the *x*, *y*, and *z* directions.

Spark Plasma Sintering (SPS) is a popular technique that is usually employed to make nanoparticles to device or bulk materials for future process. In SPS, particles are loaded into a graphite die and a direct current is applied directly across the graphite die, as well as the particles in a conductive case. Therefore the heat is generated internally, which is totally different from conventional hot pressing. The facility we used in University of California, Riverside could go

up to 1100 °C with a pressure of 30000 N, which is under charge of Prof. Javier Garay from Mechanical Engineering of UC Riverside.

In conclusion, the thermoelectric figure of merit could be significantly enhanced by properly controlled microstructures, which could guarantee the mobility of electrons while make as more interfaces as possible to scatter the phonons. Nowadays, the nanomaterials especially nanoparticles and nanowires give out a promising ability in this field and they will demonstrate it to the entire world.

2.1.2 Research Objective

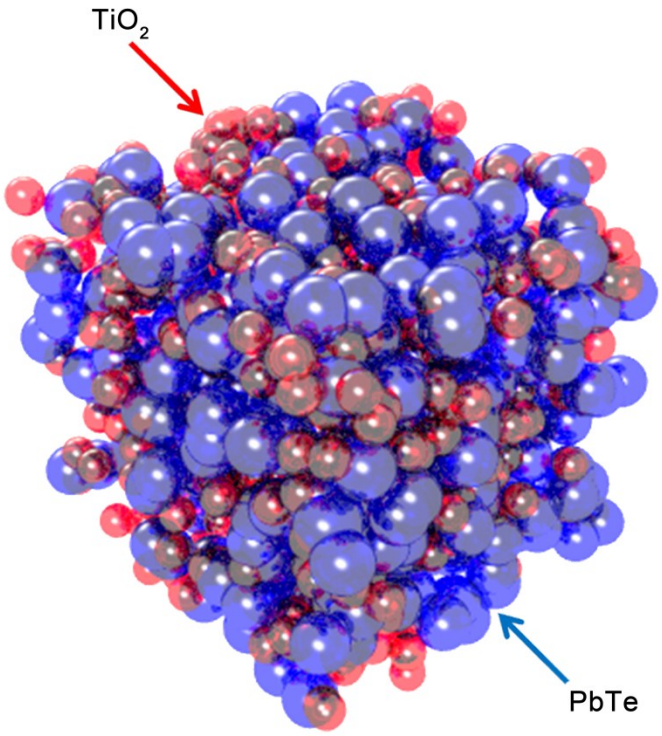

Figure 2.3 Proposed dissimilar nanocomposites as phonon-glass electron-crystal thermoelectric materials.

The efficiency of a thermoelectric material is defined by its dimensionless figure of merit, called ZT. Mathematically it is proportional to square of the material's Seebeck Coefficient,

electrical conductivity and average working temperature; and inversely proportional to its thermal conductivity. Phonon-glass electron-crystal structure has been proposed to improve the overall thermoelectric performance. As thermal conductivity is contributed by phonon transport and electronic contribution, the phonon-glass means scattering phonon transport to suppress the thermal conductivity and glass-crystal means electron transport should not be affected. Currently, superlattice materials can realize this idea but it is also well-known as hard synthesis and expense in amplification.

Dissimilar nanocomposites are proposed to achieve phonon-glass electron-crystal structure in a more facile way as illustrated in **Figure 2.3**. PbTe, a promising thermoelectric material with working temperature around 300-700 °C is selected as electron-crystal portion and TiO_2 is the phonon-glass portion. These two kinds of nanocrystals are synthesized with oleic acid as ligands, which supplied suspension ability in hexane and homogeneous mixing possibility. Oleic acid is later removed by chemical methods on the purpose to achieve full densified device in spark plasma sintering. Moreover the interfaces that generated between two types of nanocrystals further scattered transportation of phonons.

2.2 Experimental Procedure

2.2.1 Solvothermal Synthesis of PbTe Nanocrystals

In a typical solvothermal synthesis, 2.23 g of lead oxide and 8 mL of oleic acid were heated under nitrogen at 170 °C for about 0.5 hr. After lead oxide was completely reacted with oleic acid, 20 mL of toluene was added, stirred and cooled down to room temperature. Then, the solution was added with 15 mL of trioctylphosphine telluride (TOP-Te), which was prepared by dissolving 1.27 g tellurium powder in 11.4 g of trioctylphosphine (TOP) and diluted by toluene. The mixture, with another 50 mL of toluene added, was stirred for 10 min and then transferred to a 120 mL Teflon-lined stainless steel autoclave. The autoclave was sealed and maintained at 150 °C for 2.5 hr and cooled down to room temperature quickly with tap water. PbTe nanocrystals were precipitated by mixing the crude solution with acetone and the centrifuging resultant mixture at 3800 rpm for 20 min. PbTe nanocrystals were isolated by pouring off the supernatant solution. The resulting nanocrystals were purified and suspended in hexane to form a stable solution.

2.2.2 High Throughput Facile Synthesis of PbTe Nanocrystals in Aqueous Solution

In a typical synthesis, the Te precursor NaHTe was made from 1.27 g tellurium mixing with 0.8 g $NaBH_4$ in 10 mL of DI-H_2O and the flask was liquid sealed by 20 mL of Hexane. The system was placed in ultrasonic bath till the solution was totally transparent, purple like and no more hydrogen released. Then it was diluted to 50 mL by oxygen-free. After that, glucose-Pb complex as the Pb precursor was prepared from 3.33 g of $Pb(NO_3)_2$ with 2 g of Glucose and 1.5 g NaOH in 20 mL DI-H_2O. The solution was put into ultrasonic bath till transparent and diluted to 80 mL. Then, NaHTe solution was dripped into the glucose-Pb complex solution under N_2

protection and robust stirring. Separation was carried out by centrifuging at 3800 rpm for 5 min and purified by DI-H_2O and ethanol. After all, the black PbTe nanocrystals were dried under vacuum and usually a high yield of 80% could be easily achieved.

2.2.3 Reverse Micelles Assisted Synthesis of SiO_2/PbTe Core-shell Nanoparticles

In a typical reverse micelles assisted synthesis, 4.44 g of docusate sodium (AOT) was dissolved into 50 ml of cyclohexane, then 0.149 g of $Pb(NO_3)_2$, 0.0675 g of NaOH, 0.09 g of glucose, 15 μL of Ludox AS 30 (Purchased from Sigma-Aldrich, 30% aqueous solution) and 885 μL of H_2O was mixed to form uniform micro emulsion solution in a three neck flask under N_2 flow and vigorous stirring. For Te precursor, 1 mmol of Te powder, 10 ml of H_2O and 0.6 g of $NaBH_4$ were mixed and put into ultrasonic bath to form colorless NaHTe aqueous solution under a hexane sealing layer. Then NaHTe solution was transfer into an addition funnel with pressure equalization arm. After replace air to nitrogen in the funnel, the NaHTe solution was added into micro emulsion quickly and the precipitate was separated by centrifuging and thoroughly washed by H_2O.

2.2.4 Electrospray Assisted Synthesis of PbTe/SiO_2 Nanocomposites

For electrospray assisted synthesis, 10 mmol of NaHTe in 10 mL aqueous solution was prepared as described in Section 2.2.3, but not transferred to other container to avoid oxidization. 10 mmol of $Pb(NO_3)_2$ and 33 mmol of NaOH were dissolved in 10 mL of H_2O to form firstly white precipitate but finally clear solution, with the addition of NaOH, marked as solution B. Certain amount of Ludox hydrophilic SiO_2 nanocrystals was mixed in solution B, typically, 15% volume ratio of PbTe nanocrystals. Then solution B was loaded onto a syringe pump and outlet

needle was connected to positive electrode of a high voltage power supply and the tip was immersed into NaHTe solution. A ring like aluminum foil was set under the NaHTe container and connected to negative electrode. Typical voltage was like 13000 V to 20000 V and syringe pump speed was adjusted accordingly 0.1 mL/min to 2 mL/min. Finally as-prepared PbTe/SiO2 nanocomposites were washed by centrifuging and dried under vacuum.

2.2.5 Two Phase Approach Synthesis of TiO_2 Nanocrystals

In a typical experiment, 10 mmol of $Ti[OCH(CH_3)_2]_4$ and 80 mL of toluene were mixed in an 120 mL autoclave then 10 g of oleic acid was added. After that, 10 mL of DI-H_2O with 0.2 mL of *tert*-butylamine was introduced into the autoclave. Finally the autoclave was well sealed and heated to 180 °C. After 10 hr, the product was washed by centrifuging and purified by methanol and finally dispersed in hexane.

2.2.6 Chemical Removal of the Organic Ligands in Thermoelectric Nanocomposites

Method 1

$$CH_3(CH_2)_7CH{=}CH(CH_2)_7COOH + N_2H_4 \longrightarrow CH_3(CH_2)_7CH{=}CH(CH_2)_7CH_2\text{-}OH + N_2$$

$PbTe/TiO_2$ nanocomposites were immersed in 1.0 M solution of hydrazine in acetonitrile for 24 hr, then washed with acetonitrile and dried. Most of the oleic acid molecules were still attaching on the surface of nanocomposites according to FTIR spectra.

Method 2

$$CH_3(CH_2)_7CH{=}CH(CH_2)_7COOH + LiBH(CH_2CH_3)_3 \longrightarrow$$

$$CH_3(CH_2)_7CH{=}CH(CH_2)_7CH_2\text{-}OH + Li_xH_yBO_z$$

A new method was found later, which used super-hydrazine solution containing lithium triethylborohydride in THF. The nanocomposites were immersed in the super-hydride solution under nitrogen and put into ultrasonic bath for 30 min, then centrifuged and washed with THF. The procedure was repeated for 3 times. But oleic acid could not be removed thoroughly.

Method 3

$$CH_3(CH_2)_7CH=CH(CH_2)_7COOH + LiBH(CH_2CH_3)_3 + Me_3SiCl + THF \longrightarrow$$

$$CH_3(CH_2)_7CH=CH(CH_2)_7CH_2\text{-}OH + LiCl + Me_3SiH + B(CH_2CH_3)_3 + THF$$

Finally it was found that the addition of Me_3SiCl could make the reduction much more completely. The nanocomposites were immersed in 1 M super-hydride and 1 M Me_3SiCl solution in THF under nitrogen and put into ultrasonic bath for 30 min, then centrifuged and washed with THF and ethanol for 3 times.

Method 4

$$CH_3(CH_2)_7CH=CH(CH_2)_7COOH + NaOH \xrightarrow{\text{Ethanol, } NaBH_4, H_2O}$$

$$CH_3(CH_2)_7CH=CH(CH_2)_7COONa + H_2O$$

In addition, the solution of sodium hydroxide and sodium borohydride was found to remove the oleic acid. The nanocomposites were immersed in 1 M $NaBH_4$ solution in water and ethanol (volume ratio 1:1) under nitrogen at 60 °C. The pH was adjusted to 11 by sodium hydroxide. The mixture was stirred overnight then centrifuged and washed with water and ethanol. The use of sodium borohydride was to prevent the nanocomposites from oxidation in water.

2.3 Materials Characterization and Discussion

2.3.1 Solvothermal Synthesis of PbTe Nanocrystals

As synthesis of PbTe was very sensitive to the temperature and time and the yield per batch was not high enough to meet even single die of sintering. However by critically controlling the synthesis condition, the repeatability can be very good. **Figure 2.4** showed a TEM image for as-prepared PbTe nanocrystals.

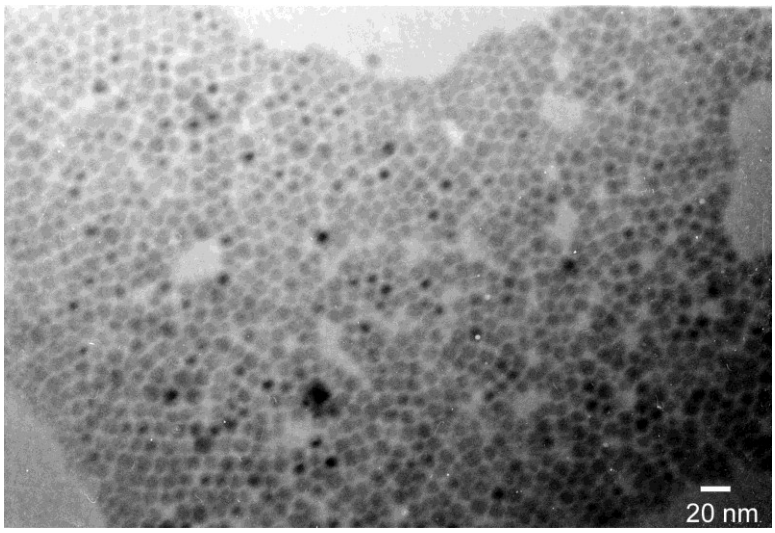

Figure 2.4 TEM image of solvothermal synthesized PbTe nanocrystals.

From **Figure 2.4**, the size of PbTe nanocrystal was around 10-15 nm and most of them had the cubic morphology. They could well disperse in hexane since the oleic acid as ligands has not been removed yet. And XRD in **Figure 2.5** showed the typical FCC structure of the nanocrystals and crystal size was about 13 nm by calculating from Debye-Scherrer Equation.

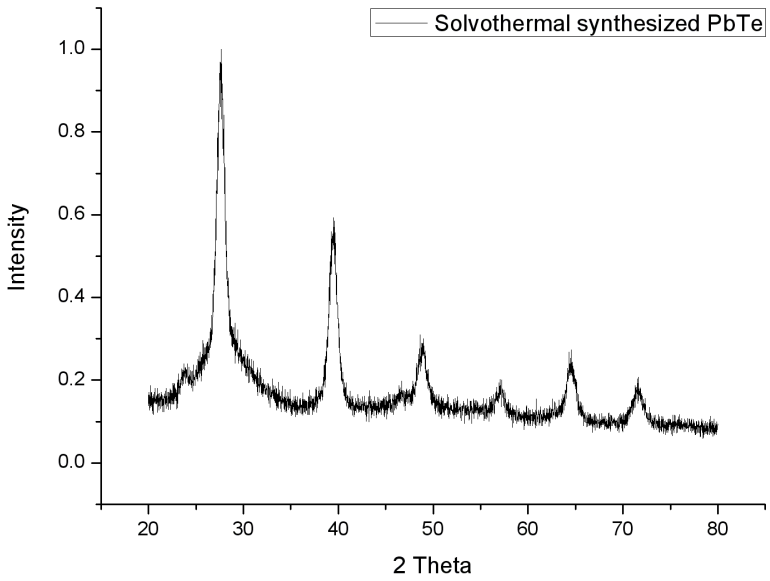

Figure 2.5 XRD pattern of solvothermal synthesized PbTe nanocrystals.

2.3.2 High Throughput Facile Synthesis of PbTe Nanocrystals in Aqueous Solution

Organic ligands can significantly decrease electrical conductivity of the device and may cause the out-gassing and huge thermal expansion during the application thus affect the stability of the device. To get rid of the organic ligands in the solvothermal synthesis and quantitatively synthesizing PbTe nanocrystals, we developed this ligands-free synthesis method in aqueous solution.

Aqueous solution synthesis usually gave out a really high yield however the PbTe nanocrystals were not totally separated as solvothermal synthesized ones but connected together to form a network as seen in **Figure 2.6**. The average particle size of the aqueous solution synthesized PbTe nanocrystals was around 10 nm, which was similar as solvothermal synthesized samples. **Figure 2.7** showed the XRD pattern of as-prepared PbTe nanocrystals, which indicated a well-defined FCC structure with the Fm3m space group (a = 6.459 Å).

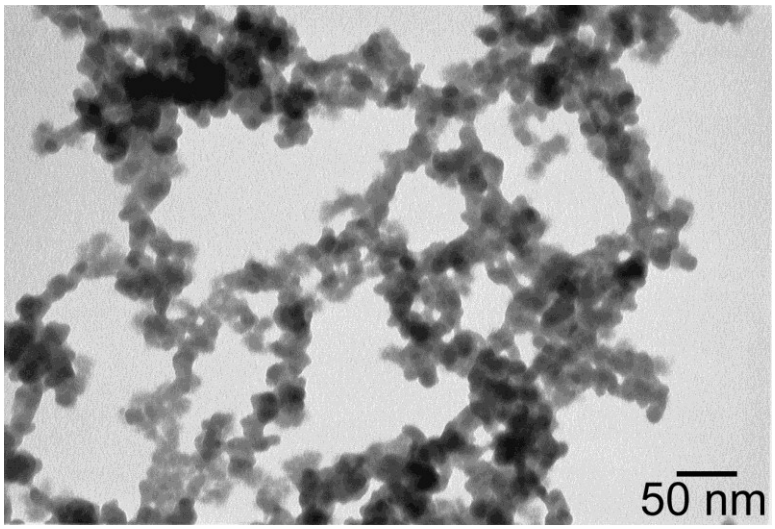

Figure 2.6 TEM image of aqueous solution synthesized PbTe nanocrystals.

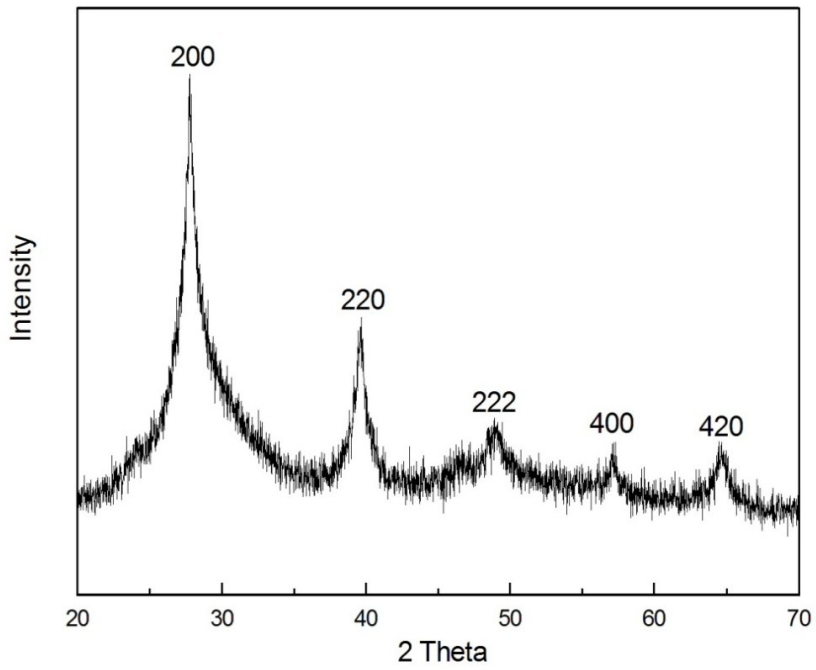

Figure 2.7 XRD pattern of aqueous solution synthesized PbTe nanocrystals.

2.3.3 Reverse Micelles Assisted Synthesis of SiO_2/PbTe Core-shell Nanoparticles

By controlling the ratio of surfactant, oil phase and aqua phase, stable micro emulsion could be prepared with controllable emulsion size. Each little droplet could be considered as a

tiny batch, and surface reaction could be introduced. By micro emulsion assisted synthesis, we can pack nanocrystals as the core into another nanocrystal as the shell, such like silica as core and PbTe as shell. Silica is known with a lower thermal conductivity and we have already synthesized PbTe nanocrystals network in aqueous solution, thus synthesis of these two kinds of nanocrystals in core-shell structure should be able to further improve the thermoelectric property.

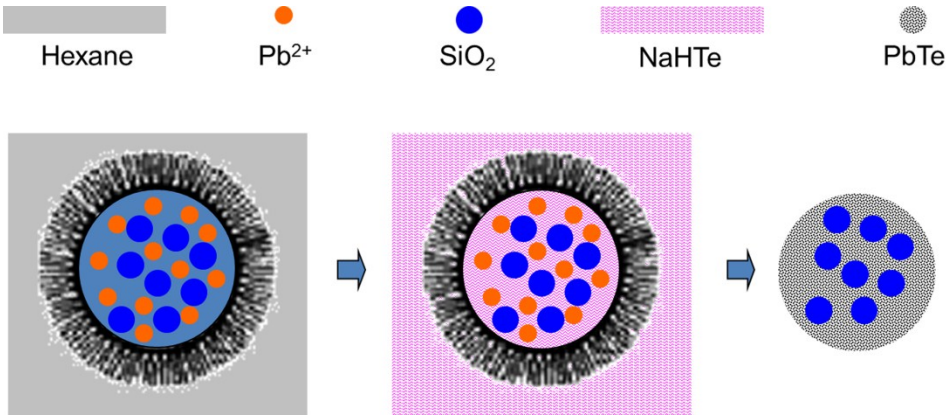

Figure 2.8 Sketch of micro emulsion assisted synthesis of SiO_2/PbTe core-shell nanoparticles.

Figure 2.8 gives out a sketch of micro emulsion assisted synthesis. Firstly use AOT, hexane and water to form micro emulsion and silica solution is introduced into the tiny batch. Then NaHTe is added into the micro emulsion quickly and the core-shell structure should be settled down by the fast reaction between Pb^{2+} and Te^{2-} at the room temperature.

However, the problems in this approach are pretty hard to deal with. The first problem is the yield. As the amount of water in this micro emulsion is strictly limited, the solubility of Pb precursor determined the total product we can get. Though we have already tried $Pb(NO_3)_2$ and $Pb(CH_3COO)_2$, which have better solubility in water than others do, only small amount of nanoparticles at the order of milligram could be prepared per batch. The second problem is the concentration of NaHTe. As mentioned before, water amount is strictly controlled in this micro

emulsion but NaHTe is water solution and will be added into the system, which means the micro emulsion is getting destroyed during the adding of NaHTe. Although as long as the reaction rate of Pb^{2+} and Te^{2-} is fast enough, the silica still can be wrapped inside the micro emulsion rather than been repelled out. In one word, higher concentration NaHTe should be suitable. However, NaHTe solution must be fresh made and the side product ($NaBO_2$) is not able to dissolve very well in the water then high concentration may cause a white deposition in the solution which will affect the later synthesis for core-shell structure. Thus a proper concentration of PbTe should be carefully determined. The third problem is the oxidization of NaHTe. Fresh made NaHTe solution could get oxidized to Te in several second if exposed to the air. Te could not be separated by centrifuge or solvent extraction. Although chemically it is possible to get rid of it by acid washing, the best way is prevent it from happening. So nitrogen or argon environment for synthesis is required. The forth problem is that silica will melt at high temperature not only during the SPS or application. Thus changing the device assembling method, finding a proper working temperature range is waiting for figuring out.

Here are characterizing results for micro emulsion assisted synthesis. **Figure 2.9** showed the SEM image of as-prepared SiO_2/PbTe core-shell nanoparticles, highly homogenous morphology of nanoparticles has been achieved and from EDS spectra in **Figure 2.10**, most of silica has been successfully wrapped in and homogenous distributed.

XRD was carried out and shown in **Figure 2.11** to determine the crystal structure and the grain size. By which we figured out that the crystallized part of nanocomposites was PbTe with a FCC structure and grain size was about 25 nm without impurity. .

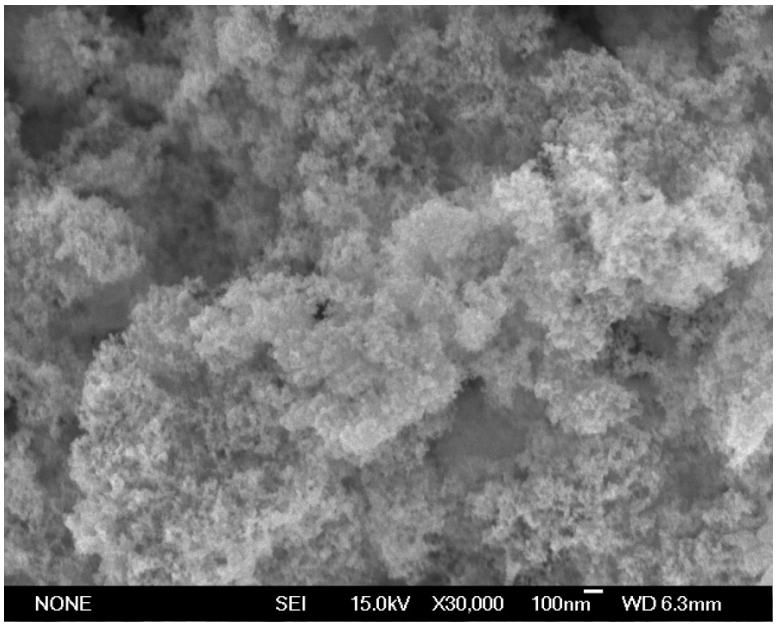

Figure 2.9 SEM image of micro emulsion assisted synthesized SiO_2/PbTe core-shell nanoparticles.

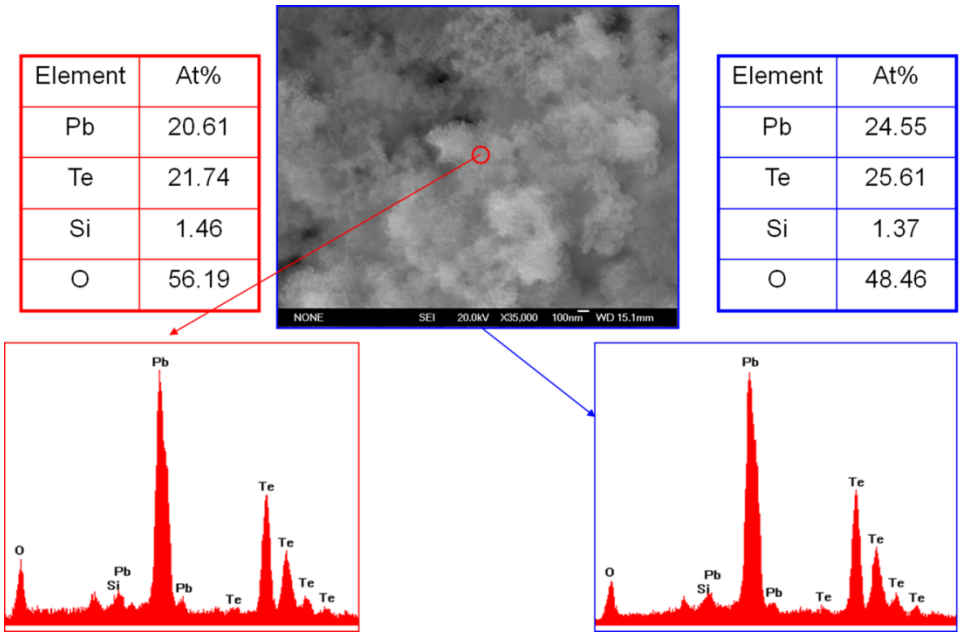

Figure 2.10 EDS spectra of as-prepared SiO_2/PbTe core-shell nanoparticles. Red one is the element ratio of the small point; blue one is the element ratio of the whole window.

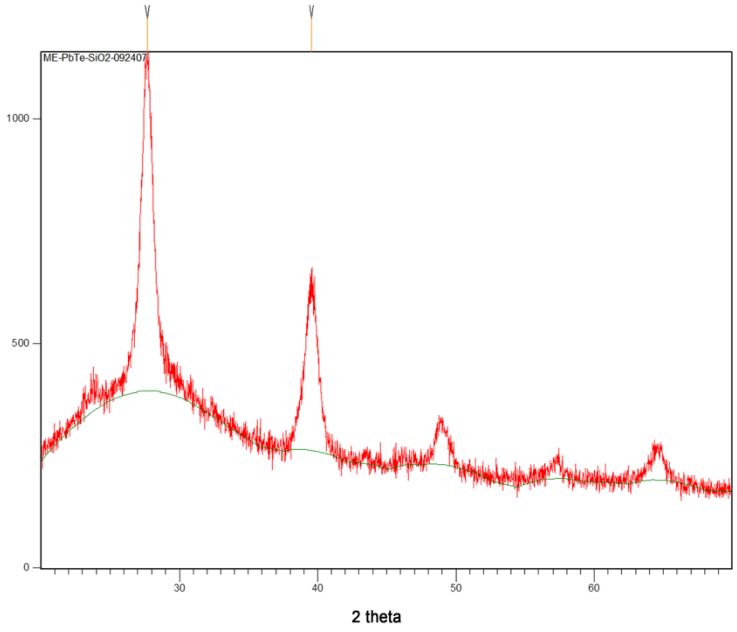

Figure 2.11 XRD pattern of as-prepared SiO_2/PbTe core-shell nanoparticles.

In conclusion, the concept of micro emulsion assisted synthesis has been approved and problems have been addressed to solve. HRTEM characterizing will be necessary to determine whether they are core-shell structure or not. However to get enough quantity of PbTe/SiO_2 nanocomposites, assemble them to final device and find out the ZT value is quite not a work worth to do. Its low throughput and expense in solvent and surfactant severely limit scale-up applications of micro emulsion assisted synthesis. Thus this method has been abandoned and efforts have been focused on how to make fully condensed devices.

2.3.4 Electrospray Assisted Synthesis of PbTe/SiO_2 Nanocomposites

Electrospray is widely used in many field and synthesis conditions are easily controlled. By extremely high voltage like 13000 V to 20000 V, which are further enhanced by aspect ratio of selected positive electrode, the precursor droplet could be atomized. Then after a dynamically

non-equilibrium process or fast chemical reaction, we can achieve the nanocrystals. Here we want to employ this method to prepare $PbTe/SiO_2$ nanocomposites.

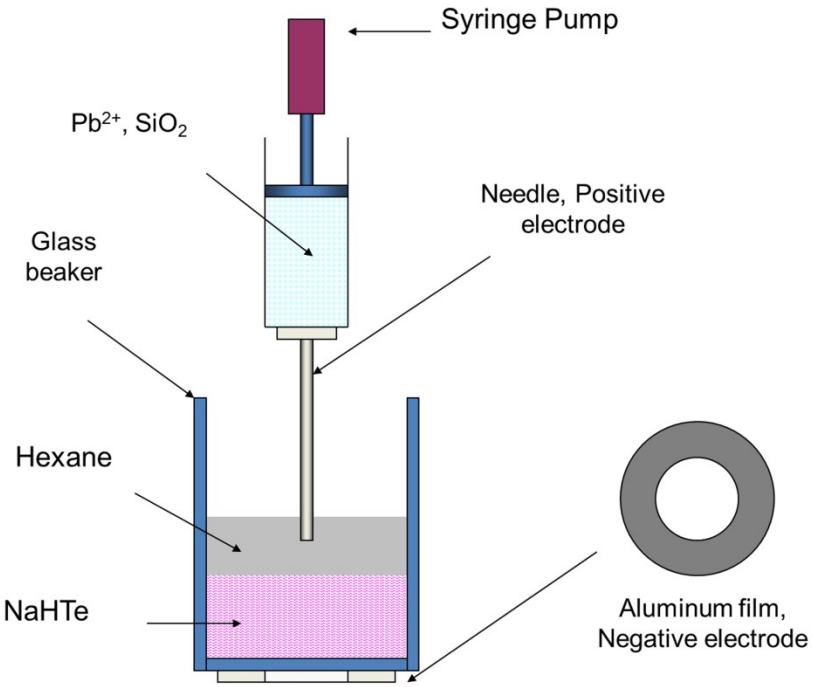

Figure 2.12 Sketch of electrospray assisted synthesis of $PbTe/SiO_2$ nanocomposites.

As in aqueous solution synthesis, NaHTe is freshly prepared but kept in the bottle without any transfer to avoid oxidization. For Pb precursor, we don't have to use glucose anymore, just water solution of pure $Pb(NO_3)_2$. The Pb precursor is filled into a syringe pump and connected to electrospray device and directly sprayed into the NaHTe solution. Silica is introduced into the Pb precursor to see if nanocomposites could form, as shown in **Figure 2.12**.

From SEM image in **Figure 2.13**, the homogenous morphology and narrow size distributed nanocrystals were observed. There is no way to distinguish the two types of nanocrystals in SEM images. The EDS data told that concentration of SiO_2 was much lower than the designed amount. And by XRD result, the calculated grain size of PbTe was 15 nm.

Comparing the size of selected silica, which was 22 nm, we thought that because of lacking interaction between PbTe and SiO_2 nanocrystals, the SiO_2 may have been washed away during centrifuge and leaves PbTe alone.

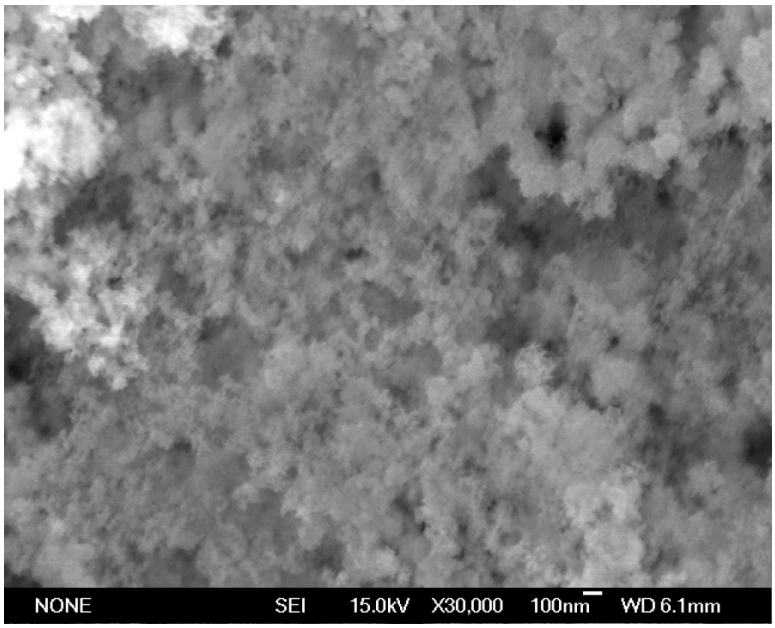

Figure 2.13 SEM image of electrospray assisted synthesis of PbTe/SiO_2 nanocomposites.

Therefore advantages as easy handling, low cost and high yield of electrospray assisted synthesis have been demonstrated. Some other materials should be found, which could have an interaction with PbTe molecule to achieve high yield in final nanocomposites and perform as adiabatic domain in the final device.

2.3.5 Two Phase Approach Synthesis of TiO_2 Nanocrystals

TiO2 is a kind of ceramic materials with a high resistance to heat transfer. Thus it is employed to form homogeneous nanocomposites with PbTe nanocrystals which could lead to reduced heat conductivity and a maintained electrical conductivity.

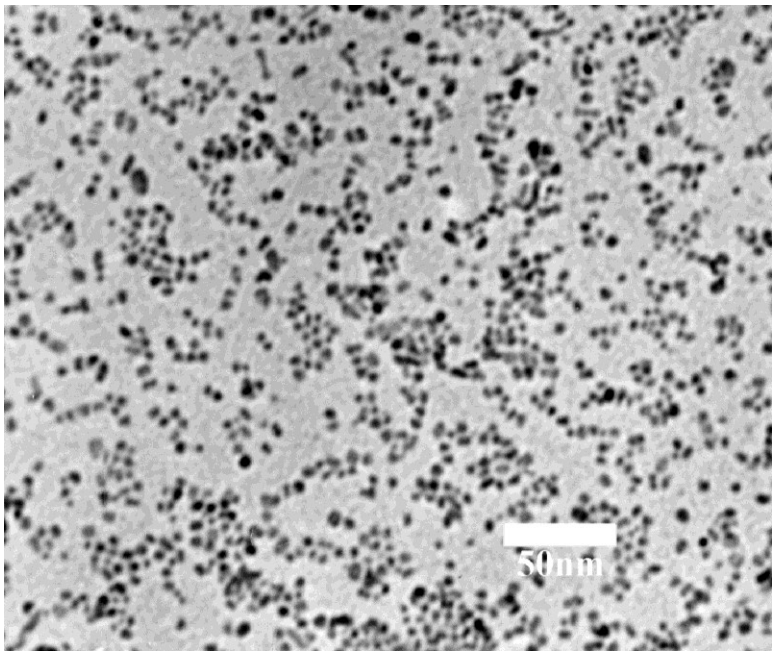

Figure 2.14 TEM of two phase approach synthesized TiO_2 nanocrystals.

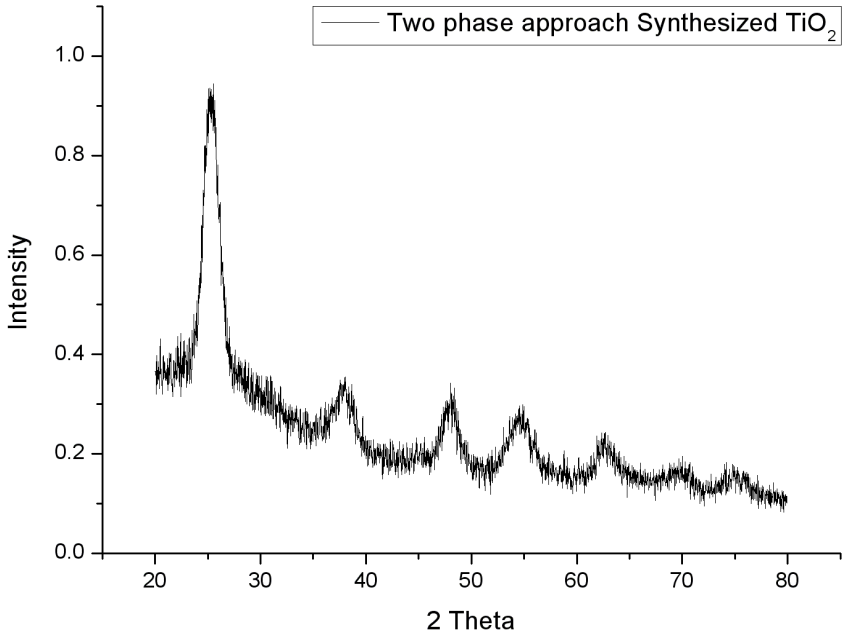

Figure 2.15 XRD of two phase approach synthesized TiO_2 nanocrystals.

At the time when TiO_2 nanocrystals came out from the autoclave, the color of the solution was light yellow. After rinsed by methanol, the side products were removed and solution

of color turned to white in hexane. **Figure 2.14** showed a typical morphology of the as-prepared TiO_2 nanocrystals. The nanocrystals were well dispersed and the size distribution was pretty narrow. The crystal size was calculated as around 6 nm by Debye-Scherrer Equation from XRD data of shows in **Figure 2.15** and the peak position shows that TiO_2 was of rutile phase.

2.4 Assemble Thermoelectric Devices for Application

2.4.1 Mixing and Hot Plate Drying of PbTe/TiO_2 Nanocomposites

Firstly, around 2 g of solvothermal synthesized PbTe nanocrystals in hexane solution was transferred to a small flask. After all the hexane evaporated, the dried PbTe nanocrystals were weighted. Then the same process was done on the as-prepared TiO_2 nanocrystals. By calculation, the mixture should have a volume ratio of 85:15, PbTe to TiO_2. Then the proper amount of each solution was mixed in a large flask and robust stirring was applied to make sure the homogeneous mixing. Meanwhile, an 18 inch silicon wafer was cleaned by ethanol and following by 70% nitric acid from Sigma-Aldrich, finally it was rinsed by DI-H_2O and dried in vacuum oven.

The cleaned and dried silicon wafer was heated to around 80 °C on a heat pot then the well-mixed PbTe/TiO_2 nanocrystals in hexane solution was dripped slowly onto the wafer. After the hexane was totally evaporated, the wafer was cooled down and well mixed nanocomposites were scratched off by a clean blade and collected in a 25 mL glass bottle.

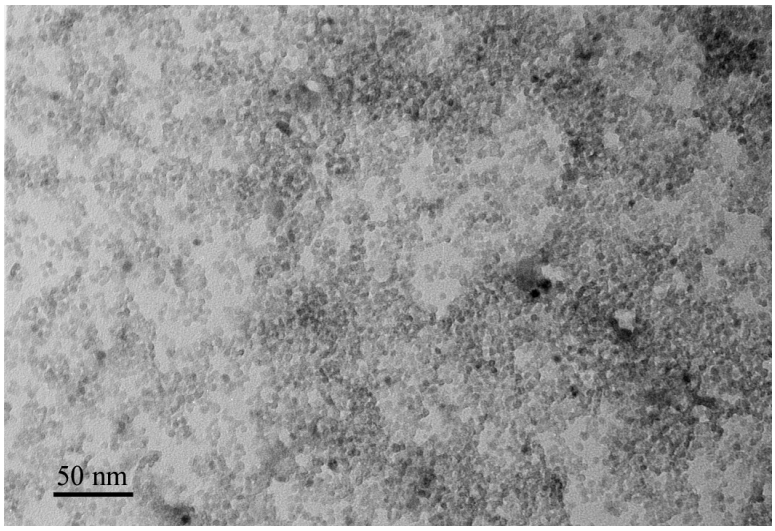

Figure 2.16 TEM image of the PbTe/TiO_2 homogeneous mixture.

In hot plate drying approach, the PbTe was made by the solvothermal method and the TiO_2 was synthesized through two phase approach. Their size and disperse ability were quite similar which were the advantage for homogeneous mixing. **Figure 2.16** showed the homogeneous mixture in the solution. The PbTe had darker contrast while the TiO_2 had lighter one. It suggested that the mixing was pretty uniform and no significant phase separation happened.

Figure 2.17 was the SEM image (**a**) and EDX mapping (**b, c, d,** and **e**) from solid state PbTe/TiO_2 nanocomposites after solvent got evaporated. **Figure 2.17c**, **d** and **e** showed the exactly the same pattern which suggested that Pb, Te and Ti, respectively, had the same distribution in the considered area, i.e. the homogeneous mixing has been successfully achieved.

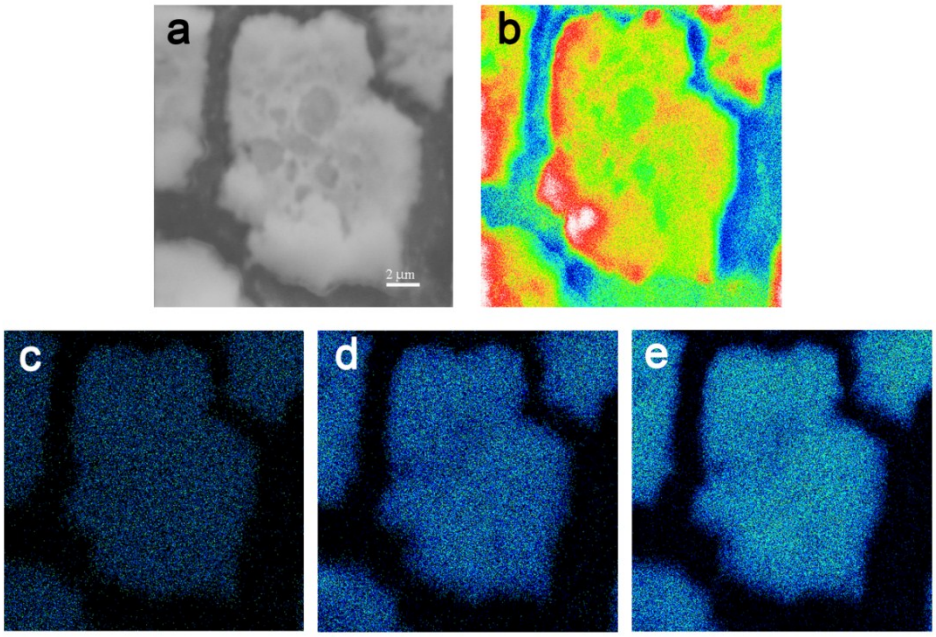

Figure 2.17 SEM and EDX mapping of PbTe/TiO_2 nanocomposites in solid state. (**a**) is the SEM picture of a cluster after solvent got totally evaporated; (**b**) is the mapping of all kinds of elements; (**c**) is the EDX mapping of Pb; (**d**) is the EDX mapping of Te; (**e**) is the EDX mapping of Ti.

2.4.2 Removing the Organic Residue

Glucose has been used to prepare large-scale production of PbTe nanocrystals in aqueous solution. Considering the weak interaction between glucose and PbTe, PbTe nanocrystals were washed repeatedly to remove resident glucose using ethanol and water, and dried in vacuum. FTIR study was applied and indicated that the glucose was completely removed by this method. However, the problems have come from removing oleic acid from PbTe/TiO_2 nanocomposites.

Oleic acid was employed during the solvothermal synthesis for PbTe nanocrystals and two phase synthesis of TiO_2 nanocrystals, but it interacted with metal and metal oxide surface too strongly that created significant difficulties in their complete removal. However complete removal of the organic ligands in the nanocomposites was critical to achieve fully condensed and robust sintered samples. In order to make crack free samples, four solutions were developed in removing oleic acid and final results indicated that two of them ($LiBHEt_3$/Me_3SiCl and $NaBH_4$/NaOH) were very efficient to remove the OA completely, i.e. Method 3 and Method 4 in Section 2.2.6.

Thermogravimetric analysis (TGA) was conducted to compare the efficiency of the above mentioned methods, and the plots are shown in **Figure 2.18**. The samples were first heated to 100 °C under argon at a heating rate of 10 °C per min and held for 10 min to remove the residual solvent. Then temperature was increased to 600 °C at the same heating rate and held for 10 min. The samples were then exposed to air for 10 min before temperature was decreased to room temperature. The as-prepared sample **Figure 2.18D** (before removing OA) showed that 17% of the organic component was removed during heating, following by another 1% weight loss when they were exposed to air, due to the combustion of the residual carbon. While for the samples after chemical treatment, there was no weight loss when exposed to air, indicated that

almost all the organic components have been removed at the sintering temperature, i.e. 600 °C. For the sample washed by Method 2 (**Figure 2.18E**), there was about 6.4% of the weight as organic components lost after the treatment. It was very excited that, for samples washed with Method 3 and 4 (**Figure 2.18C** and **Figure 2.18F**, respectively), no organic component was detected, indicated that the oleic acid has been totally removed by these two methods.

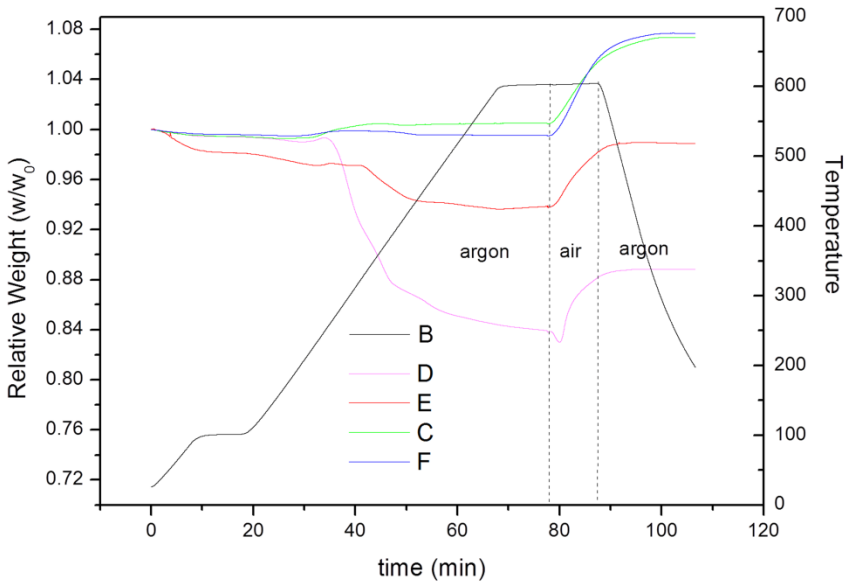

Figure 2.18 TGA plots of (**B**) temperature, (**D**) As-prepared $PbTe/TiO_2$ mixture, (**E**) $PbTe/TiO_2$ mixture after treatment with $LiBHEt_3$ (Method 2), (**C**) $PbTe/TiO_2$ mixture after treatment with $LiBHEt_3/Me_3SiCl$ (Method 3), (**F**) $PbTe/TiO_2$ mixture after treatment with $NaOH/NaBH_4$ (Method 4).

The above conclusion was further confirmed by FTIR spectra. As shown in **Figure 2.19**, the strong absorption (**Figure 2.19a**) for the as-prepared $PbTe/TiO_2$ nanocomposites at 1560 cm^{-1} was assigned to the stretching vibration of the carboxylic groups. The two sharp peaks at 2847 and 2923 cm^{-1} were attributed to the symmetric and asymmetric CH_2 stretching vibrations of oleic acid, respectively. After soaking in lithium triethylborohydride/THF (**Figure 2.19b**, Method 2), these bands became much weaker. This revealed that most of oleic acid coordinated to the nanocomposites has been removed. For the samples washed by Method 3 and

4, the organic absorptions have completely disappeared from **Figure 2.19c** and **d**, indicating the total removal of oleic acid, which was consistent with the TGA results.

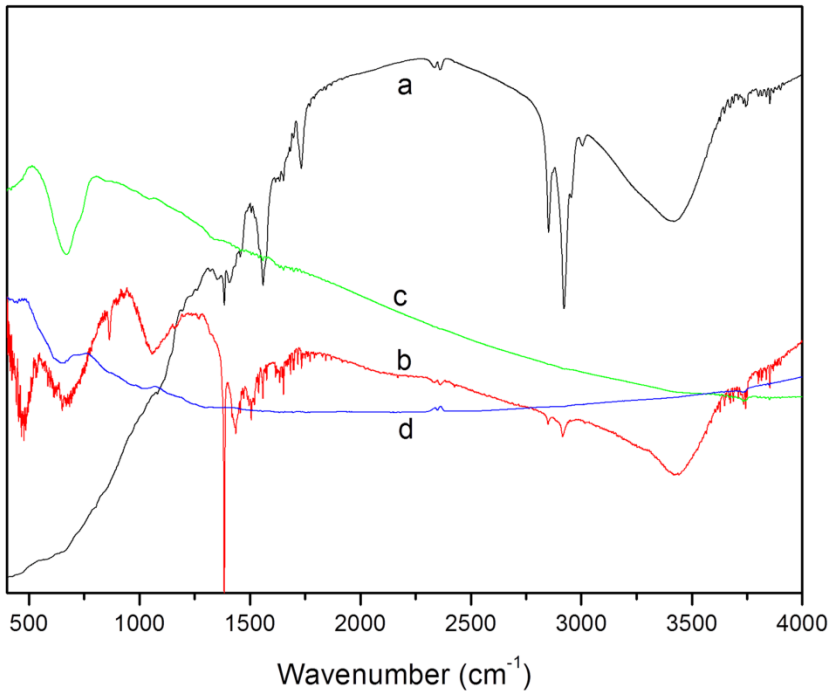

Figure 2.19 FTIR spectra of (**a**) As-prepared PbTe/TiO_2 nanocomposites, (**b**) after treatment with $LiBHEt_3$ (Method 2), (**c**) after treatment with $LiBHEt_3/Me_3SiCl$ (Method 3), (**d**) after treatment with $NaOH/NaBH_4$ (Method 4).

Actually during the sintering, we also observed the improvement that the vacuum did not drop a lot during the heating process for oleic acid-free nanocomposites comparing to a significant outgassing from the samples without OA removal. And Method 3 and 4 gave out much stronger samples after spark plasma sintering process instead of brittle ones.

2.4.3 Reducing Oxidation Layer

In a typical experiment, reducing the oxidation layer was performed during the sintering. After raising the temperature to 500 °C under vacuum (8.0×10^{-2} torr), the chamber was filled

with the forming gas (5% vol. Hydrogen, 95% vol. Nitrogen) for 30 seconds to allow the reduction of the oxide layers. Then the chamber was pumped down to vacuum and filled with the forming gas again. The cycle was repeated for 10 times at the same temperature.

2.4.4 Spark Plasma Sintering

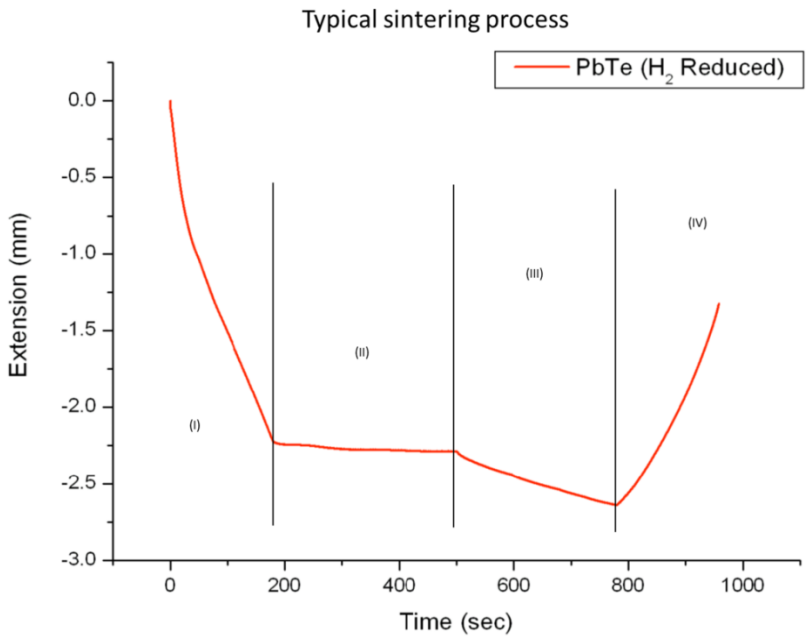

Figure 2.20 Typical Sintering Chart. Extension vs Time.

In a typical process, 5 g of PbTe nanocrystals or PbTe/TiO_2 nanocomposites were loaded into the graphite die after removing the residual organic components and drying under vacuum. The sample was heated to 500 °C to remove moisture and solvents; the forming gas reducing step was applied as described above. Then the load was added on the die with pressure to 30000 N, which refers to the section (I) in **Figure 2.20** and maintained for 5 min (II). Most of the densification process has been completed during this time and then the system (III) was cooled down while maintaining the load. A thermal shrinking was clearly observed from the sintering

curve. After the temperature was close to room temperature, the load (IV) was removed and the volume expansion was observed while reducing the load. Finally the sample was taken out and the graphite layer was carefully polished away. Ideally, a piece of robust, highly condensed, metallic appearance sample should be achieved.

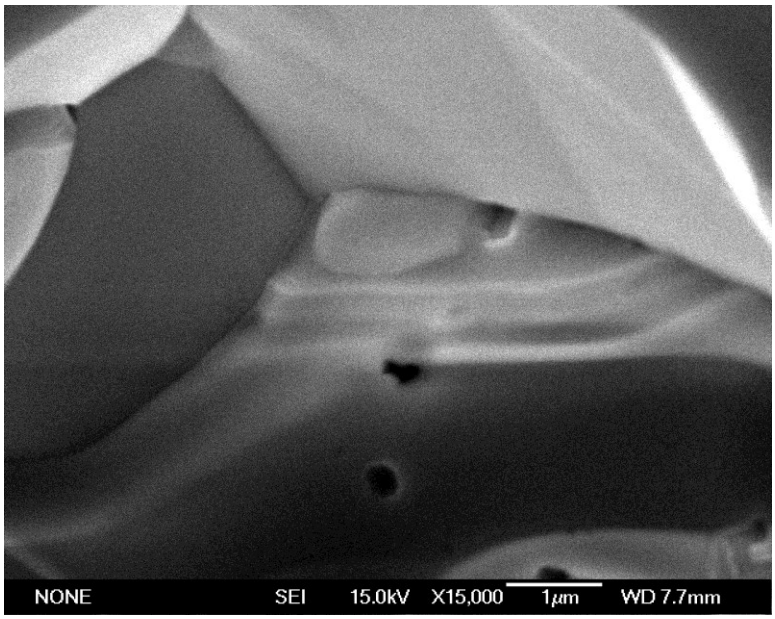

Figure 2.21 SEM image of pure PbTe nanocrystals after sintering.

Finishing all the purification work on the nanocrystals, we finally got the homogeneous mixed, organic ligands free nanocomposites. As described before, the nanostructure must be maintained during the sintering. Actually comparing SEM images of sintered the pure PbTe nanocrystals (**Figure 2.21**) and PbTe/TiO_2 nanocomposites (**Figure 2.22**), we could tell that TiO_2 has played a significant role in preventing the PbTe nanocrystals from fusing together. In **Figure 2.21**, pure PbTe melted and became bulk materials, while in **Figure 2.22** PbTe successfully maintained their nano-size and no significant phase separation occurred between PbTe and TiO_2 nanocrystals. Moreover, some holes in the sintered pure PbTe samples were

found, which indicated some organic residents had stayed there before their decomposition, thus purify the PbTe nanocrystals more carefully and thoroughly was necessary.

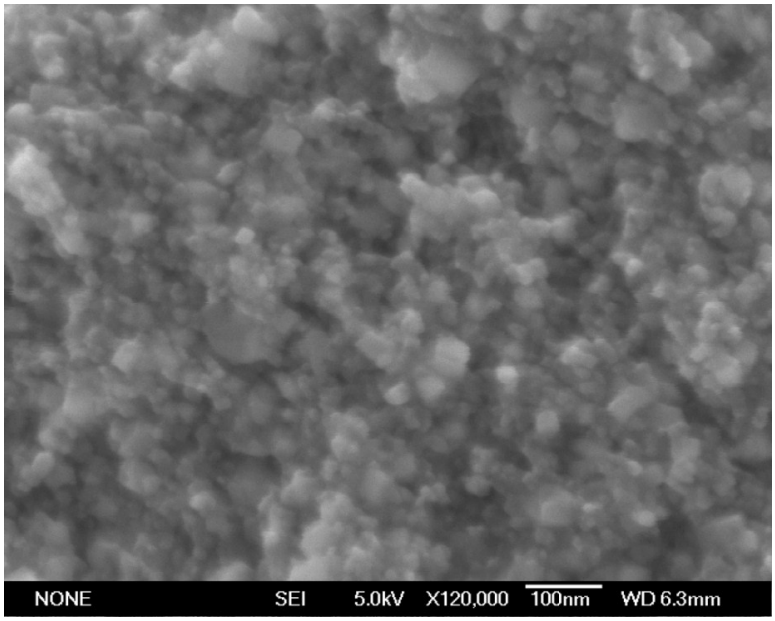

Figure 2.22 SEM image of PbTe/TiO_2 nanocomposites after sintering.

The densities of pellets were measured using *n*-butyl alcohol and the measured results were listed in **Table 2.1**. For the pellets sintered from the PbTe nanocrystals that prepared from aqueous solution synthesis, a completely condensed sample was achieved. The density measured was 8.32 g/cc, which was even higher than the ideal PbTe density (8.16 g/cc). The higher density was possibly due to the presence of metallic Pb (density for metallic Pb and Te is 11.3 g/cc and 6.24 g/cc, respectively) within the nanocomposites. Nevertheless, this experiment did indicate that washing with DI-water and ethanol have completely removed glucose and led to the formation of a completely condensed sample. More interestedly, the density of the pellet with hydrogen reduction was noticed significantly higher than the one without the hydrogen reduction. This result indicated that hydrogen reducing was necessary to remove any oxidation layer on PbTe nanocrystals, which should also lead to an improved electrical conductivity.

Table 2.1 Density measurement of $PbTe/TiO_2$ samples after sintering.

Measurement						
Solvent: n-Butanol, Density 0.81				Component	Purity Density	
$PbTe/TiO_2$=85/15 %Vol.				PbTe	8.164	
Unit: g, cm^3				TiO_2	4.26	
ID*	M1	M2	V	Measured Density	Ideal Density	Percentage
Aq PbTe w/ H_2 (600 °C)	3.8845	3.5067	0.4664	8.3283	8.1640	102.01%
Aq PbTe w/o H_2 (600 °C)	1.6450	1.4787	0.2053	8.0123	8.1640	98.14%
$PbTe/TiO_2$ LiWash w/ H_2 (600 °C)	4.0758	3.5814	0.6104	6.6776	7.5784	88.11%
$PbTe/TiO_2$ Air w/ H_2 (600 °C)	2.5203	2.1632	0.4409	5.7167	7.5784	75.43%
$PbTe/TiO_2$ LiWash w/o H_2 (750 °C)	4.3354	3.8183	0.6384	6.7911	7.5784	89.61%

* M1 is the weight in Air, M2 is the weight in Liquid.
"Aq" means aqueous method synthesized PbTe particles.
"w/ H_2" means Hydrogen reducing was applied at 500 °C during the sintering procedure.
"w/o H_2" means no Hydrogen reducing was applied during the sintering procedure.
"LiWash" means this powder sample was washed by $LiBH_4$ solution for removing the ligands
"Air" means this powder sample was air calcined at 500 °C before sintering for removing the ligands
"(xxx °C)" means final sintering temperature is xxx °C.

$$V = \frac{M1 - M2}{\rho_{fluid}} \qquad \rho_{sample} = \frac{M1}{V}$$

For pellets sintered from $PbTe/TiO_2$ nanocomposites that has been chemically removed oleic acid with Li compound, a relative density of 88% was achieved after sintering at 600 °C; while for the pellets treated by air oxidation and reduction method, a relative density of 75% was achieved. There were two possible reasons for the lower density. One was the oxidation process due to the air treatment. Although hydrogen reduction was employed during the sintering process, it may not be sufficient to remove all the oxidation layers. The other reason could be the formation of aggregated structure during the calcinations process, which hindered their complete densification. For the pellets prepared from the nanocomposites at 750 °C, a slightly higher density was achieved (89.6%). These pellets were robust without any cracking.

To determine the crystallization of PbTe and TiO_2, XRD for these samples were carried out and the crystal grain sizes were calculated by Debye-Scherrer Equation. The XRD patterns were shown in **Figure 2.23**. The black pattern was from PbTe/TiO_2 LiWash w/H_2 (600 °C), the red one was from PbTe/TiO_2 LiWash w/o H_2 (750 °C) while the green one was of PbTe/TiO_2 Air w/H_2 (600 °C).

After calculation, the crystal grain sizes of PbTe were 40 nm, 40 nm and 34 nm respectively to black, red and green patterns in **Figure 2.23.** The crystal grains have grown larger after sintering but still remained in nano-size. Taking density results into account, it was reasonable that larger crystal grain contributes to higher bulk density.

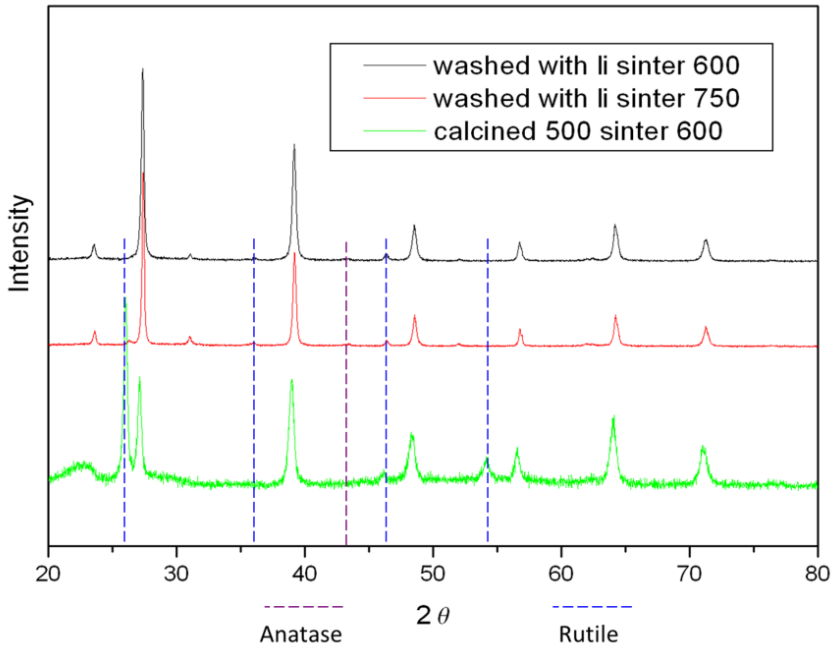

Figure 2.23 XRD results and TiO_2 crystal lattices.

In addition, some TiO_2 peaks appeared after sintering and the two crystal lattices of TiO_2 are marked by color lines. The rutile TiO_2 has lower forming temperature than anatase TiO_2, thus the mixture of two phases was observed in red line, which was sintered at 750 °C. Comparing

these three patterns, we could tell that long time high temperature treating caused highly crystallization of TiO_2. The evidence was the first blue line marked peak in the green pattern, which was contributed by 500 °C air calcination and hydrogen reduction under the same temperature. From Debye-Scherrer Equation, this peak showed a crystal grain of TiO_2 around 34 nm, which was similar with the crystal grain size of PbTe in the same pellet (the green pattern). Larger crystal grain size has higher possibility to cause phase separation. Thus air calcination was not a good pathway for removing organic components in purpose of keeping the homogeneous mixed nanocomposites of PbTe and TiO_2.

However, we found that all the samples were not durable over time, even the most beautiful promising samples. The annealing was carried out at 350 °C for overnight right after the sintering to release the internal stress but did not change the situation very much that the samples still became broken after about 2 week. This issue has remained to be solved till now.

2.5 Thermoelectric Property

This project was cooperated with Toyota Technique Center, USA. Thus only partial data characterized outside of Toyota Technique Center, USA could be released here.

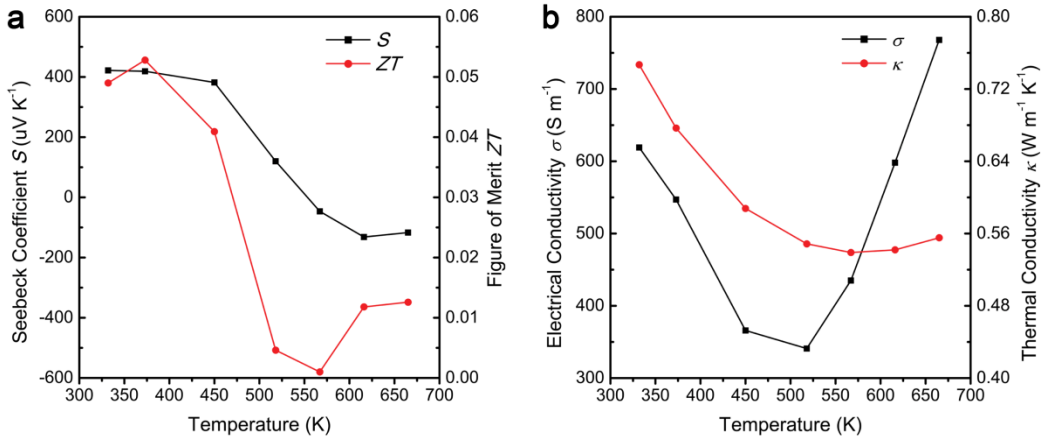

Figure 2.24 Seebeck Coefficient of PbTe/TiO_2 after SPS. (**a black**) is Seebeck coefficient and (**a red**) is figure of merit *ZT*. (**b black**) is electrical conductivity and (**b red**) is thermal conductivity.

As in **Figure 2.24a black**, our PbTe/TiO_2 showed a little bit p-type Seebeck performance. Suggested reason was Te precursor was not able to thoroughly decompose to form PbTe thus Pb exceeded in tiny amount. As temperature increasing, electrical conductivity of PbTe/TiO_2 decreased as typical metal materials, however, after around 520 °C, n-type carrier was activated, so electrical conductivity got recovered as indicated by **Figure 2.24b black**. Moreover, as temperature increased, carrier mobility was reduced by increasing of band gap, which significantly affected thermal conductivity contributed by carrier, as shown in **Figure 2.24b red**. Until over 550 °C, thermal conductivity got slowly recovered by increasing mobility of n-type carriers. Overall *ZT* performance of our samples was far lower than our expectation, as shown in **Figure 2.24a red**, because of poor electrical conductivity, although the thermal conductivity has

been successfully suppressed to 0.53 W m^{-1} K^{-1} by dissimilar nanocomposites as phonon-glass structure.

Our hypothesis by mixing PbTe/TiO_2 nanocrystals to decrease thermal conductivity of bulk device has been proved in a facial, amplifiable method, though it is not as low as reported 0.35 W m^{-1} K^{-1} at 300 K in PbTe superlattice and most low dimension thin films are actually above 0.4 W m^{-1} K^{-1}.[16] Overall, ZT performance of our sample is not high due to poor electrical conductivity, which might due to oxidization layer and ligands residue between nanocrystals, not 100% condensed and its intrinsic un-doped carrier concentration ~10^{18} cm^{-3}. Problem should be able to get solved by doping PbTe, better method in removing ligands, preventing oxidization and optimizing sintering process.

2.6 Conclusion and Future Direction

After comparing several different synthesis pathways, solvothermal synthesis has been proved as most suitable for later mixing with TiO_2 nanocrystals though ligands removal has been a trouble in later SPS process. The synthesis in aqueous solution using NaHTe as precursor has the best yield and nanocrystal networks however lack of ligands made it hard for post-treatment. Reverse micelle assisted synthesis has provided almost perfect mixture of SiO_2/PbTe nanocrystals in aqueous solution however it could only be used as understanding the thermodynamic process because of its extreme low handling ability and expense in amplification. Moreover, electrospray assisted synthesis shows thermodynamically non-equilibrium process, however, if amplified to large amount, reaction rate drops significantly in a single batch thus later formed PbTe could not trap SiO_2 firmly in its nanocrystal network, thus it may not be a uniform mixture, unless changing to flow reactor to maintain the concentration of Pb^{2+}.

In post-treatment, a method to remove oleic acid as ligands has been successfully developed using lithium triethylborohydride and trimethylchlorosilane in tetrahydrofuran (THF). Samples without ligands perform much better during SPS process, otherwise organic compound in high temperature get gasified and has caused graphite die exploded twice. SPS could get high density from nanocrystals however internal stress could cause samples brittle, though this chance could be reduced by post-treatment like annealing.

As-prepared PbTe/TiO_2 nanocomposites have proved our hypothesis that using different nanocrystals as building block for phonon-glass electron-crystal materials. The thermal conductivity has been reduced significantly, gets similar to that of a superlattice structure and almost approaches theoretical calculation results. However, due to oxidation layer and even trace amount of ligands in the interface of nanocrystals, the electrical conductivity and bulk density

could not achieve the best performance thus overall figure of merit are not high enough. Using doping PbTe as electron-crystal portion should be the future direction, meanwhile developing other optimized methods in removing ligands, preventing oxidization during storage and transportation before sintering and optimized sintering process will also be necessary to final success.

Chapter 3 Visible Light Driving Self-Disinfecting Coating

3.1 Background Introduction

3.1.1 Motivation: *In Vitro* Antiviral Disinfecting Coatings

Influenza A viruses, the pathogens that are responsible for the recent H1N1 outbreak and many historical pandemics, remain a threat to the public health.[95-97] On average, the influenza virus caused three deadly pandemics per century since the seventeenth century.[95] Current measures against influenza mainly rely on antiviral drugs and vaccines.[96] Using antiviral drugs might help to reduce the symptoms and contain virus spreading, but their stockpiling is not economical due to unpredictable outbreak of pandemics. While vaccination is considered as the most effective measure to prevent virus infection, continuous evolution of influenza viruses makes the design of effective vaccines extremely difficult prior to an outbreak. Seeking effective solutions that can prevent rapid spreading of the virus is of particular importance.

Influenza viruses are generally spread through contact with contaminated surfaces and virus-containing aerosol.[97] The influenza viruses could survive a remarkable long time on contaminated surfaces, for example over 24 hr on hands, stainless steel and plastics,[98] and spreading through aerosol was supported by other studies, particularly in the case of short distance infection and prolonged airborne period.[99-101] But no matter by which pathway the influenza virus will be transmitted, it is practically impossible to sterilize such public areas with large flowing population every minute using the traditional disinfection techniques. We recognize that visible-light-driving photocatalysts is suitable for self-disinfecting coatings that eligible to disinfecting influenza viruses spontaneously and continuously.

It is unambiguously accepted that the photocatalytic reactivity of photocatalyst comes from singlet oxygen species and reactive free radicals, which are produced by interfacial redox reactions of electrons and holes that are generated upon band gap. Specifically, energy of photons that equal or higher than photocatalyst's band gap is absorbed by photocatalyst to separate electrons and holes, which could travel to the surface of photocatalyst and get trapped there (e_{tr}^-, h_{tr}^-). Then by reacting with acceptor and donor, reactive species, such as $H^\bullet$, $O_2^{\bullet-}$, $OH^\bullet$, $CO^{2\bullet-}$, $R^\bullet$, $^1O_2$, etc, will be generated and may vary depend on the surrounding solution environment.[102] While the other way to terminate e_{tr}^- and h_{tr}^- is recombination and releases the energy as heat. These reactive species are highly reactive and their reactions with free amino acid and amino acid residues, which significantly change the function of the entire proteins, are widely investigated.[103-106] Rapid chemical reaction of His, Trp, Tyr, Met and Cys residues with singlet oxygen species at physiological pH has been reported and at higher pH even Arg and Lys residues would undergo photo oxidation.[107-110] Simultaneously, reactions between free radicals and free amino acids or amino acid residues have been summarized as hydroxylation, chlorination and nitration of aromatic amino acid residues,[111-122] hydroxylation of aliphatic amino acid side chains,[111] nitrosylation of thiol groups,[123-126] sulfoxidation of methionine residues,[121,127-128] chlorination of primary amino groups,[122,129-134] and conversion of some amino acid residues to carbonyl derivatives.[135-139] Furthermore, oxidation can also cleave the polypeptide chain and form cross-linked protein aggregates.[105,135,140] These reactions will destroy function of these proteins and eventually disinfect the bacteria. In addition, oxidization damage to genetic materials will also happen to increase the disinfecting process.[141-142]

3.1.2 Research Objective

Herein, we proposed the fabrication of self-disinfecting surfaces on which influenza virus and other hazard pathogens could be, spontaneously and continuously, disinfected by visible light. This was achieved by forming semiconductor coatings that could absorb visible light and produce active oxidative species. As illustrated in **Figure 3.1**, when fomites and virus containing aerosols get contacted the surface as schemed, as-produced reactive species could oxidize their amino acid residues on the envelope proteins of the virus, which inactive these proteins and disinfect the virus.

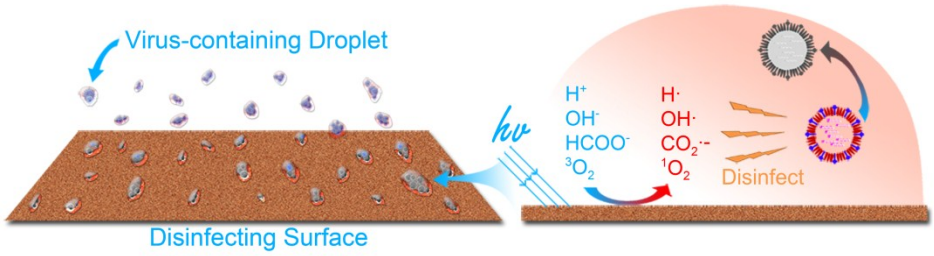

Figure 3.1 Illustration of disinfecting virus on a self-disinfecting surface powered by visible light.

Our self-disinfecting surfaces were fabricated from nano-crystals (NCs) of $CuInZn_4S_6$ (CIZS) with band gaps within the visible light. The NCs were synthesized from diethyldithiocarbamate precursors of zinc, copper and indium with a designed molar ratio of 4:1:1. The synthesis was achieved by the hot-injection method using oleic acid as the capping agent. It was also worth mentioning that the fabrication of such coatings is achieved by directly coating photoactive nanocrystals on the substrates followed by a sintering process. Such a simple wet chemical approach ensured effective fabrication of such disinfecting surface at lower cost comparing to ion-injection doping, CVD process, plasma itching, electron sparking and other high temperature sintering processes.

3.2 Experimental Procedure

3.2.1 Synthesis of $CuInZn_4S_6$ nanocrystal

In a typical synthesis, 0.8 mmol of zinc diethyldithiocarbamate, 0.2 mmol of copper diethyldithiocarbamate, 0.2 mmol of indium diethyldithiocarbamate and 2 mL of oleic acid were mixed in 10 mL 1-Octadecene in a 50 mL three neck flask under nitrogen flow and vigorous stirring. The flask was heated slowly to 180 °C and 1 mL of oleylamine was added after the solid was completely dissolved. After 2 min, the flask was cooled rapidly by adding ethanol to room temperature. The product was washed by toluene and methanol twice and finally stored in 5 mL toluene. After the final wash, samples were blocked from light by wrapping the container with aluminum foil. The final concentration was determined by weighting the residual solid after evaporate certain volume of CIZS solution.

3.2.2 Design Self-Disinfecting Coating

Designed amount of CIZS toluene solution was drop-coated onto glass cover slips (Ted Pella, Inc.) with a surface concentration of 5 $\mu g/mm^2$. The coatings were dried under the room temperature without light illumination and followed by the surface ligands exchange with cysteamine. In a typical process, glass cover slips with dried $CuInZn_4S_6$ nanocrystal coating were placed in to 24 well plates then 500 μL of cysteamine (5 mg/mL) water solution were added to each well. After 30 min, solution was sucked out and every samples was rinsed by 1 mL of DI-water twice to remove the exceed cysteamine. Finally samples were dried under the room temperature in a covered box to prevent the light.

For ligands exempt samples, as-coated cover slips were placed in a glass container and nitrogen carried water vapor was supplied. The samples were sintered at 400 °C for 4 hr while heating rate was 5 °C /min and cooled slowly to room temperature.

TiO_2-coated surfaces were prepared for control at the same surface concentration using commercial TiO_2 (P25, Degussa) suspended in H_2O (10 mg/mL) as the coating solution.

3.2.3 Disinfection of H1N1 Influenza A Virus

Disinfection effects were examined by immersing the coated slips with 300 μL solution of A/PR/8/34 H1N1 influenza A virus (PR8) on ice, which titer was 3.57×10^4 $TCID_{50}$/mL (50% Tissue Culture Infectious Dose per mL) on MDCK (Madin-Darby canine kidney) cell line as determined by Reed-Muench method, meanwhile bare slips, TiO_2 coated slips and dark controls were set up in the same configuration. Visible light illumination was applied by a solar light simulator (Solar Cell & Module Test Equipment, PV Measurements, INC.) equipped with a ultraviolent (UV) filter (HOYA HMC 58 mm UV(0)). After 1 hr illumination, virus activities were measured using the same $TCID_{50}$ assay on MDCK cell line. To simulate the virus spreading through aerosol, droplets of virus solution (15 μL) were deposited on the 5 $\mu g/mm^2$ CIZS coated slips, which were then placed on ice. Virus activities were assayed after only 15 min using the same Reed-Muench method.

3.2.4 Disinfection of HCV

CIZS-coated slides were immersed in 400 μL HCV solution with a titer of 4,900 ffu/mL (foci forming unit per mL) under illumination for 1 hour on ice bath. Then HCV virus was titrated by immunofluorescence assay. Briefly, Huh-7.5.1 cells were seeded in 96-well plate at

the density of 3×10^3 cells/well. HCV supernatant collected after the CIZS treatment was 10-fold serially diluted in complete Huh-7.5.1 cell growth medium and inoculated onto Huh-7.5.1 cells in triplicate for 72 hr at 37 °C. Infected cells then were fixed with methanol and detected by immunohistochemical staining for HCV protein NS5A. By counting the number of the NS5A antigen positive foci at the highest dilution, the virus titer was assessed and presented as ffu/mL.

3.2.5 Disinfection of *E. coli.*

Briefly, 35 μL of *E. coli.* with titer of 2×10^5 cfu/mL (colony formation units per mL) was added onto each CIZS coated surface and illuminated for 1 hr. Then the *E. coli.* were plated out on agar to measure the remaining titer after incubate 18 hr at 37 °C .

3.2.6 Deactivation of Hemagglutinin (HA)

Washed pooled chicken red blood cells (10% in Alsever's solution, Lampire Biological Laboratories) were diluted to 1% using PBS buffer solution. After 2 hr treatment by 20 $\mu g/mm^2$ of CIZS coated slips, 100 μL PR8 solution, which titer was 3.57×10^7 $TCID_{50}$/mL on MDCK cell line, was added into the first column of a Corning V-bottom 96-well plate, which was 2-fold serially diluted across the 96 well plate with PBS. The final 50 μL from each well of the last column was disposed. Then 50 μL freshly PBS-diluted chicken red blood cells (1%) was added to each well and mixed by gently tapping the plate. The plate was incubated for 30 min at 4 °C and HA Unit was observed directly from end point of agglutination phenomena.

3.2.7 Deactivation of Neuraminidase (NA)

Neuraminidase (NA) assays were carried out in a 48-well plate. CIZS-coated slips were immersed in 250 μL neuraminidase solution (10 UN/mL, Type V, Clostridium perfringens) on ice and illuminated for 1 hr. Then 200 μL solution was taken out and mixed with 80 μL of 5 mM 2'-(4-Methylumbelliferyl)-α-D-N-acetylneuraminic acid sodium salt hydrate aqueous solution, 550 μL of 100 mM sodium acetate buffer with 2 mM calcium chloride (pH 5.0), and incubated at 37 °C with vigorous stirring. After 30 min, 170 μL of 200 mM glycine buffer (pH 10.7) was added and the fluorescence signal from 400 to 500 nm was collected using a QuantaMaster Spectrofluorometer (Photon Technology International) with an exciting wavelength of 365 nm. The emission intensity at 450 nm was selected to compare the activity of neuraminidase.

3.2.8 Deactivation of Trypsin

First of all, CIZS nanocrystals were prepared to be sustainable in aqueous solution by ligands exchange. Typically, 1 g of cysteamine was dispersed in 5 mL water and 1 mL ethanol, then 200 μL as-prepared CIZS solution was added and vigorous stir was applied. The vial was covered by aluminum foil to prevent illumination. After 12 hours, the solution was mixed with 20 mL ethanol, centrifuged and the solid was re-dispersed in 4 mL of water. Typical zeta potential was around 40 mV and the yield was about 90%.

For trypsin inactivation, 2 mg of trypsin, 0.4 mg of CIZS and 2 mL of 50 mM pH 8 tris buffer were mixed and stirred vigorously on ice bath. 30 μL of sample solution was taken out every hour and diluted to 195 μL using the same buffer. After adding 5 μL of 50 mM N-benzoyl-DL-arginine 4-nitroanilide dimethyl sulfoxide solution, adsorption at wavelength 410 nm was selected to quantify the degradation kinetics.

3.3 Results and Discussion

3.3.1 Characterization of As-prepared $CuInZn_4S_6$ Nanocrystals Coating

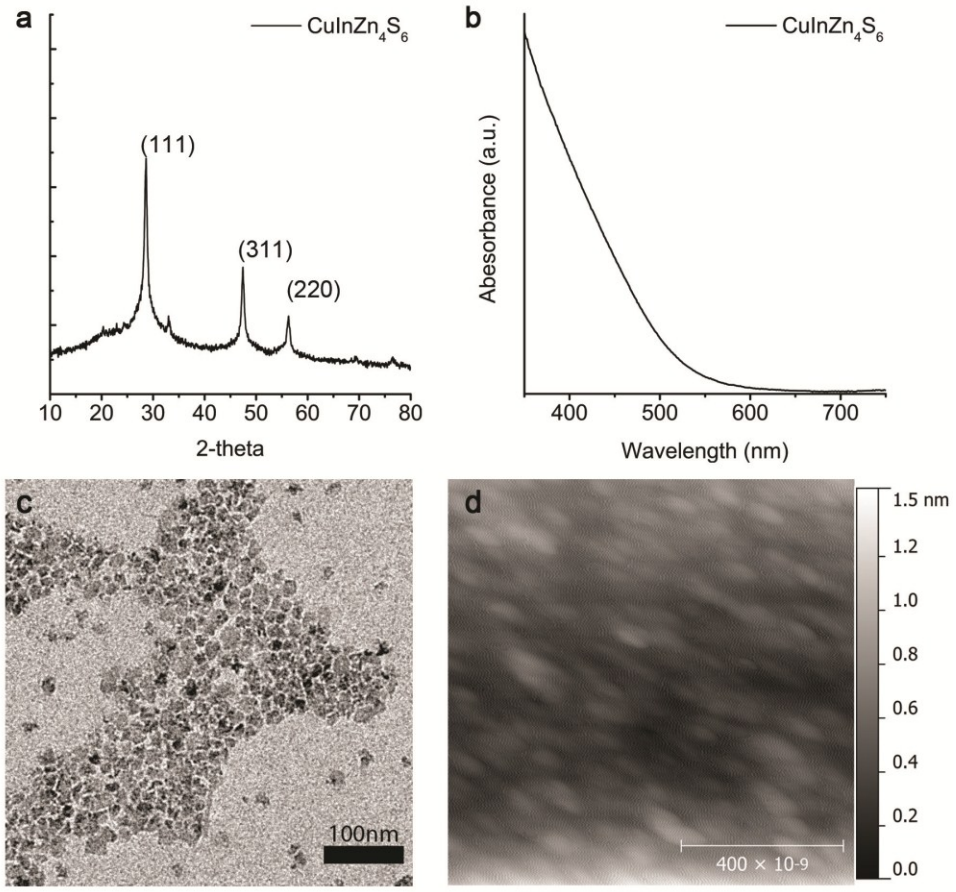

Figure 3.2 (**a**) XRD pattern of as-prepared $CuInZn_4S_6$ nanocrystals, which suggested ~20 nm crystal size calculated from Debye-Scherrer Equation. (**b**) Absorption spectrum of as-prepared $CuInZn_4S_6$ nanocrystals. (**c**) TEM image shows a particle size around 20 nm by direct observation. (**d**) AFM image of the coating surface suggest the formation of uniformed self-disinfecting coatings.

The $CuInZn_4S_6$ nanocrystals (NCs) were synthesized from diethyldithiocarbamate precursors of zinc, copper and indium with a designed molar ratio of 4:1:1. The synthesis was achieved by the hot-injection method using oleic acid as the capping agent. As-synthesized NCs were then coated on glass substrates to form the uniform CIZS coatings. As-synthesized NCs

showed a zincblende structure (see the x-ray diffraction (XRD) pattern in **Figure 3.2a**) with intense absorbance in the visible-light range (**Figure 3.2b**) with a band gap estimated around 2.21 eV, which was consistent with those reported from other studies.[143] Trans-mission electron microscopic (TEM) image of the NCs suggested a uniformed NC size centered at 20 nm (**Figure 3.2c**), which was consistent with that estimated from the XRD pat-tern using the Debye-Scherrer Equation. Using the NCs as the building blocks led to the formation of uniformed self-disinfecting coatings. **Figure 3.2d** showed a representative atomic force image (AFM) of a coating surface with smooth morphology. Compared with the traditional deposition approach (e.g., chemical vapor deposition or physical vapor deposition), this strategy provided a simple approach towards the synthesis of self-disinfecting surface from pre-made NCs.

3.3.2 Effect of Surface Ligands Exchange

Ligands exchange happened at the interface between nanocrystal coating and ligands solution. As time prolonged, the ligands would diffuse layer by layer into the coating and occupied position the originally belonged to oleic acid. As cysteamine was hydrophilic molecule, the $CuInZn_4S_6$ nanocrystals gaining more and more cysteamine instead of oleic acid would eventually became water soluble and been washed away by DI-H_2O, as illustrated in **Figure 3.3a**. However, lack of cysteamine but rich in oleic acid would form a hydrophobic barrier between $CuInZn_4S_6$ functional coating and influenza virus tiny droplets. To figure out how it affecting the disinfecting performance of $CuInZn_4S_6$ coatings, the concentration, volume of cysteamine aqueous solution, the surface concentration of $CuInZn_4S_6$ nanocrystal coatings were fixed but ligands exchanging time was varied like 0, 0.5, 1 and 2 hr. Utilizing the same setup in Section

3.2.2, remaining virus infectivity was examined by the same Reed-Muench method and marked as 50% Tissue Culture Infectious Dose per mL.

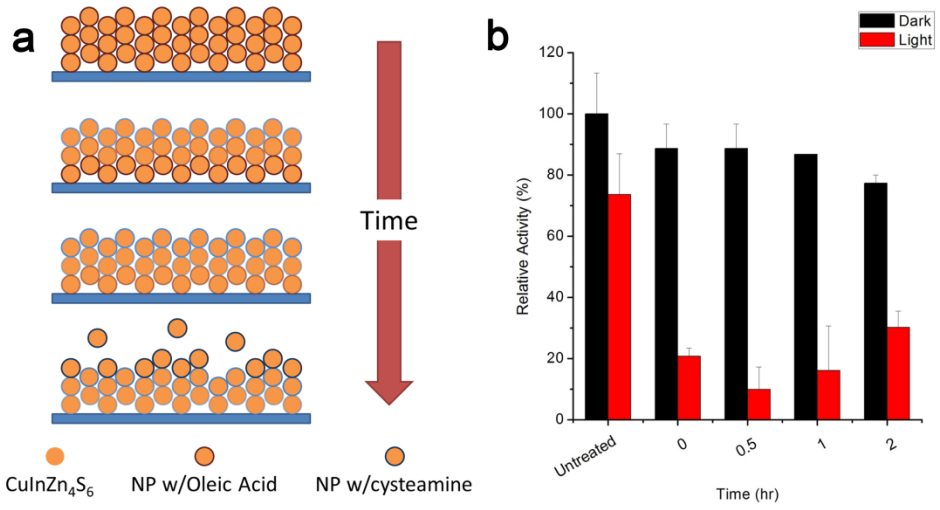

Figure 3.3 (**a**) Illustration of surface ligands exchange process that $CuInZn_4S_6$ nanocrystals get more hydrophilic as time goes on then eventually get lost during washing. (**b**) Different time of surface ligands exchange will affect the overall disinfecting performance of the coating.

The results were plotted in **Figure 3.3b** as relative activity of virus. Clear difference in remaining infectivity was observed from different ligands exchanging time. That no exchanging (0 hr), the reactive species generated by $CuInZn_4S_6$ nanocrystals could not contact with virus in the best situation and disinfecting them while 0.5 hr exchanging gave these reactive species better chance. However, for time longer than 0.5 hr, $CuInZn_4S_6$ nanocrystals coatings began to get loss during washing process, thus overall performance has been destroyed which agreed with our preliminary results with different surface concentrations of $CuInZn_4S_6$ nanocrystals which was not displayed here. However, due to too much manipulating steps, accurate amount of loss in $CuInZn_4S_6$ nanocrystals was not able to be figured out and amount of cysteamine on sites of $CuInZn_4S_6$ nanocrystals was not successfully characterized because of light absorption of

$CuInZn_4S_6$ nanocrystals and potential photo-oxidizing of thiol group on cysteamine which resulting loss of ligands.

Overall our surface ligands exchanging model has been confirmed and finally we chose the exchanging condition as described in Section 3.2.2.

3.3.3 Disinfection of Influenza A Virus

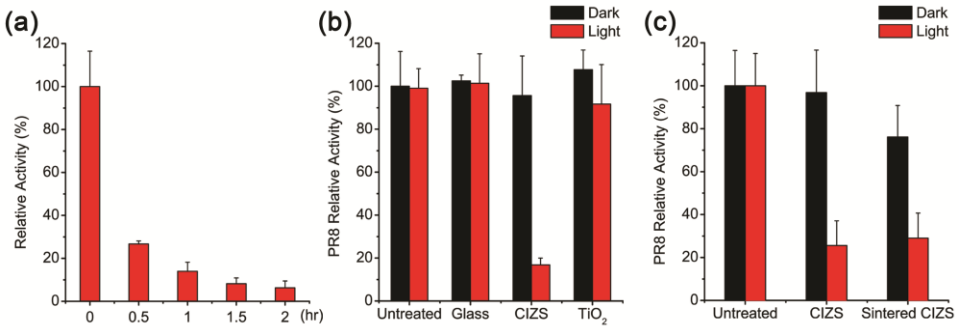

Figure 3.4 Disinfection of influenza A virus. (**a**) Disinfection efficiency of CIZS-coated surfaces over time. (**b**) Disinfection efficiency of CIZS- and P25-coated surfaces with and without illumination for 1 hr. (**c**) Disinfection efficiency of the CIZS-coated surfaces prepared with and without the sintering process.

The disinfecting ability of these coatings was examined using A/PR/8/34 H1N1 influenza A virus (PR8) as an example. **Figure 3.4a** showed the activity of the virus after exposure to the CIZS coated surfaces and visible light illuminated for 0.5, 1, 1.5 and 2 hr, exhibiting remarkable infectivity loss of 73%, 86%, and 92% and 94%, respectively. To confirm the disinfection effect, **Figure 3.4b** compared the virus infectivity after exposure to glass, 5 $\mu g/mm^2$ CIZS coated and same concentrated TiO_2 (commercialized P25), a widely used photo oxidizing catalyst, coated surfaces for 1 hr. With visible light illumination, the TiO_2-coated surface disinfected only 8% of the virus, which was significantly less effective than CIZS-coated surface (83%), while the glass surface showed no effect. Without visible light illumination, no significant change in infectivity

was observed. This result clearly demonstrated the effectiveness of using visible-light-adsorptive semiconductors as self-disinfecting surface. The significantly lower disinfecting capability observed for the TiO_2 surface was due to the higher band gap of TiO_2 (2.21 eV[143] for $CuInZn_4S_6$ and 3.1 eV for TiO_2) that excludes it from harvesting visible light.

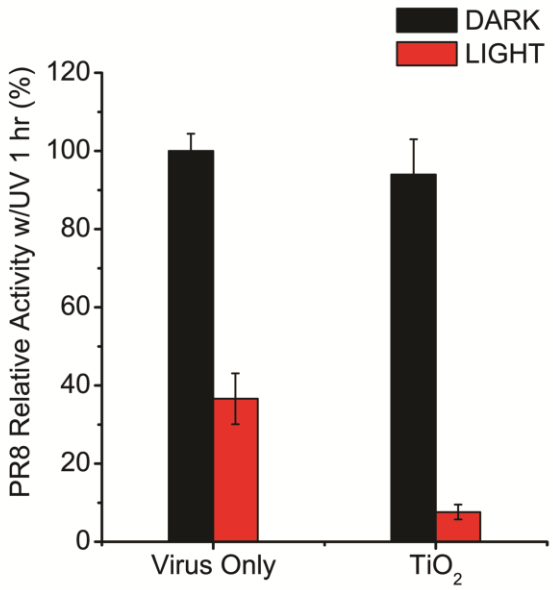

Figure 3.5 Disinfection efficiency of P25-coated surfaces with and without illumination for 1 hr. UV lights were not blocked, thus TiO_2 just contribute 29% of total disinfection on PR8.

To simulate actual circumstances where small volumes of virus-containing aerosols or liquid were deposited on a surface through coughing, sneezing or direct contact, droplets of PR8 virus solution (~15 μL) were applied on the CIZS surface and the results were summarized in **Figure 3.4c**. 74% of virus infectivity was neutralized shortly after only 15 min, suggesting a highly effective and rapid route to disinfect influenza virus using visible light. However, we were aware that the un-sintered CIZS-coated surfaces might not be stable enough for practical uses. Mechanically stronger CIZS coatings were therefore prepared by sintering the nanocrystal coatings at 400 °C under nitrogen and water vapor; removal of the capping ligands from the

nanocrystals and sintering process converted the nanocrystals into highly robust CIZS coatings. As expected, such robust coatings could disinfect 71% of the virus within exposure time of 15 min. Considering abundant semiconductor materials that are photoactive within the visible light wavelength, this study opened a new avenue to the design and fabrication of self-disinfecting coatings.

Disinfecting efficiency of P25 coated glass substrates under UV lights has been tested as additional control experiment. Glass substrates were drop coated by P25 TiO_2 nanocrystals with the surface concentration of 5 $\mu g/mm^2$ and dried under room temperature. Then 300 μL of A/PR/8/34 H1N1 influenza virus (PR8) with the original titer of 6.81×10^5 $TCID_{50}$/mL (50% Tissue Culture Infectious Dose per mL) was added onto the slides and exposed to the light source with same light intensity as previous experiments for 1 hr without UV filter applied for the light group while dark group was wrapped by aluminum foil. The remaining infectivity of PR8 was plotted in **Figure 3.5**. As UV lights were not blocked, the virus only group in light condition already lost 63% of their infectivity due to UV lights irradiation, while the TiO_2 treated group lost total 92% of their infectivity. By deducting the donation from directly exposing to UV lights, here we could make the conclusion that P25 TiO_2 could disinfect only 29% of PR8's infectivity.

3.3.4 Disinfection of HCV and *E. coli.*

The general applicability of such disinfecting surface was further examined using hepatitis C virus (HCV). Like influenza virus, HCV is an enveloped virus but currently has no vaccines available. As shown in **Figure 3.6a**, HCV infectivity was reduced by 85%, while no significant changes observed for without light exposure and bare glass treated group.

Immunofluorescence analysis of HCV samples using the antibody against the viral core protein was carried out and the representative images were shown in **Figure 3.6c-e**. Compared to untreated HCV (**Figure 3.6c**), the fluorescence-positive cells (infected by HCV) were greatly reduced (**Figure 3.6d**) when HCV was treated with as-fabricated self-disinfected surface for 1 hr of illumination. Under dark condition, surface treatment has no effects (**Figure 3.6e**). As-fabricated CIZS surfaces also demonstrated its disinfecting effects on bacteria, another diverse microbe group that is highly related to human health. A common bacterium, *E. coli.* was used in this study. As shown in **Figure 3.6b**, only 21% of *E. coli.* retained their activity while no significant change was observed in control groups.

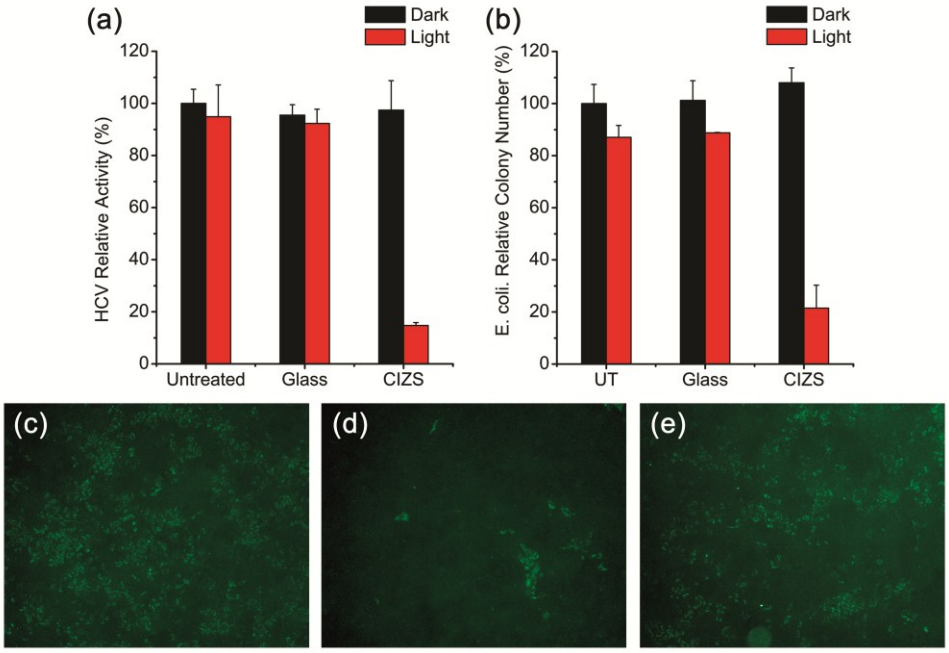

Figure 3.6 Disinfection of hepatitis C virus and bacteria. (**a**) Disinfection of HCV and (**b**) *E. coli.* by CIZS-coated surface after 1-hr illumination and fluorescence images of the HCV-infected cells on the CIZS-coated surface: (**c**) control, (**d**) with and (**e**) without the illumination.

3.3.5 Disinfection Mechanism

We suggested that the disinfection mechanisms may involve inactivation of hemagglutinin (HA) and neuraminidase (NA), the two critical envelope proteins governing influenza virus infection. HA receptor-binding domain mediates the entry of flu virus into host cell, while NA effectively cleaves the glycosidic linkages of neuraminic acid and allows virion be released from the host cells. HA is named by its ability to aggregate red blood cells and this hemagglutination ability is also used to quantify influenza viruses. To examine the disinfecting effects from CIZS, quantification of PR8 viruses were carried out by hemagglutination activity assay and HA units (HAU) were determined.

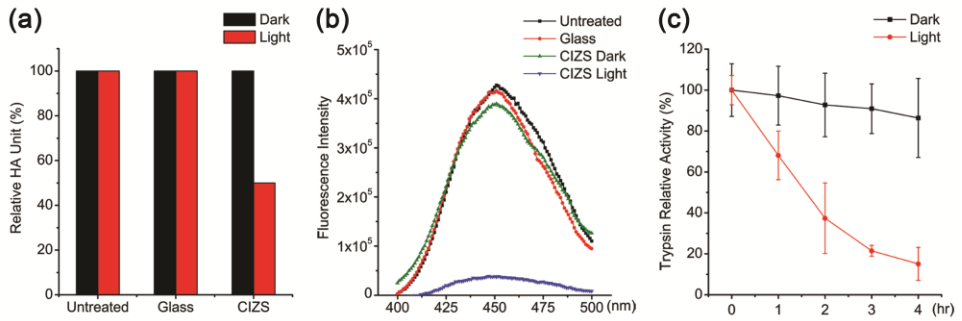

Figure 3.7. Inactivation of proteins: hemagglutinin (**a**) and neuraminidase (**b**) on CIZS-coated surface and bare glass surface with and without illumination for 2 hr. and trypsin (**c**) by CIZS nanocrystals with and without illumination.

As shown in **Figure 3.7a**, HAU of PR8 dropped by 50% after 2 hr exposure to visible light on the CIZS-coated surface comparing to the same treatment under darkness, while no difference was observed between light and dark condition on native or bare glass treated PR8. The result indicated that hemagglutination ability of PR8 was impaired by the CIZS coated surfaces, most likely due to adverse effects on HA. We also examined whether NA is affected by the CIZS surface. The enzymatic activity of NA was measured using 2'-(4-Methylumbelliferyl)-

α-D-N-acetylneuraminic acid sodium salt hydrate as the substrate, which upon cleavage by NA would generate products emitting fluorescence at 450 nm when excited at 365 nm. After exposure to the visible light on different surfaces for 1 hr, NA activity was measured and the spectra were plotted in **Figure 3.7b** (experiment details please refer to supplementary information). The result showed that CIZS treated NA lost 90% activity, comparing to native NA and bare glass treated NA with illumination and CIZS treated under darkness.

We believe that the inactivation of HA and NA is attributed to oxidative species (e.g., singlet oxygen species and reactive free radicals) produced upon illuminating the CIZS, such as $^1O_2$, H•, O_2•-, OH•, and CO_2•-.[102,104,106] These species were known to be capable of reacting with amino acid residues, such as His, Trp, Tyr, Met, Cys and Arg, and altering protein properties.[103,105,107,110] Furthermore, the oxidation can also cleave a polypeptide chain and induces formation of crosslinked protein aggregates.[135,140] Specific to H1N1 influenza virus, the H1 binding site contains Asp, His, Leu, Trp, Tyr, Thr, Gly and Gln, while the N1 active cite contains Glu, Asp, Val, Arg, Gln, and Tyr.[144-145] Such residues can react with the oxidative species, leading to the disinfection effect observed. Moreover, it is also possible that these reactive species penetrate viral particles and cause damages to genetic materials, resulting in the loss of infectivity.[142,146]

For the other instance, Hepatitis C virus, which shares a similar virion organization with influenza virus, has an envelope decorated with viral glycoproteins, E1 and E2, which are important for viral infectivity. Thus, it was thought that HCV might be neutralized by CIZS-coated surface through singlet oxygen species and free radicals reacting with residues of E1 and E2, such as His, Trp, Tyr, Met, Cys, Arg, Lys, Gln, Leu and Val etc. [147]

Based on the proposed mechanism, such an inactivation process should be applicable to any proteins. We then tested the hypothesis on trypsin. Indeed, trypsin's activity dropped significantly with visible light exposure to 68%, 37%, 21% and 15% after 1, 2, 3 and 4 hr treatment, respectively (**Figure 3.7c**). Experiment details please refer to supplementary information. The active site of trypsin contains Ser, Asp and His,[148] among which His could be reacted with singlet oxygen species thus to inactivate trypsin. This result supports our hypothesis that the protein inactivation via photo oxidation is non-selective and can be generally applied to proteins in addition to HA, NA and trypsin.

These results of mechanism suggest an essential conclusion: it is possible to construct general self-disinfecting surfaces powered by visible light for virus and pathogens from photoactive coatings.

3.4 Conclusion and Future Direction

Overall, we have demonstrated the fabrication of highly effective self-disinfecting surface from preformed NCs. Such surfaces show promising ability in non-discriminative disinfection of influenza A virus, HCV and *E. coli.*. Several important features, including use of visible but not hazardous UV light, non-selective inactivation of proteins, and capability of continuous disinfection, render such surfaces a practical and effective solution to reduce potential harmful infections of pathogens in public area.

In the future, $CuInZn_4S_6$ based visible light powered coatings need improve its mechanical strength and figure out its toxicity to human being, though it is suggested as lower toxicity in elements than Cd or Pb.

Chapter 4 Spontaneous and Continuous Disinfection of Influenza A Virus by Non-stoichiometric Perovskite-structured La_xMnO_3

4.1 Background Introduction

4.1.1 Motivation: External Condition Independent Self-disinfecting Coating

As introduced in Chapter 3, influenza A virus has been a continuous threat to people's health security for hundreds of years. Extensive research interests have been addressed into preventing the irregular outbreak and controlling the rapid spreading of flu pandemic. As a result, antiviral drugs and vaccines has been considered as the most effective *in vivo* measures,[96] and cutting off the spreading pathway of influenza virus, which were reported as contacting contaminated surfaces and virus-containing aerosol, has become important *in vitro* solution.[97,149]

Massive reports have been published focusing on self-disinfecting surfaces and nearly all of them were utilizing photocatalysts to kill microbes, in which bacteria received more research interests than virus did. Typically, reactive free radicals that generated during light illuminating are utilized as mediators to disinfect microbes and visible light are preferred by scientists because of UV band's carcinogenic potential, such like N-doped TiO_2, AgBr-Ag-Bi_2WO_6 nanojuction and our previous reported $CuInS_4Zn_6$. However, it is Achilles' Heel that performance of all these photocatalysts are limited by light resource, switching on or off, high or low intensity, band distribution, etc. To overcome this inherent drawback of photocatalysts based self-disinfecting surfaces, herein we propose an alternative solution that can spontaneously disinfect virus even in dark condition, working continuously and silently, maybe not as strenuous

as photocatalyst under a high power light source but get the disinfection done rapidly with no attention attracted.

The materials of as suggested coating could use the same mechanism as $CuInZn_4S_6$ coating that react with envelope proteins, which usually should be oxidization, but not requiring external conditions. The oxidize ability should be proper that not hazard to human been but enough for microbes' proteins. Moreover, the material should be stable in crystal structure even doing their oxidization jobs, unlike MnO_2 that physical morphology of MnO_2 will crash because of changing valence of Mn, where promising oxidize ability comes from.

Herein, we located this problem with the new application potential of $LaMnO_3$ compounds in disinfecting influenza virus, spontaneously, continuously and external conditions freely, which means no special setup is necessary to make it work, especially illumination or temperature. Comparing to other oxidative chemicals currently using in disinfection like Cl_2, HClO, $KMnO_4$, etc., $LaMnO_3$ is less harsh and superior in stability for long-term operation and it doesn't need to be cleaned after applied. To the best of our knowledge, this is the first report about disinfecting ability of perovskite-structured compounds.

The family of $LaMnO_3$ compounds is some of the most interesting members of the perovskite oxide family. The research attention to them has been attracted as compound with colossal magnetoresistance,[150-151] the cathode material for the solid oxide fuel cells,[152] and the oxidation catalyst,[153-154] since sixty years ago. It is well known that $LaMnO_3$ exhibits promisingly higher oxidative ability comparing to most other perovskite oxides.[155-156] Structural investigations of $LaMnO_3$ have revealed that Mn^{4+} ions are created in $LaMnO_3$ by the presence of vacancies in La and Mn sites.[157-158] For further improving the oxidative ability of $LaMnO_3$,

the partial substitution of La by other elements and non-stoichiometry of La/Mn ratio have been extensively studied to increase the Mn^{4+} ions amount by many researchers.[159-160]

4.1.2 Research Objective

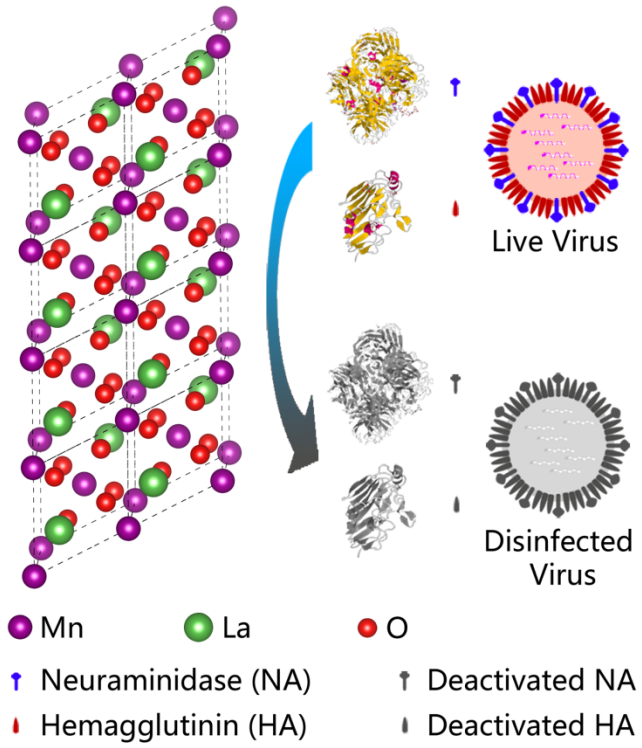

Figure 4.1 Oxidization thus disinfection of influenza A virus by non-stoichiometric perovskite-structured La_xMnO_3 (x=1, 0.95, 0.9).

External condition independent self-disinfecting coatings are proposed based on perovskite-structured $LaMnO_3$ to work in the dark condition. As illustrated in **Figure 4.1**, the oxidative ability of $LaMnO_3$ compounds can be utilized to oxidize the amino acid residues of envelope proteins on influenza viruses, hemagglutinin (HA) and neuraminidase (NA), and eventually disinfect them. Taken H1N1 as an instance, previous research showed that His, Trp and Tyr were included in HA's activate site while Arg and Tyr were in NA's,[144-145] which

residues could easily react with oxidative species and resulted in the deactivation of entire proteins. Moreover, the oxidative ability of $LaMnO_3$ compounds would be also triggered by non-stoichiometric way to improve its disinfecting ability as La_xMnO_3 (x=1, 0.95, 0.9).

4.2 Experimental Procedure

4.2.1 Preparation of Non-stoichiometric Perovskite-structured La_xMnO_3 (x=1, 0.95, 0.9)

Non-stoichiometric La_xMnO_3 (x=1, 0.95, 0.9) materials were prepared by the citrate sol-gel method from $La(NO_3)_3 \cdot 6H_2O$ (Aldrich, 99.99%), $Mn(NO_3)_2 \cdot 4H_2O$ (Aldrich, ≥97.0%) and citric acid (Aldrich, 99.5%). The solutions were prepared in de-ionized water with cation ratio La:Mn of 1:1, 0.95:1 and 0.9:1, respectively. Then, the citric acid was added with 10 wt.-% excess over the stoichiometric quantity to insure the complete complexation of the metal ions. Hereafter, the solution was stirred and condensed on a heating stirrer (80 °C) until a viscous gel was obtained. Then the gel was placed in a vacuum oven (90 °C, 12 hr) to form spongy materials after removing the nitrous vapors. Finally the raw material was crushed and calcined in pure oxygen (700 °C , 5 hr, 10 °C /min) and ball-milled (6 min) for further characterizing.

4.2.2 X-ray Diffraction (XRD) Patterns

The XRD patterns were obtained with an X'Pert Pro X-ray powder diffractometer operating at 45 kV and 40 mA equipped with nickel-filtered Cu Kα radiation (λ = 1.5418 Å), ranging from 20° to 70° with a 0.02 step size.

4.2.3 Electron Paramagnetic Resonance (EPR) Spectra

The EPR spectra were recorded at room temperature (RT) with a Bruker A320 spectrometer in the X band frequency (≈9.78 GHz). Portions of same weight of samples (20 mg) were placed inside the quartz probe cell. Location and the intensity of g factors were determined by Bruker's WINEPR program based on the $h\upsilon = g\beta H$, where h is Planck constant, H is the applied magnetic field, β is Bohr magneton.

4.2.4 Temperature Programmed Reduction (TPR)

The TPR measurements were performed in a conventional, U-shaped, quartz microreactor. The samples (50 mg) were first heated to 500 °C under a flow of 30 ml/min pure O_2 and kept for 30 min. Then, the samples were cooled down to RT in 30 ml/min pure O_2 flow and followed by purging with Helium for 30 min. After that, the samples were heated up at a ramping rate of 10 °C / min from 50 to 800 °C under a flow of 5% H_2/He (30 mL/ min). The concentration of H2 in the outlet gas was measured by a Balzers QMS200 quadruple spectrometer.

4.2.5 Disinfecting Ability of La_xMnO_3 (x=1, 0.95, 0.9)

Quantity of La_xMnO_3 (x=1, 0.95, 0.9) for disinfection experiments were achieved by drop coating as-prepared materials (40 mg/mL aqueous solution) onto round glass cover slips and dried under room temperature. The amount of materials was marked as surface concentration, varied from 5 μg/mm^2 to 20 μg/mm^2. The disinfecting abilities of as-prepared La_xMnO_3 (x=1, 0.95, 0.9) samples were examined by $TCID_{50}$ (tissue culture infectious dose 50) assay with A/PR/8/34 H1N1 influenza A virus (PR8) on MDCK (Madin-Darby Canine Kidney) cell line. Cover slips coated with as-prepared La_xMnO_3 (x=1, 0.95, 0.9) were placed into a 48 well-plate as one slip per well and empty cover slips were set up in the same way as controls. Then PR8 with flu growth medium (15 μL, 3.57×10^5 $TCID_{50}$/mL) was deposit onto each cover slip and the plate was thoroughly wrapped by aluminum foil and placed on ice for 15 min. Finally PR8 was washed out; 10-fold serially diluted and got to infect the MDCK cells. The infectivity was calculated by Reed-Muench method after cells were incubated 72 hr. The experiments were

carried out in quadruplicate. Disinfecting efficiency was characterized as relative remaining infectivity.

4.2.6 Deactivation of Hemagglutinin

In hemagglutinin (HA) deactivation assay, washed pooled chicken red blood cells (10% in Alsever's solution, Lampire Biological Laboratories) were diluted to 1% using PBS buffer solution right before the experiment. After 2 hr treatment by as-coated slips ($La_{0.9}MnO_3$, 20 μg/mm^2), PR8 with flu growth medium (100 μL, 3.57×10^5 $TCID_{50}$/mL) was added into the first column of a Corning V-bottom 96-well plate, which was then 2-fold serially diluted across the 96 well plate with PBS. The final 50 μL from each well of the last column was disposed. Then 50 μL freshly diluted chicken red blood cells (1%) was added to each well and mixed by gently tapping the plate. The plate was incubated for 30 min at 4 °C and HA Unit (HAU) was observed directly from end point of agglutination phenomena. Experiments were carried out in triplicate.

4.2.7 Deactivation of Neuraminidase

The neuraminidase (NA) deactivation assays were carried out in a 48-well plate. As-coated slips ($La_{0.9}MnO_3$, 20 μg/mm^2) were immersed in 30 μL neuraminidase solution (1 UN/mL, Type V, Clostridium perfringens) on ice for 1 hr. Then 6 μL solution was taken out and mixed with 50 μL of 5 mM 2'-(4-Methylumbelliferyl) -α-D-N-acetylneuraminic acid sodium salt hydrate aqueous solution, 550 μL of 100 mM sodium acetate buffer with 2 mM calcium chloride, and incubated at 37 °C . After 30 min, 200 μL of 200 mM glycine buffer (pH 10.7) was added and the fluorescence signal from 400 to 500 nm was collected using a QuantaMaster

Spectrofluorometer (Photon Technology International) with an exciting wavelength of 365 nm. The emission intensity at 450 nm was used to compare the activity of neuraminidase.

4.3 Results and Discussion

4.3.1 Characterization of Perovskite-structured $LaMnO_3$

Figure 4.2 showed the XRD patterns of La_xMnO_3 (x=1, 0.95, 0.9) samples calcined at 700 °C. The diffraction patterns of La_xMnO_3 could be assigned to a rhombohedral perovskite-structured oxide phase with a space group of $R\bar{3}c$. It was worth noticing that no diffraction peak of Mn_3O_4 phase appeared in the $La_{0.95}MnO_3$ and $La_{0.9}MnO_3$ samples, which was in agreement with other reports.[161-162]

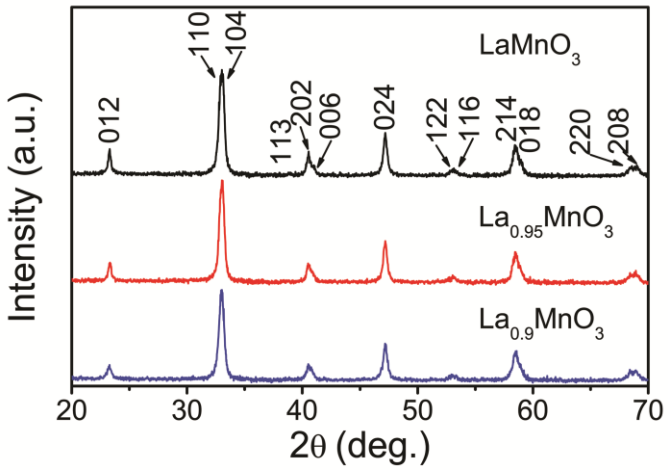

Figure 4.2 The XRD patterns of the La_xMnO_3 (x=1, 0.95, 0.9) samples.

The electron configuration of Mn^{4+} ions in an octahedral field ($^4A_{2g}$) allowed observing their EPR spectrum at room temperature.[163] Thus, we investigated Mn^{4+} ions signal of the La_xMnO_3 (x=1, 0.95, 0.9) samples by EPR measurement. As shown in **Figure 4.3**, a unique signal with *g*-value around 1.99 was detected for all La_xMnO_3 (x=1, 0.95, 0.9) samples, which was correlated with Mn^{4+} ions.[164] Due to the fact that intensity of Mn^{4+} ions was proportion to the double integrated area of EPR spectrum, we compared the concentration of Mn^{4+} ions among the La_xMnO_3 (x=1, 0.95, 0.9) samples.[165] The double integrated area ($La_{0.9}MnO_3$ ~ 7.88×10^{11};

$La_{0.95}MnO_3$ ~ 2.95×10^{11}; $LaMnO_3$ ~ 1.14×10^{11}) increased with decreasing of La/Mn ratio. Therefore, the lower La/Mn ratio achieved the higher concentration of Mn^{4+} ions in the La_xMnO_3 (x=1, 0.95, 0.9) samples, which correlated to higher oxidative ability.[161,166]

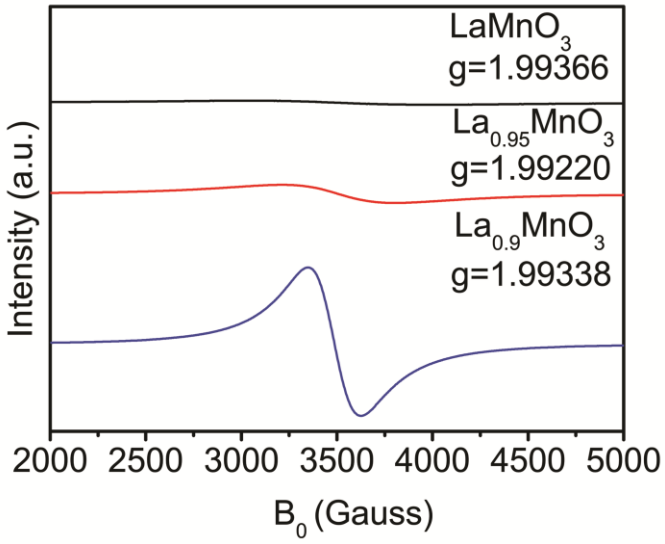

Figure 4.3 The EPR spectrum of the La_xMnO_3 (x=1, 0.95, 0.9) samples.

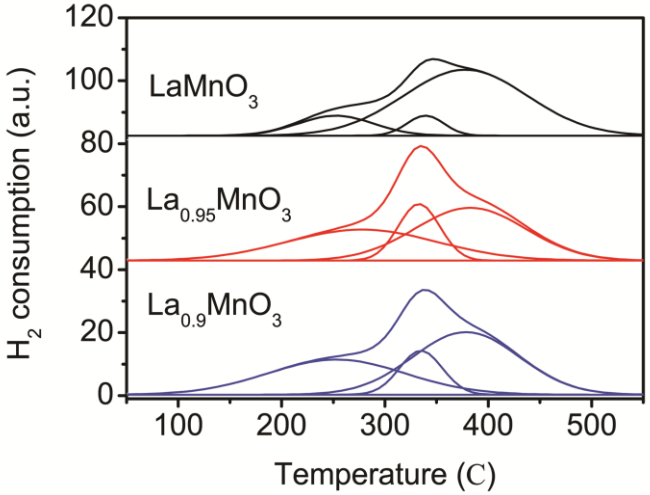

Figure 4.4 The H_2-TPR profiles of the La_xMnO_3 (x=1, 0.95, 0.9) samples.

Table 4.1 The integrated peak area of the La_xMnO_3 (x=1, 0.95, 0.9) samples.

	250-260 °C	330-340 °C	370-380 °C
$LaMnO_3$	155	138	2716
$La_{0.95}MnO_3$	1722	846	2183
$La_{0.9}MnO_3$	2125	993	2829

The results of H_2-TPR experiments performed on the La_xMnO_3 (x=1, 0.95, 0.9) samples were depicted in **Figure 4.4**. The La_xMnO_3 (x=1, 0.95, 0.9) samples were characterized by the presence of three H_2 reduction peaks based on temperature, which indicated the multiple sites for the reduction of perovskites. The first peak located at the temperature of 250-260 °C could be assigned to the removal of non-stoichiometric excess oxygen accommodated within the lattice. The following two peaks located at 330-340 °C and 370-380 °C were attributed to the reduction of Mn^{4+} to Mn^{3+}.[166-167] In order to further investigate the Mn^{4+} ions amount in the La_xMnO_3 (x=1, 0.95, 0.9) samples, we integrated the peak area of them in **Table 4.1**. It was noted that the integrated peak area assigned to the reduction of Mn^{4+} to Mn^{3+} in the La_xMnO_3 (x=1, 0.95, 0.9) samples was getting larger while the ratio of La/Mn was decreased, which indicated the more amount of Mn^{4+} ions at x = 0.9 and corresponded well to the EPR results.

4.3.2 Disinfection of Influenza A Virus

The disinfecting ability of as-prepared La_xMnO_3 (x=1, 0.95, 0.9) samples on PR8 was marked as relative infectivity and displayed in **Figure 4.5**. It has been observed that the disinfecting ability was increased with higher surface concentration and with lower La/Mn ratio (**Figure 4.5a**). The best disinfection was achieved by $La_{0.9}MnO_3$ (20 μg/mm^2) as 76% of PR8 was deactivated with only 15 min contacting, while no other special condition was supplied, included but not limited to lighting, heating or special atmosphere. Also we proved that

infectivity of PR8 has been reduced significantly over time (**Figure 4.5b**), which suggested La_xMnO_3 (x=1, 0.95, 0.9) was continuous disinfecting the virus and the disinfection was not attributed to absorption between as-prepared La_xMnO_3 (x=1, 0.95, 0.9) and PR8 viral particles but the reaction between them.

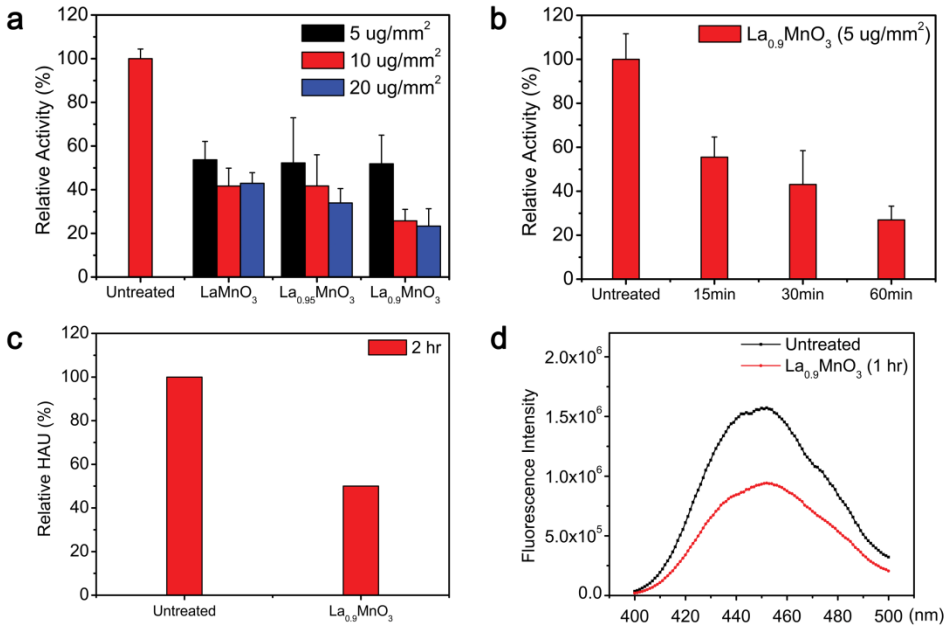

Figure 4.5 Disinfection of influenza A virus. (**a**) Disinfecting ability of La_xMnO_3 (x=1, 0.95, 0.9) samples got better with the increase of the surface concentration, $La_{0.9}MnO_3$ showed the best disinfecting ability of 76% on PR8 in 15 min with surface concentration of 20 μg/mm^2 and the infectivity of PR8 kept decreasing with time (**b**). Mechanism study showed that hemagglutinin (**c**) and neuraminidase (**d**) have been deactivated after treated by $La_{0.9}MnO_3$.

By correlating observed different disinfecting efficiency of La_xMnO_3 (x=1, 0.95, 0.9) samples with oxidative ability comparison of different La/Mn ratio, we confidently believe that the disinfection of PR8 involved the oxidative ability of La_xMnO_3 (x=1, 0.95, 0.9). In detail, $La_{0.9}MnO_3$ has the best disinfecting ability in all samples with the same concentration that suggested the most reaction has taken place between the virus and $La_{0.9}MnO_3$ particles, which

was considered as oxidizing virus by $La_{0.9}MnO_3$ particles. On the other hand, theoretical calculation, previous report and our EPR and H_2-TPR results all suggested the maximum amount of Mn^{4+} ions in $La_{0.9}MnO_3$ among La_xMnO_3 (x=1, 0.95, 0.9) samples, indicating the highest oxidative ability of $La_{0.9}MnO_3$. Thus the most disinfecting efficiency on PR8 influenza virus on $La_{0.9}MnO_3$ was well explained.

4.3.3 Disinfection Mechanism

To further specify the mechanism behind disinfecting phenomena, deactivation of the two critical envelope proteins on influenza virus, hemagglutinin (HA) and neuraminidase (NA), by as-prepared $La_{0.9}MnO_3$ were separately investigated. HA could binding to sialic acid receptor introduce virus genome into the cell and NA could cleave the sialic acid residues therefore release the newly reproduced viral particles and prevent them for aggregation. Deactivation of HA was examined by testing the binding ability on red blood cells, which was noted as HA unit (HAU). After 2 hr contact with 20 μg/mm^2 $La_{0.9}MnO_3$, only half of viral HA was working properly (**Figure 4.5c**). On the other hand, activity of NA was characterized by fluorescence substrate after 1 hr contact with 20 μg/mm^2 $La_{0.9}MnO_3$ and similarly only 60% of original activity was retained (**Figure 4.5d**). These results firmly testified our hypothesis, meanwhile suggested the possibility that the oxidative species might penetrate viral particles and damage the genetic materials, which could also result in 76% loss of infectivity as the best total disinfection of PR8.

4.4 Conclusion and Future Direction

In conclusion, non-stoichiometric perovskite-structured La_xMnO_3 (x=1, 0.95, 0.9) has been successfully synthesized and demonstrated its spontaneous, continuous and external conditions free disinfection phenomena on PR8 H1N1 influenza virus. The oxidative ability of different stoichiometric ratio has been investigated by EPR and H_2-TPR, that $La_{0.9}MnO_3$ owned the best oxidative ability and accordingly presented the best disinfecting efficiency within them three, 76% disinfection in 15 min contact. We believe that further development of coating, molding and *in situ* synthesis technology can utilize La_xMnO_3's feature of anti-pathogens in self-disinfecting air filters, moreover due to its oxidizing mechanism, disinfectable pathogens should include but not limit to viruses, bacteria and even fungi.

For the future direction, methods to achieve high mechanic stress coatings for La_xMnO_3 (x = 1, 0.95, 0.9) should be investigated to make more promising application of this kind of self-disinfecting coatings.

Chapter 5 Novel Adenovirus Nanogel as Gene Delivery Vector with Enhanced Stability

5.1 Background Introduction

5.1.1 Motivation: Adenovirus as DNA Delivery Vector

Gene therapy as a medical treatment based on understanding genetic and biomolecular basis of our live promises a beautiful map to cure almost all the diseases. Even early clinical trial failed to show efficacy,[168] extensive research efforts have been continuously injected into this field. However, people are not pursuing success on specific disease but turn to understand the biology of interactions between gene delivery vector and the human immune system, which could result in fetal consequences. Discovery in gene-transfer techniques has allowed the development of more efficient, specific and safer delivery vectors.

Viruses are superb efficient in delivery their own genome to the host cell and exploit the cellular machinery in order to facilitate self-replication. Viruses have caused severe pandemics in human history; however, they also serve as fantastic gene transfect vector in gene therapy after deleting all or some of their own viral genome, reserving functional proteins or gene codes and incorporating therapeutic genes. Mainly there are five types of viral vectors applicable for clinical transfection derived from oncoretroviruses, lentiviruses, adenoviruses, adeno-associated viruses (AAVs) and herpes simplex-1 viruses (HSV-1s).[169]

As bio-functional particles, vectors are usually sensitive to changing of environment conditions as temperature, humidity, adverse pH and chemicals. Also directly modification on vectors may also induce loss of transfection efficiency or additional immunogenicity. Thus by combining polymer nanogel techniques developed by Lu, et al,[92] a novel adenovirus nanogel has been designed and proved in prolonged stability for long-term storage and transportation. In

addition, further modification on the outer polymer shell has possibility in achieving targeting selectivity and *in vivo* lower immunogenicity.

5.1.2 Research Objective

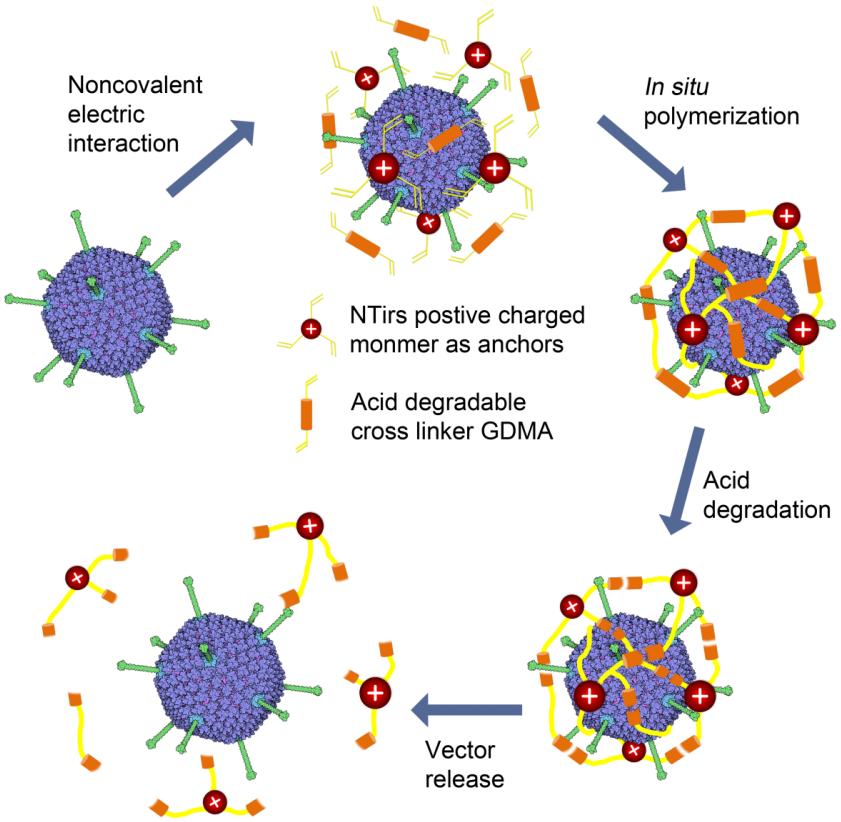

Figure 5.1 Design of novel adenovirus nanogels utilizes non-covalent electric interaction to anchor polymer shell onto surface of adenovirus.

As adenoviruses highly rely on their surface proteins during infection, conjugating polymerizable acryl groups covalently to adenovirus' surface proteins as anchors of polymer shell by reacting amine group of surface proteins with n-acryloxysuccinimide has been proved resulting significant loss of infectivity. Thus novel polymer shell should be designed by engineering virus-polymer interface as utilizing non-covalent electric interaction between

monomers and adenoviruses as the anchor. By adding acid degradable crosslinker and initiating *in situ* free radical polymerization near the surfaces of adenoviruses, the adenoviruses would be wrapped to form nanogel as shown in **Figure 5.1**. The adenovirus could still be released in the acidified lysosome. A luciferase expressing adenoviral vector, AdCMVLuc, would be employed as the demonstration. All the terms "adenovirus" are referring to AdCMVLuc in this chapter. As-prepared nanogel would be expected to achieve long-term stability for the adenovirus vector at 4 °C.

5.2 Experimental Procedure

5.2.1 Covalently Conjugation of Polymerizable Acryl Groups onto Adenovirus Capsid

To prove the loss of infectivity by covalently conjugating polymerizable acryl groups onto adenovirus surface proteins, different amount of 1 mg/mL n-acryloxysuccinimide (NAS) in dimethyl sulfoxide (DMSO) were added into 10 μL of adenovirus solution (50 μg/mL in phosphate buffered saline (PBS)) to achieve the molar ratio as 125, 250, 500, 1000 and 2000. The mixture was reacted in ice bath for 2 hr then infected HeLa cell at multiplicity of infection equaled to 10 (MOI = 10).

5.2.2 Synthesis of Positively Charged Monomer

Non-covalent electric interaction has been employed to anchor polymer shell to surface of adenovirus virion. Monomer with positive charge center has been designed and synthesized, as in the route shown in **Figure 5.2.**

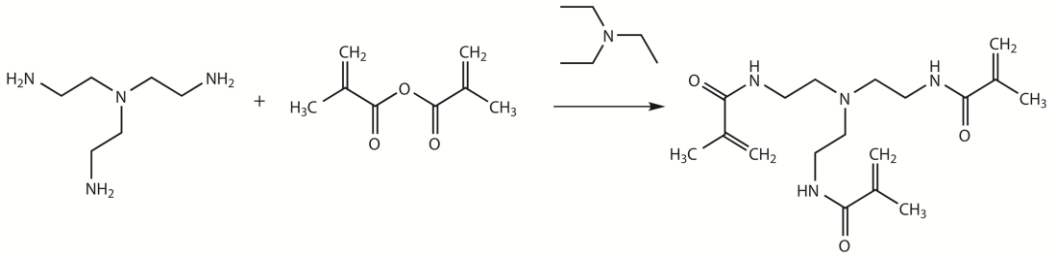

Figure 5.2 Synthesis route of positively charged monomer.

In a typical synthesis, 0.492 mmol of methacrylic anhydride and 0.615 mmol of triethylamine were dissolved in 1 mL acetonitrile in the ice/water bath with vigorous stirring, mark as solution A, and 20 mg tris (2-aminoethyl)amine was dissolved in another 1 mL acetonitrile and dripped into solution A and react for 8 hr. Then the solution was dried in vacuum

and dark condition. After that, the compound was dissolved in 500 μL methanol and isolated by the silica gel chromatography, which mobile phase was chloroform and methanol with volume ratio 12 to 1. Final product was named as NTris for convenience. Purified NTris was dried in vacuum and dark condition again then stored under -80 °C.

5.2.3 Synthesis of the Novel Adenovirus Nanogel

AdCMVLuc has been employed as the model delivery vector and all the adenovirus in my experiments refers to AdCMVLuc. Typically, 10 μL of adenovirus solution (0.5 mg/mL in 10 mM tris buffer with 1 mM Mg^{2+}, pH 8), 1 μL of NTris DMSO solution (4%), 1 μL of glycerol dimethacrylate (GDMA) DMSO solution (4%), 6.4 μL of ammonium persulphate in aqueous solution (dilute 100 times from fresh prepared 5% wt. aqueous solution), 6.4 μL of N,N,N',N'-tetramethylethylenediamine aqueous solution (dilute 100 times from fresh prepared 1% aqueous solution) and 75.2 μL of tris buffer (10 mM tris buffer with 1 mM Mg^{2+}, pH 8) were mixed and reacted in ice bath for 2 hr. Then adenovirus nanogels are dialyzed to the same tris buffer.

5.2.4 4 °C Stability of the Novel Adenovirus Nanogel

Acid degradation has been employed to help degrading polymer shell by mix as-prepared adenovirus nanogels with pH 5 acetate buffer (1 M) and incubated 30 min in 4 °C.

Day 1, adenovirus nanogels were synthesized and dialyzed with 10 mM tris buffer with 1 mM Mg^{2+}, pH 8 for overnight. 48 well plates were seeded with HeLa cells (1×10^4 cell per well).

Day 2, dialyzed adenovirus nanogel and native adenovirus were aliquot to several 1.5 mL centrifuge tubes and stored at 4 °C. Took each tube of samples and diluted to 5 times in volume with pH 5 acetate buffer (1 M) for acid degradation. Firstly certain amount of adenovirus

nanogels or viruses was added into 48 well plate seeded on Day 1 to achieve MOI = 10, immediately after mixed with acid buffer. Then after 30 min, acid degraded adenovirus nanogel and native virus were added again to other wells. All the samples were tested in triplicates. Finally infected cell plate was incubated for 3 days and luciferase assays were carried out to determine infectivity.

Day 5, luciferase assays were carried out to determine the infectivity of fresh prepared adenovirus nanogel.

Day 11, 48 well plates were seeded with HeLa cells (1×10^4 cell per well).

Day 12, the same process of Day 2 was repeated.

Day 15, luciferase assays were carried out for the infection on Day 12, to determine the stability of as-prepared adenovirus nanogel.

5.2.5 Luciferase Assay

Firefly Luciferase Assay kit was purchased from Promega, cat# E1501. The standard protocol was followed.[170] Briefly, infected cells were lysed and collected into 1.5 mL centrifuge tubes and centrifuged for 10 min at 3,000 rpm. Supernatants were mixed with substrate then chemiluminescent signals were recorded by a FB12 Single Tube Luminometer from Berthold Detection System.

5.3 Results and Discussion

5.3.1 Modification of Amine Group Resulted Significant Loss in Infectivity

Covalent conjugation of polymerizable acryl groups to surface of adenovirus as anchor of polymer shell has been proved extreme harsh to infectivity of adenovirus. In **Figure 5.3**, molar ratios of NAS to virions are 125, 250, 500, 1000 and 2000.

As shown in **Figure 5.3**, infectivity of modified adenovirus has dropped significantly comparing to native adenovirus. Recalled from introduction, adenovirus highly depends on its surface proteins not only for targeting and induces endocytic entry process but also need these proteins for later releasing to cytoplasm and dissociating its capsid. Thus even the first step, targeting and induce entry, could be substituted by other functional group later labeled onto outer polymer shell, the second step still get suppressed. Thus this design should not be taken as anchoring method for the polymer shell.

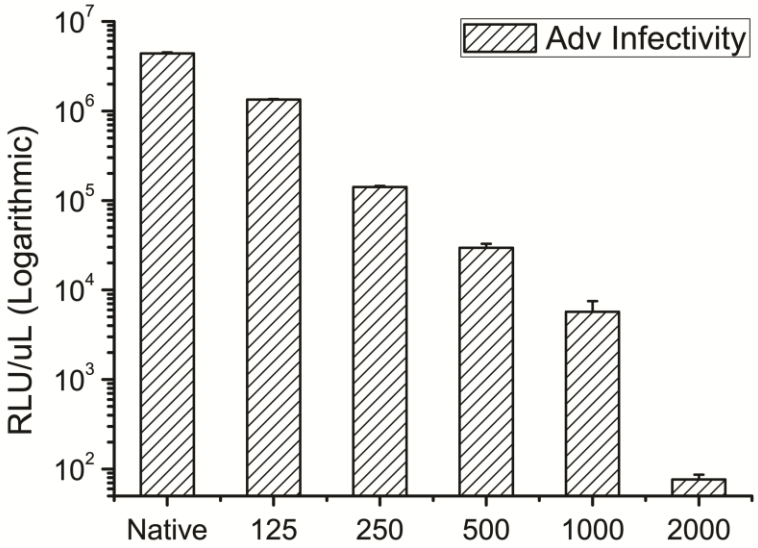

Figure 5.3 Loss of infectivity by covalently conjugating acryl groups onto adenovirus surface proteins.

5.3.2 NMR Characterization of Synthesized NTris Monomer

Nuclear Magnetic Resonance was utilized for characterizing as-prepared monomer and the spectrum was displayed in **Figure 5.4**. The first group of chemical shifts around 1 ppm was donated by methyl group, which was quartet peaks, and the peak area showed three of them exist. Then six methylene groups appeared as a triplet of doublets. After that, the group appeared around 3.5 ppm was considered as H-C(sp^2)-H coupling and three of them was found by peak area. Thus the structure in synthesis route **Figure 5.3** was confirmed. However, either precursor or deuterium oxide as NMR solvent has been contaminated so some peaks could not be recognized.

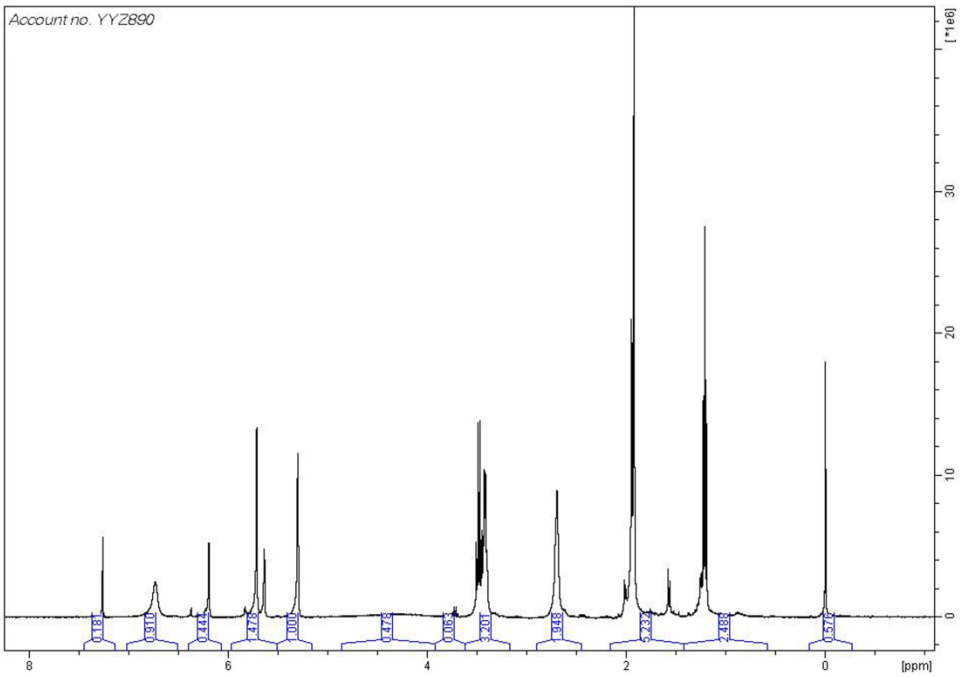

Figure 5.4 NMR spectrum of as-prepared NTris monomer.

5.3.3 DLS Characterization of NTris Adenovirus Nanogel

Dynamic light scattering was carried out in pH 8 tris buff with Mg^{2+} to determine size distribution and zeta potential of as-prepared NTris adenovirus nanogels. As shown in **Figure**

5.5, as-prepared nanogels have a negative zeta potential around -27 mV in pH 8 tris buffer, which should be stabilize enough against thermodynamic aggregation. The size distribution of native adenovirus has been examined around 78 nm as the reference. The size distribution of as-prepared NTris adenovirus nanogels were averaged around 100 nm, which also confirmed successful wrapping of adenovirus.

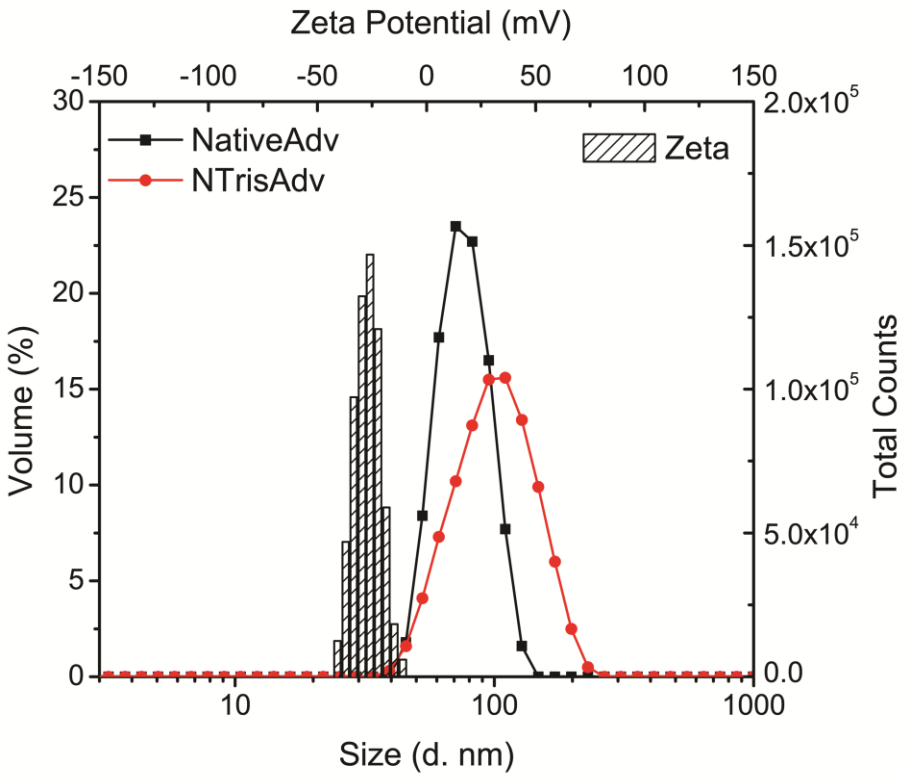

Figure 5.5 DLS characterization of as-prepared NTris adenovirus nanogel. Bottom-left axes with black and red lines are size distribution of native adenovirus (NativeAdv) and NTris adenovirus nanogel (NTrisAdv). Top-right axes with shadowed columns are zeta potential of NTris adenovirus nanogel.

5.3.4 Enhanced 4 °C Stability of NTris Adenovirus Nanogel

Stability of NTris adenovirus nanogels was compared with native adenoviruses, their luciferase assay results were plotted in **Figure 5.6**. Relative infectivity was calculated using

infectivity of native virus on the experiment day as reference respectively and notation "acid" means the samples were acid-degraded for 30 min before infecting the cells. In **Figure 5.6a**, relative infectivity results showed that native virus was as 3 times as infectivity of NTris adenovirus nanogel on Day 2, which they were fresh made right after dialysis. However, it dropped to a quarter of the infectivity of as-prepared nanogels on Day 12. This change could be read more specifically on **Figure 5.6b**, that infectivity of native adenovirus dropped from 3.7×10^5 RLU/μL on Day 2 to 2.2×10^3 RLU/μL on Day 12, while infectivity of as-prepared nanogel decreased from 1.4×10^5 RLU/μL to 9.6×10^3 RLU/μL, respectively. These results confirmed more than 11 folds of enhanced stability of our designed novel nanogel for adenovirus after 12 days at 4 °C.

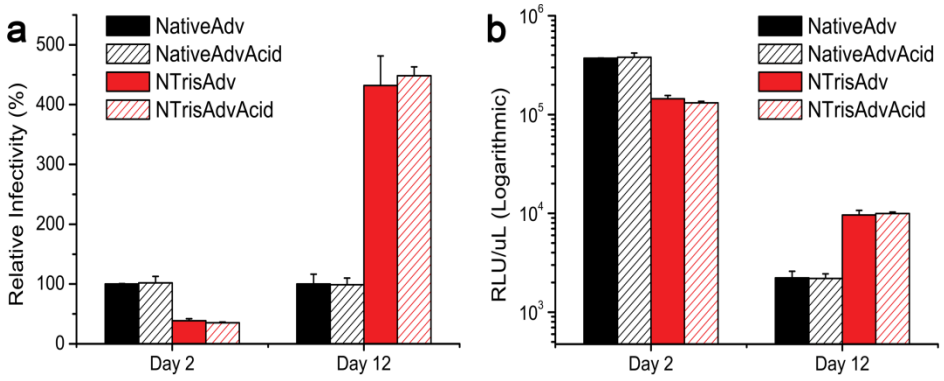

Figure 5.6 Enhanced 4 °C stability of NTris adenovirus nanogel. (**a**) presents relative infectivity, which use native virus infectivity as reference respectively to the date. (**b**) presents specific infectivity of the same data in **a**, which reflects the infectivity drop of native adenovirus and enhanced stability of as-prepared nanogel more apparently. Notation "Acid" means the samples were acid-degraded for 30 min before infect the cells. However, not much enhancement in adverse pH has been found.

Not much enhancement in the stability for adverse pH has been found. It should be understandable that native adenovirus must be sustainable during acidify of endosome to lysosome in order to achieve releasing their genome to infect host cell. However, no changing

for pre acid-degradation of polymer shell indicated that the shell perhaps blocks infectivity of adenovirus nanogel thus caused loss in efficiency. On the other hand, it also proved that polymer shell was able to be dissociated inside the cell endosome otherwise no infectivity should be detected. Thus using acid-degradable cross linker GDMA was a good choice, but the ratio need be optimized.

5.4 Conclusion and Future Direction

In conclusion, novel adenovirus nanogel has been designed and synthesized successfully. By utilizing non-covalent electric interaction, activity of surface proteins of adenoviruses was not affected as covalently modified adenovirus. The infectivity of as-prepared adenovirus nanogel has been proved as 4 times as of native adenovirus after 12 days storage from the synthesis at 4 °C. Thus this novel adenovirus nanogel has great potential application in transport and storage for gene delivery vectors. Furthermore, this kind of technique opened possibility in controllability of surface charge and targeting selectivity for gene delivery vectors by controlling monomer in polymer shell and further modification with targeting peptides or groups on the polymer shell instead of on surface proteins of adenovirus, which would result significant loss of deliver efficiency.

As wrapping by polymer, targeting ability of adenovirus has been somewhat blocked thus the fresh made samples didn't obtain 100% infectivity as native adenovirus. Adding targeting peptides as CD4 or RGD and cell penetrating peptide TAT on to surface of the nanogel should be able to improve delivery efficiency and control the targeting selectivity. And adjust zeta potential of as-prepared novel adenovirus nanogel could future increase the infectivity as positive charge may induce non-targeting endocytosis. This should be future direction of this project. Moreover, although GDMA has been added on purpose of making polymer shell degradable, there wasn't significant difference between acid-degraded samples and non-acid degraded samples. Therefore, monomer ratio and acid-degrading time need get optimized.

Chapter 6 Thesis Conclusion

Through the engineering of the nanocrystal-nanocrystal interface, virus-nanocrystal interface, and virus -polymer interface, this dissertation mainly unveils three topics that are related to energy harvesting and health care.

By engineering nanocrystal-nanocrystal interface, the first topic, *dissimilar nanocomposites for thermoelectric materials*, presented, 1) developing facile synthesis methods for PbTe based thermoelectric materials, 2) designing and preparing phonon-glass electron-crystal structure devices based on two different nanocrystals, 3) suppressed thermal conductivity of as-prepared dissimilar nanocomposites similar to that of the superlattice structure, which has almost approached the lowest theoretical calculated results.

By controlling virus-nanocrystal interface, the second topic, *self-disinfection antiviral coatings*, presented, 1) synthesis and characterizing visible light powered self-disinfecting coatings based on $CuInZn_4S_6$, 2) surface exchanging for better contact of nanocrystals and virus containing droplets, 3) rapid disinfection as killing 74% of influenza A virus in 15 min and over 94% in 2 hr under visible light irradiation, 4) the eligibility in disinfecting other virus like hepatitis C virus and even bacteria, 5) the evidences that photogenerated oxidative free radicals reacted with amino acid residues of the surface proteins and eventually caused the proteins to malfunction. Following this disinfection mechanism, external condition independent self-disinfecting coating was presented, 1) synthesis of non-stoichiometric LaxMnO3, x = 1, 0.95, 0.9, 2) the highest Mn^{4+} oxidative ability from $La_{0.9}MnO_3$ in hydrogen temperature programmed reduction (H_2-TPR) and electron paramagnetic resonance (EPR), 4) the best disinfecting performance from $La_{0.9}MnO_3$ in the dark condition as killing 76% of influenza A virus in 15 min. 4) similar mechanism as in as in $CuInZn_4S_6$ self-disinfecting coatings.

By designing virus-polymer interface, the third topic, *polymer stabilized virus vector for gene delivery*, presented, 1) design of non-covalently conjugated acid degradable polymer shell on adenovirus, 2) utilizing non-covalent electric interaction as anchors between positively charged monomer and negatively charged viral capsid, 3) more than 11 folds of enhanced stability on adenovirus nanogel after 12 days storage at 4 °C.

In summary, precisely engineering nanocrystal-nanocrystal interface, virus-nanocrystal interface, and virus-polymer interface achieved dissimilar nanocomposites for thermoelectric materials, self-disinfecting antiviral coatings, and polymer stabilized virus vector for gene delivery. The capability to synthesize and controlling huge families of nanomaterials provides solutions to much more problems in energy harvesting and health care issues and supports human society for sustainable development in the future. This dissertation just serves as a beginning.

References

1 Matsubara, K. Development of a High Efficient Thermoelectric Stack for a Waste Exhaust Heat Recovery. in *Proceedings of the 21st international Conference on Thermoelectrics.* (ed T. Caillat) p. 418 (2002).

2 Matsubara, K. & Matruura, M. in *CRC Thermoelectrics Handbook: Macro to Nano* (ed D. M. Rowe) p. 52-3 (CRC Press, 2006).

3 Seebeck, T. J. The magnetic polarization of metals and ores produced by temperature difference. *Proc.Prussian Acad. Sci.*, 265-373, (1822).

4 Peltier, J. C. Nouvelles experiences sur la caloriecete des courans electriques. *Ann. Chem.* **LVI**, 371-387, (1834).

5 Thomson, W. On a Mechanical Theory of Thermoelectric Currents. *Proc. Roy. Soc. Edinburgh* 91-98, (1851).

6 Thomson, W. Account of Researches in Thermoelectricity. *Proc. Roy. Soc. London* **7**, 49-58, (1854).

7 Roberts, R. B. Absolute Scale of Thermoelectricity. *Nature* **265**, 226-227, (1977).

8 Ioffe, A. F. *Semiconductor thermoelements and Thermoelectric cooling*. (Infosearch, ltd., 1957).

9 Ashcroft, N. W. & Mermin, N. D. *Solid state physics*. (Saunders College, 1976).

10 Slack, G. A. in *CRC Handbook of Thermoelectrics* (ed D. M. Rowe) p. 407 (CRC Press, 1995).

11 Goldsmid, H. J. *Thermoelectric Refrigeration*. (Plenum Press, 1964).

12 Dresselhaus, M. S. *et al.* in *Semiconductors and Semimetals: Recent Trends in Thermoelectric Materials Research III* Vol. 71 (ed T. M. Tritt) p. 1-121 (Academic Press, 2001).

13 Scheidemantel, T. J., Ambrosch-Draxl, C., Thonhauser, T., Badding, J. V. & Sofo, J. O. Transport Coefficients from First-principles Calculations. *Phys. Rev. B* **68**, 125210-1 - 125210-6, (2003).

14 Lee, S. & Allmen, P. v. Tight-Binding Modeling of Thermoelectric Properties of Bismuth Telluride. *Appl. Phys. Lett.* **88**, 22107-1 - 22107-3, (2006).

15 Venkatasubramanian, R., Siivola, E., Colpitts, T. & O'Quinn, B. Thin-Film Thermoelectric Devices with High Room-Temperature Figures of Merit. *Nature* **413**, 597-602, (2001).

16 Harman, T. C., Taylor, P. J., Walsh, M. P. & LaForge, B. E. Quantum Dot Superlattice Thermoelectric Materials and Devices. *Science* **297**, 2229-2232, (2002).

17 Hsu, K. F. *et al.* Cubic $AgPb_mSbTe_{2+m}$: Bulk Thermoelectric Materials with High Figure of Merit. *Science* **303**, 818-821, (2004).

18 Fluerial, J. P., Caillat, T. & Borshchevsky, A. in *Proceedings of the 13th International Conference on Thermoelectrics.* p. 40-44 (1994) (AIP, New York).

19 Kanatzidis, M. G. Department of Chemistry, Northwestern University, <http://chemgroups.northwestern.edu/kanatzidis/greatthermo.html> (Last update, Nov 17 2009).

20 Ghamaty, S., Elsner, N. & Bass, J. Recent Progress in the Development of High Efficiency Thermoelectrics. in *2003 Diesel Engine Emissions Reduction (DEER) Conference Presentations.* (Newport, Rhode Island 2003).

21 Heremans, J. P. *et al.* Enhancement of Thermoelectric Efficiency in PbTe by Distortion of the Electronic Density of States. *Science* **321**, 554-557, (2008).

22 Online Etymology Dictionary. <http://www.etymonline.com/index.php?term=virus>.

23 Zaitlin, M. in *Discoveries in Plant Biology* (ed S. D. Kung & S. F. Yang) p. 105-110 (Wolrd Publishing Co., 1998).

24 Beijerinck, M. W. Über ein Contagium vivum fluidum als Ursache der Fleckenkrankheit der Tabaksblätter. *Verhandelingen der Koninklijke akademie van Wetenschappen te Amsterdam* **65**, 1-22, (1898).

25 Casjens, S. in *Desk Encyclopedia of General Virology*) p. 167 (Academic Press, 2010).

26 Canchaya, C., Fournous, G., Chibani-Chennoufi, S., Dillmann, M. L. & Brüssow, H. Phage as agents of lateral gene transfer. *Curr. Opin. Microbiol.* **6**, 417-424, (2003).

27 Breitbart, M. & Rohwer, F. Here a virus, there a virus, everywhere the same virus? *Trends in Microbiology* **13**, 278-284, (2005).

28 Collier, L., Balows, A. & Sussman, M. *Topley and Wilson's Microbiology and Microbial Infections*. 9 edn, Vol. 1 Virology (1998).

29 Ryabchikova, E. I. & Price, B. B. *Ebola and Marburg Viruses - A View of Infection Using Electron Microscopy*. (Battelle Press, 2004).

30 wikipedia. <http://en.wikipedia.org/wiki/File:TobaccoMosaicVirus.jpg> (2008).

31 wikipedia. <http://en.wikipedia.org/wiki/File:Adenovirus_4.jpg> (2008).

32 wikipedia. <http://en.wikipedia.org/wiki/File:H1N1_navbox.jpg> (2009).

33 wikipedia. <http://en.wikipedia.org/wiki/File:3D_Influenza_virus.png> (2009).

34 wikipedia. <http://en.wikipedia.org/wiki/File:HIV_Virion-en.png> (2005).

35 wikipedia. File:PhageExterior.svg. (2009).

36 Temin, H. M. & Baltimore, D. RNA-Directed DNA Synthesis and RNA Tumor Viruses. *Advanced in Virus Research* **17**, 129-186, (1972).

37 Komaroff, A. Is Human Herpesvirus-6 a Trigger for Chronic Fatigue Syndrome? *Journal of Clinical Virology* **37 Supplement 1**, S39-S46, (2006).

38 Barton, E. S. *et al.* Herpesvirus Latency Confers Symbiotic Protection from Bacterial Infection. *Nature* **447**, 326-329, (2007).

39 Fowler, M. G., Lampe, M. A., Jamieson, D. J., Kourtis, A. P. & Rogers, M. F. Reducing the risk of mother-to-child human immunodeficiency virus transmission: past successes, current progress and challenges, and future directions. *Am. J. Obstet. Gynecol.*, (2007).

40 Sauerbrei, A. & Wutzler, P. The Congenital Varicella Syndrome. *J. Perinatol.* **20**, 548-554, (2000).

41 wikipedia. <http://en.wikipedia.org/wiki/1918_flu_pandemic> (2012).

42 Palese, P. Making Better Influenza Virus Vaccines. *Emerging Infect. Dis.* **12**, 61-65, (2006).

43 McLean, A. A. Development of vaccines against hepatitis A and hepatitis B. *Rev. Infect. Dis.* **8**, 591-598, (1986).

44 Magden, J., Kääriäinen, L. & Ahola, T. Inhibitors of virus replication: recent developments and prospects. *Appl. Microbiol. Biotechnol.* **66**, 612-621, (2005).

45 Presti, R. M. *et al.* Quaranfil, Johnston Atoll, and Lake Chad Viruses Are Novel Members of the Family Orthomyxoviridae. *J. Virol.* **83**, 11599-11606, (2009).

46 Jones, L. D. & Nuttall, P. A. Non-viraemic transmission of Thogoto virus: influence of time and distance. *Trans. R. Soc. Trop. Med. Hyg.* **83**, 712-714, (1989).

47 Ely, B. *Infectious Salmon Anaemia* (National Institute for Medical Research, Mill Hill, London, 1999).

48 Raynard, R. S., Murray, A. G. & Gregory, A. Infectious salmon anaemia virus in wild fish from Scotland. *Dis. Aquat. Org.* **46**, 93-100, (2001).

49 Nicholls, H. Pandemic Influenza: The Inside Story. *PLOS Biol* **4**, e50 156-160, (2006).

50 wikipedia. <http://en.wikipedia.org/wiki/Russian_flu> (2012).

51 Patterson, K. D. & Pyle, G. F. The geography and mortality of the 1918 influenza pandemic. *Bull. Hist. Med.* **65**, 4-21, (1991).

52 PBS. Influenza 1918. *American Experience* (1998).

53 Johnson, N. P. A. S. & Mueller, J. Updating the Accounts: Global Mortality of the 1918-1920 "Spanish" Influenza Pandemic. *Bull. Hist. Med.* **76**, 105-115, (2002).

54 Mahmoud, A. A. F. in *The Threat of Pandemic Influenza: Are We Ready? Workshop Summary* (ed S Knobler, A Mack, A Mahmoud, & S Lemon) p. 60-61 (The National Academies Press, 2005).

55 Barry, J. M. *The Great Influenza: The Epic Story of the Deadliest Plague in History*. (Viking Penguin, 2004).

56 Science and Technology Committee. Pandemic Influenza. (House of Lords, London, 2009).

57 Collier, R. *The Plague of the Spanish Lady: The Influenza Pandemic of 1918-1919*. (Macmillan, 1974).

58 Goldsmith, C. *Influenza: The Next Pandemic?* . (21st century publishing., 2007).

59 Greene, J. *The Bird Flu Pandemic*. 5 edn(St. Martin's Griffin, Moline, Karen).

60 Starling, A. E. *Plague, SARS, and the Story of Medicine in Hong Kong*. (HK University Press, 2006).

61 Flu.gov. <http://www.pandemicflu.gov/general/historicaloverview>.

62 WHO. <http://www.who.int/csr/don/2010_07_30/en/index.html> (2009).

63 NewScientist. <http://www.newscientist.com/article/dn17025-deadly-new-flu-virus-in-us-and-mexico-may-go-pandemic.html> (2009).

64 Throsby, M. *et al.* Heterosubtypic Neutralizing Monoclonal Antibodies Cross-Protective against H5N1 and H1N1 Recovered from Human IgM+ Memory B Cells. *PLoS ONE* **3**, e3942, (2008).

65 Ekiert, D. C. *et al.* Antibody Recognition of a Highly Conserved Influenza Virus Epitope. *Science* **324**, 246-251, (2009).

66 Barbey-Martin, C. *et al.* An Antibody That Prevents the Hemagglutinin Low pH Fusogenic Transition. *Virology* **294**, 70-74, (2002).

67 Meindl, P., Bodo, G., Palese, P., Schulman, J. & Tuppy, H. Inhibition of neuraminidase activity by derivatives of 2-deoxy-2,3-dehydro-N-acetylneuraminic acid. *Virology* **58**, 457-463, (1974).

68 Lew, W., Chen, X. & Kim, C. U. Discovery and Development of GS 4104 (oseltamivir): An Orally Active Influenza Nueraminidase Inhibitor. *Curr. Med. Chem.* **7**, 663-672, (2000).

69 Yamashita, M. *et al.* CS-8958, a Prodrug of the New Neuraminidase Inhibitor R-125489, Shows Long-Acting Anti-Influenza Virus Activity. *Antimicrob. Agents. Ch.* **53**, 186-192, (2009).

70 LifeHugger. <http://vol.lifehugger.com/wiki/Peramivir> (2009).

71 FDA. Tamiflu Prescribing Information. (2011).

72 Fujishima, A. & Honda, K. Electrochemical Photolysis of Water at a Semiconductor Electrode. *Nature* **238**, 37-38, (1972).

73 Zhang, L., Li, J., Chen, Z., Tang, Y. & Yu, Y. Preparation of Fenton Reagent with H_2O_2 Generated by Solar Light-Illuminated Nano-Cu_2O/MWNTs Composites. *Appl. Catal. A-Gen.* **299**, 292-297, (2006).

74 Zhang, L. *et al.* Sonochemical synthesis of nanocrystallite Bi_2O_3 as a visible-light-driven photocatalyst. *Appl. Catal. A-Gen.* **308**, 105-110, (2006).

75 Kim, H. G., Hwang, D. W. & Lee, J. S. An Undoped, Single-Phase Oxide Photocatalyst Working under Visible Light. *J. Am. Chem. Soc.* **126**, 8912-8913, (2004).

76 Kudo, A., Omori, K. & Kato, H. A Novel Aqueous Process for Preparation of Crystal Form-Controlled and Highly Crystalline $BiVO_4$ Powder from Layered Vanadates at Room Temperature and Its Photocatalytic and Photophysical Properties. *J. Am. Chem. Soc.* **121**, 11459-11467, (1999).

77 Finlayson, A. P., Tsaneva, V. N., Lyons, L., Clark, M. & Glowacki, B. A. Evaluation of Bi-W-Oxides for visible light photocatalysis. *Physica Status Solidi (a)* **203**, 327-335, (2006).

78 Zhang, L.-S. *et al.* Effective photocatalytic disinfection of *E. Coli* K-12 using AgBr-Ag-Bi_2WO_6 nanaojunction system irradiated by visible light: The role of diffusing hydroxyl radicals. *Environ. Sci. Technol.* **44**, 1392-1398, (2010).

79 Thomas, C. E., Ehrhardt, A. & Kay, M. A. Progress and Problems with the Use of Viral Vectors for Gene Therapy. *Nature Reviews Genetics* **4**, 346-358.

80 Lemieux, P. *et al.* Block and Graft Copolymers and Nanogel™ Copolymer Networks for DNA Delivery into Cell. *Journal of Drug Targeting* **8**, 91-105, (2000).

81 Dickerson, E. B. *et al.* Chemosensitization of cancer cells by siRNA using targeted nanogel delivery. *BMC Cancer* **10**, 10-1 - 10-11, (2010).

82 Blackburn, W. H., Dickerson, E. B., Smith, M. H., McDonald, J. F. & Lyon, L. A. Peptide-functionalized nanogels for targeted siRNA delivery. *Bioconjug. Chem.* **20**, 960-968, (2009).

83 Kohli, E., Han, H.-Y., Zeman, A. D. & Vinogradov, V. Formulations of biodegradable Nanogel carriers with 5'-triphosphates of nucleoside analogs that display a reduced cytotoxicity and enhanced drug activity. *J. Control Release* **121**, 19-27, (2007).

84 Lee, E. S., Kim, D., Youn, Y. S., Oh, K. T. & Bae, Y. H. A Virus-Mimetic Nanogel Vehicle. *Angew. Chem. Int. Ed. Engl.* **47**, 2418-2421, (2008).

85 Wagner, E., Culmsee, C. & Boeckle, S. Targeting of Polyplexes: Toward Synthetic VirusVector Systems. *Adv. Genet.* **53**, 333-354, (2005).

86 Remy, J.-S. *et al.* Gene transfer with lipospermines and polyethylenimines. *Adv. Drug Delivery Reviews* **30**, 85-95, (1998).

87 Kircheis, R., Wightman, L. & Wagner, E. Design and gene delivery activity of modified polyethylenimines. *Adv. Drug Delivery Reviews* **53**, 341-358, (2001).

88 Boeckle, S., Fahrmeir, J., Roedl, W., Ogris, M. & Wagner, E. Melittin analogs with high lytic activity at endosomal pH enhance transfection with purified targeted PEI polyplexes. *J. Control Release* **112**, 240-248, (2006).

89 Fisher, K. D. *et al.* Polymer-coated adenovirus permits efficient retargeting and evades neutralising antibodies. *Gene Therapy* **8**, 341-348, (2001).

90 Ichikawa, T. *et al.* Intraneoplastic polymer-based delivery of cyclophosphamide for intratumoral bioconversion by a replicating oncolytic viral vector. *Cancer Res.* **61**, 864-868, (2001).

91 Hallak, L. K., Merchan, J. R., Storgard, C. M., Loftus, J. C. & Russell, S. J. Targeted Measles Virus Vector Displaying Echistatin Infects Endothelial Cells via αvβ3 and Leads to Tumor Regression. *Cancer Res.* **65**, 5292-5300, (2005).

92 Yan, M. *et al.* A novel intracellular protein delivery platform based on single-protein nanocapsules. *Nature Nanotechnology* **5**, 48-53, (2010).

93 Hicks, L. D. & Dresselhaus, M. S. Effect of Quantum-Well Structures on the Thermoelectric Figure of Merit. *Phys. Rev. B* **47**, 12727-12731, (1993).

94 Hicks, L. D. & Dresselhaus, M. S. Thermoelectric Figure of Merit of a One-Dimensional Conductor. *Phys. Rev. B* **47**, 16631-16634, (1993).

95 Potter, C. W. A history of influenza. *J. Appl. Microbiol.* **91**, 572-579, (2001).

96 Webby, R. J. Are We Ready for Pandemic Influenza? *Science* **302**, 1519-1522, (2003).

97 Hilleman, M. R. Realities and enigmas of human viral influenza: pathogenesis, epidemiology and control. *Vaccine* **20**, 3068-3087, (2002).

98 Bean, B. *et al.* Survival of influenza viruses on environmental surfaces. *J. Infect. Dis.* **146**, 47-51, (1982).

99 Alford, R. H., Kasel, J. A., Gerone, P. J. & Knight, V. Human influenza resulting from aerosol inhalation. *Proc. Soc. Exp. Biol. Med.* **122**, 800-804, (1966).

100 Lidwell, O. M. Aerial dispersal of microorganisms from the human respiratory tract. *Soc. Appl. Bacteriol. Symp.* **3**, 135-154, (1974).

101 Tellier, R. Aerosol transmission of influenza A virus: a review of new studies. *J. Roy. Soc. Interface* **6**, S783-S790, (2009).

102 Somasundaram, S., Ming, Y., Chenthamarakshan, C. R., Schelly, Z. A. & Rajeshwar, K. Free Radical-Mediated Heterogeneous Photocatalytic Reduction of Metal Ions in UV-Irradiated Titanium Dioxide Suspensions. *J. Phys. Chem. B* **108**, 4784-4788, (2004).

103 Davies, M. J. Singlet oxygen-mediated damage to proteins and its consequences. *Biochem. Biophys. Res. Commun.* **305**, 761-770, (2003).

104 Timoshenko, V. *Singlet Oxygen Generation and Detection for Biomedical Applications*. Vol. II 295 (Springer, 2009).

105 Stadtman, E. R. Protein oxidation and aging. *Free Radical Research* **40**, 1250-1258, (2006).

106 Wright, A., Bubb, W. A., Hawkins, C. L. & Davies, M. J. Singlet Oxygen-mediated Protein Oxidation: Evidence for the Formation of Reactive Side Chain Peroxides on Tyrosine Residues. *Photochemistry and Photobiology* **76**, 35-46, (2002).

107 Wilkinson, F., Helman, W. P. & Ross, A. B. Rate constants for the decay and reactions of the lowest electronically excited state of molecular oxygen in solution. An expanded and revised compilation. *J. Phys. Chem. Ref. Data* **24**, 663-1021, (1995).

108 Straight, R. C. & Spikes, J. D. in *Singlet O_2* Vol. 4) p. 91-143 (CRC Press, 1985).

109 Papeschi, G., Monici, M. & Pinzauti, S. pH effect on dye sensitized photooxidation of aminoacids and albumins. *Med. Biol. Environ.* **10**, 245-250, (1982).

110 Michaeli, A. & Feitelson, J. Reactivity of singlet oxygen toward amino acids and peptides. *Photochemistry and Photobiology* **59**, 284-289, (1994).

111 Maskos, Z., Rush, J. D. & Koppenol, W. H. The hydroxylation of phenylalanine and tyrosine: a comparison with salicylate and tryptophan. *Arch Biochem Biophys* **296**, 521-529, (1992).

112 Wells-Knecht, M. C., Huggins, T. G., Dyer, S. R., Thorpe, S. R. & Baynes, J. W. Oxidized amino acids in lens protein with age. Measurement of o- tyrosine and dityrosine in the aging human lens. *J Biol Chem* **269**, 12348-12353, (1993).

113 Davies, K. J. A., Delsignore, M. E. & Lin, S. W. Protein damage by oxygen radicals. II. Modification of amino acids. *J. Biol. Chem.* **262**, 9902-9907, (1987).

114 Dean, R. T., Geisen, S. & Davies, M. J. Reactive species and their accumulation on radical-damaged proteins. *Trends Biochem Sci* **18**, 437-441, (1993).

115 Giulivi, C. & Davies, K. J. A. Dityrosine and tyrosine oxidation products are endogenous markers for the selective proteolysis of oxidatively modified red blood cell hemoglobin by the (19S) proteasome. *J. Biol. Chem.* **268**, 8752-8759, (1993).

116 Heinecke, J. W., Li, W., Daehnke, H. L. I. & Goldstein, J. A. Dityrosine, a specific marker of oxidation. *J Biol Chem* **268**, 4069-4077, (1993).

117 Winchester, R. V. & Lynn, K. R. X- and gamma-radiolysis of some tryptophan dipeptides. *Int Radiat Biol* **17**, 541-549, (1970).

118 Kikugawa, K., Kato, T. & Okamoto, Y. Damage of amino acids and proteins induced by nitrogen dioxide, a free radical toxin in air. *Free Radical Biology & Medicine* **16**, 373-382, (1994).

119 Gow, A., Duran, D., Thom, S. R. & Ischiropoulos, H. Carbon dioxide enhancement of peroxynitrite-mediated protein tyrosine nitration. *Arch Biochem Biophys* **333**, 42-48, (1996).

120 Armstrong, R. C. & Swallow, A. J. Pulse- and gamma-radiolysis of aqueous solutions of tryptophan. *Radiation Res* **41**, 563-569, (1969).

121 Tien, M., Berlett, B. S., Levine, R. L., Chock, P. B. & Stadtman, E. R. Peroxynitrite-mediated modification of protein at physiological carbon dioxide concentrations: pH dependence of carbonyl formation, tyrosine nitration, and methionine oxidation. *Proc Natl Acad Sci USA* **96**, 7809-7814, (1999).

122 Kettle, A. J. Neutrophils convert tyrosyl residues in albumin to chlorotyrosine. *FEBS Lett* **379**, 103-106, (1996).

123 Li, J., Billiar, T. R., Talanian, R. V. & Kim, Y. M. Nitric oxide reversibly inhibits seven members of the caspase family via S-nitrosylation. *Biochem Biophys Res Commun* **240**, 419-424, (1997).

124 Mannnick, J. B. *et al.* Fas-induced caspase denitrosylation. *Science* **284**, 651-654, (1998).

125 Stamler, J. S. Redox signaling: nitrosylation and related target interactions of nitric oxide. *Cell* **78**, 931-936, (1994).

126 Viner, R. I., Williams, T. D. & Schoeneich, C. Peroxynitrite modification of protein thiols: oxidation, nitrosylation, and S-glutathiolation of functionally important cysteine residue(s) in the sarcoplasmic reticu- lum Ca ATPase. *Biochemistry* **38**, 12408-12415, (1999).

127 Lavine, T. F. The formation, resolution, and optical properties of the diasteriomeric sulfoxides derived from L-methionine. *J Biol Chem* **169**, 477-491, (1947).

128 Vogt, W. Oxidation of methionine residues in proteins: tools, targets, and reversal. *Free Radical Biology & Medicine* **18**, 93-105, (1995).

129 Maier, K. L. *et al.* Different selectivities of oxidants during oxidation of methio- nine residues of the alpha-1 proteinase inhibitor. *FEBS Lett* **250**, 221-226, (1989).

130 Peskin, A. V. & Winterbourn, C. C. Kinetics of the reactions of hypo- chlorous acid and amino acid chloramines with thiols, methionine, and ascorbate. *Free Radical Biology & Medicine* **30**, 572-579, (2001).

131 Hawkins, C. L. & Davies, M. J. Hypochlorite-induced oxidation of proteins in plasma: formation of chloramines and nitrogen-centered radicals and their role in protein fragmentation. *Biochem J* **340**, 539-548, (1999).

132 Candeias, L. P., Patel, K. B., Stratford, R. L. & Wardman, P. Free hydroxyl radicals are formed between the neutrophil-derived species superoxide and hypochlorous acid. *FEBS Lett* **333**, 151-153, (1993).

133 Candeias, L. P., Stratford, M. R. L. & Wardman, P. Formation of hydroxyl radicals on reaction of hypochlorous acid with ferrocyanide, a model iron(II) complex. *Free Rad Res* **20**, 241-249, (1994).

134 Folks, L. K., Candeias, L. P. & Wardman, P. Kinetics and mechanisms of hypochlorous acid reactions. . *Arch Biochem Biophys* **323**, 120-126, (1995).

135 Stadtman, E. R. & Levine, R. L. Free radical-mediated oxidation of free amino acids and amino acid residues in proteins. *Amino Acids* **25**, 207-218, (2003).

136 Cerami, A., Vlassara, H. & Brownlee, M. Glucose and aging. *Sci Am* **256**, 90-96, (1987).

137 Wolf, S. P., Garner, A. & Dean, R. T. Free radicals, lipids, and protein degradation. *Trends Biochem Sci* **11**, 1-5, (1986).

138 Verzijl, N. *et al.* Age accumulation of Maillard products in human articular cartilage collagen. *Biochem. J.* **350**, 381-387, (2000).

139 Wells-Knecht, K. J., Zyzak, D. V., Litchfield, J. E., Thorpe, S. R. & Baynes, J. W. Mechanism of autoxidative glycosylation: identification of glyoxal and arabinose as intermediates in the autoxidative modification of proteins by glucose. *Biochemistry* **34**, 3702-3709, (1995).

140 Hazell, L. J., Berg, J. J. M. v. d. & Stocker, R. Oxidation of low-density lipoprotein by hypochlorite causes aggregation that is mediated by modification of lysine residues rather than lipidoxidation. *Biochem. J.* **302**, 297-304, (1994).

141 Cadet, J., Douki, T., Ravanat, J.-L. & Mascio, P. D. Sensitized formation of oxidatively generated damage to cellular DNA by UVA radiation. *Photochem. Photobiol. Sci.* **8**, 903-911, (2009).

142 Cadet, J., Douki, T. & Ravanat, J.-L. Measurement of oxidatively generated base damage in cellular DNA. *Mutation Research/Fundamental and Molecular Mechanisms of Mutagenesis* **711**, 3-12, (2011).

143 Pan, D. *et al.* Alloyed semiconductor nanocrystals with broad tunable band gaps. *Chemical Communications*, 4221-4223, (2009).

144 Stevens, J. *et al.* Structure of the Uncleaved Human H1 Hemagglutinin from the Extinct 1918 Influenza Virus. *Science* **303**, 1866-1870, (2004).

145 Russell, R. J. *et al.* The structure of H5N1 avian influenza neuraminidase suggests new opportunities for drug design. *Nature* **443**, 45-49, (2006).

146 Shen, X.-C. *et al.* Visible light-induced plasmid DNA damage catalyzed by a CdSe/ZnS-photosensitized nano-TiO_2 film. *Environ. Sci. Technol.* **42**, 5049-5054, (2008).

147 Garry, R. F. & Dash, S. Proteomics computational analyses suggest that hepatitis C virus E1 and pestivirus E2 envelope glycoproteins are truncated class II fusion proteins. *Virology* **307**, 255-265, (2003).

148 Markley, J. L. & Porubcan, M. A. The charge-relay system of serine proteinases: proton magnetic resonance titration studies of the four histidines of porcine trypsin. *J. Mol. Biol.* **102**, 487-509, (1976).

149 Webster, R. G., Bean, W. J., Gorman, O. T., Chambers, T. M. & Kawaoka, Y. Evolution and ecology of influenza A viruses. *Microbiol. Rev.* **56**, 152-179, (1992).

150 Helmolt, R. v., Wecker, J., Holzapfel, B., Schultz, L. & Samwer, K. Giant negative magnetoresistance in perovskitelike $La_{2/3}Ba_{1/3}MnO_x$ ferromagnetic films. *Phys. Rev. Lett.* **71**, 2331-2333, (1993).

151 Jin, S. *et al.* Thousandfold Change in Resistivity in Magnetoresistive La-Ca-Mn-O Films. *Science* **264**, 413-415, (1994).

152 Minh, N. Q. Ceramic Fuel Cells. *J. Am. Ceram. Soc.* **76**, 563-588, (1993).

153 Voorhoeve, R. J. H., Johnson, D. W. J., Remeika, J. P. & Gallagher, P. K. Perovskite Oxides: Materials Science in Catalysis. *Science* **195**, 827-833, (1977).

154 Kim, C. H., Qi, G., Dahlberg, K. & Li, W. Strontium-Doped Perovskites Rival Platinum Catalysts for Treating NOx in Simulated Diesel Exhaust. *Science* **327**, 1624-1627, (2010).

155 Kuo, J. H., Anderson, H. U. & Sparlin, D. M. Oxidation-reduction behavior of undoped and Sr-doped $LaMnO_3$ nonstoichiometry and defect structure. *J. Solid State Chem.* **83**, 52-60, (1989).

156 Seiyama, T. Total Oxidation of Hydrocarbons on Perovskite Oxides. *Catal. Rev.-Sci. Eng.* **34**, 281-300, (1992).

157 Arulraj, A. *et al.* Insulator-Metal Transitions, Giant Magnetoresistance, and Related Aspects of the Cation-Deficient $LaMnO_3$ Compositions $La_{1-\delta}MnO3$ and $LaMn_{1-\delta}O3$. *J. Solid State Chem.* **127**, 87-91, (1996).

158 Dezanneau, G., Sin, A., Roussel, H., Audier, M. & Vincent, H. Magnetic properties related to structure and complete composition analyses of nanocrystalline $La_{1-x}Mn_{1-y}O_3$ powders. *J. Solid State Chem.* **173**, 216-226, (2003).

159 Wang, H., Zhao, Z., Xu, C.-M. & Liu, J. Nanometric $La_{1-x}K_xMnO_3$ Perovskite-type Oxides-Highly Active Catalysts for the Combustion of Diesel Soot Particle under Loose Contact Conditions. *Catal. Lett.* **102**, 251-256, (2005).

160 Horyń, R. & Klimkiewicz, R. High Thermodynamic Stability of La-deficient Rhombohedral Form of Lanthanum Manganite Phase as Decisive Factor in Effective Ketonization Reaction of 1-Butanol. *Appl. Catal. A-Gen.* **351**, 184-188, (2008).

161 Rodríguez-Carvajal, J., Hennion, M., Moussa, F. & Moudden, A. H. Neutron-Diffraction Study of the Jahn-Teller Transition in Stoichiometric $LaMnO_3$. *Phys. Rev. B* **57**, R3189-R3192, (1998).

162 Zuo, Y., Li, J., Yi, J., Wang, Z. & Chen, C. Determination of A-site Deficiency in Lanthanum Manganite by XRD Intensity Ratio. *J. Solid State Chem.* **181**, 700-704, (2008).

163 Malavasi, L. *et al.* Effects of cation vacancy distribution in doped $LaMnO_{3+\delta}$ Perovskites. *J. Solid State Chem.* **178**, 2042-2049, (2005).

164 Ivanshin, V. A., Deisenhofer, J., Krug von Nidda, H.-A. & Loidl, A. ESR Study in Lightly Doped $La_{1-x}Sr_xMnO_3$. *Phys. Rev. B* **61**, 6213-6219, (2000).

165 Huber, D. L. *et al.* EPR linewidths in La1-xCaxMnO3: 0<~x<~1. *Phys. Rev. B* **60**, 12155-12161, (1999).

166 Machocki, A. *et al.* Manganese-lanthanum oxides modified with silver for the catalytic combustion of methane. *J. Catal.* **227**, 282-296, (2004).

167 Ponce, S., Peña, M. A. & Fierro, J. L. G. Surface properties and catalytic performance in methane combustion of Sr-substituted lanthanum manganites. *Appl. Catal. B-Environ.* **24**, 193-205, (2000).

168 Scollay, R. Gene Therapy: a Brief Overview of the Past, Present, and Future. *Ann.N Y Acad. Sci.* **953**, 26-30, (2001).

169 Kay, M. A., Glorioso, J. C. & Naldini, L. Viral vectors for gene therapy: the art of turning infectious agents into vehicles of therapeutics. *Nature Med.* **7**, 33-40, (2001).

170 Promega. <http://www.promega.com/resources/protocols/technical-bulletins/0/luciferase-assay-system-protocol/> (2011).